

Motion compensation in X-ray tomography

submitted by

Ander Biguri

for the degree of Doctor of Philosophy

of the

University of Bath

Department of Electrical and Electronic Engineering

September 2017

COPYRIGHT

Attention is drawn to the fact that copyright of this thesis rests with its author. This copy of the thesis has been supplied on the condition that anyone who consults it is understood to recognise that its copyright rests with its author and that no quotation from the thesis and no information derived from it may be published without the prior written consent of the author.

This thesis may be made available for consultation within the University Library and may be photocopied or lent to other libraries for the purposes of consultation.

Signature of Author

Ander Biguri

Contents

| | | |
|----------|---------------------------------------------------------------|-----------|
| 1 | Introduction | 3 |
| 2 | X-ray imaging in medicine | 4 |
| 3 | The image reconstruction problem | 5 |
| 3.1 | Geometry of CBCT | 5 |
| 3.2 | FDK | 5 |
| 3.3 | Iterative reconstruction algorithms | 5 |
| 3.3.1 | Algebraic Reconstruction Techniques | 7 |
| 3.3.2 | Conjugate Gradient Least Squares | 9 |
| 3.3.3 | Total variation minimization with POCS | 10 |
| 3.3.4 | Total variation regularization via Rudin-Osher-Fatemi model . | 19 |
| 3.4 | Discussion | 21 |
| 4 | GPU methods in tomography | 22 |
| 4.1 | Hardware used in this research | 24 |
| 4.2 | GPGPU architecture | 24 |
| 4.2.1 | Exploiting GPGPUs for CT | 27 |
| 4.3 | The projection operator | 28 |
| 4.3.1 | Ray-voxel intersection method | 29 |
| 4.3.2 | Grid-interpolated methods | 33 |
| 4.3.3 | Comments on optimization | 35 |
| 4.3.4 | Differences between operators | 37 |
| 4.4 | The backprojection operator | 42 |
| 4.4.1 | Voxel-driven backprojection | 42 |
| 4.4.2 | Backprojection weights | 44 |
| 4.4.3 | Comments on optimization | 48 |
| 4.5 | Benchmark | 48 |
| 4.6 | The TIGRE toolbox | 51 |

| | | |
|----------|--------------------------------------------------------------|------------|
| 4.6.1 | Geometry in TIGRE | 51 |
| 4.6.2 | Structure | 52 |
| 4.7 | Summary | 56 |
| 5 | Experiments and Applications | 60 |
| 5.1 | Algorithm Experiments | 61 |
| 5.1.1 | Convergence rates | 61 |
| 5.1.2 | Total variation minimization | 65 |
| 5.2 | Iterative Algorithms in Different CT Applications | 69 |
| 5.2.1 | Medical Head CBCT from The Christie Hospital | 69 |
| 5.2.2 | Cryo Soft X-Ray Tomography at Diamond Light Source | 69 |
| 6 | Motion compensation modelling | 79 |
| 6.1 | Alternative motion modelling approach | 80 |
| 6.1.1 | Warped projection operator in a GPU | 81 |
| 6.1.2 | Warped back projection operator in a GPU | 82 |
| 6.1.3 | Motion-compensated algorithm | 83 |
| 6.2 | Results | 83 |
| 6.2.1 | Arbitrary deformation of a digital phantom | 84 |
| 6.2.2 | Real patient data | 87 |
| 6.2.3 | Computation times | 92 |
| 6.3 | Discussion | 93 |
| 7 | Numerical Study of Motion Compensation | 95 |
| 7.1 | Materials and methods | 96 |
| 7.2 | Results | 99 |
| 7.2.1 | Iterative algorithms vs FDK in 4D CBCT | 99 |
| 7.2.2 | Motion Compensated vs 4D CBCT | 99 |
| 7.2.3 | Substandard Deformation Vector Fields | 102 |
| 7.3 | Discussion | 109 |
| 8 | Conclusions and Future work | 111 |

Chapter 1

Introduction

Chapter 2

X-ray imaging in medicine

Chapter 3

The image reconstruction problem

This chapter tries to explain the mathematics behind CT reconstruction, the FDK algorithm and iterative reconstruction algorithms. After the formal proposition of the mathematical problem of integrating over straight lines, the FDK algorithm is introduced. Then, the alternative proposal of the iterative algebraic methods is shown, followed by a wide variety of different algorithms that can be used to solve the algebraic problem. These include gradient descend techniques, Krylov subspace methods, statistical approaches and compressed sensing techniques. Finally, a discussion of the challenges that arise from the use iterative algorithms are described.

3.1 Geometry of CBCT

3.2 FDK

3.3 Iterative reconstruction algorithms

Nowadays the FDK algorithm is the most widely used algorithm, and only until very recently it has been the only algorithm available in any commercial medical or industrial CT device. Companies started using hybrid iterative algorithms for a limited subsection of their software in 2010 earliest[19], for standard CT, and for IGRT/CBCT one of the firsts has been Varian Medical Systems Inc, patented Apr. 2017[47] , published on web Sep. 2017[24]. While using FDK is advantageous in some cases, often the algorithm behaves poorly, specially when errors arise in the data, or the amount of data is limited. This is because FDK is based on an analytical approximation of straight path integrals

in continuous spaces. Reality is far from straight path integrals, as due to X-ray physics photons do not behave linearly. Photons from CT machines are polychromatic, and human tissue is behaves non-linearly in respect to X-ray energy. Additionally, Compton scattering is a common effect, where the photons get reflected in different angles dependent on their energy. Apart from photon physics related errors, electronic noise is always present in detector technology being the only feasible way of avoiding it longer exposition times, harmful to live tissue. Limited data can additionally harm the image reconstruction, as CT has generally less detector data than the amount of voxels are desired to reconstruct. All these effects make CT image reconstruction a challenging problem and have strong effect in the behaviour of FDK. As an alternative to FDK, iterative algebraic reconstruction algorithms try to minimize a functional by updating the image continuously and comparing it to the measured data. These algorithms have been shown to improve reconstruction quality when the data is noisy and/or limited. Additionally, as they are an algebraic tool, they allow careful tuning of the mathematics, enabling them to change their behaviour.

Iterative algorithms in CT generally reffer to those algorithms that, as the name says, iterate, but solve the linearized model

$$Ax = b + \tilde{e} \quad (3.1)$$

on where $x \in \mathbb{R}^{N_{voxels}}$ is a vector representing the lexicographically ordered voxels of the 3D image, $b \in \mathbb{R}^{N_{pixels}}$ a vector of the detector measured pixels. A is the linearized model matrix, a matrix that describes the behaviour of the CT system. Each row of the matrix A is describes the behaviour of the X-rays that affect each single pixel in the detector. However, this matrix is so big that in practice its explicit form is impossible to store, and the matrix product operations Ax (or projection) and A^Tb are implemented instead. The next chapter goes into a bit more detail on how to operate with matrix A and its limitations. Errors from measurement are inevitable in any application, and there are linearization errors, as no model is perfect. In equation 3.1, \tilde{e} represents all those errors.

As an exact solution for x can not be found, the problem in equation 3.1 is minimized as

$$\hat{x} = \arg \min_x \|Ax - b\|^2 + R(x), \quad (3.2)$$

on where $R(x)$ is an optional regularization function. This minimization function has been widely studied in mathematics and there are multiple algorithms that can solve it. However not all algorithms that solve the equation can be used in CT reconstruction, due to the nature of the A matrix, as it is very big (approximately $10^8 \times 10^8$ in

a standard medical image) and very sparse (approximately 0.0017% of sparsity in a standard medical image). This makes the matrix severely ill-conditioned and impossible to store in memory. Additionally, often the CT problem can be underdetermined, making the problem ill-posed and further constraining the possible algorithms that can be used. That said, a wide variety of algorithm have been proposed to solve the CT algebraic problem and new ones are still being published. This section discusses a few of the available and most common algorithms that have been studied in this work and implemented in TIGRE. There are numerous other algorithms in the literature, and none of them are necessarily worse than the ones presented here.

3.3.1 Algebraic Reconstruction Techniques

Arguably the most well known iterative algorithm is the method known as the algebraic reconstruction technique (ART)[27], known as the Kaczmarz method outside the CT imaging field. The ART algorithm, for matrix elements $a_{ij} \in R$ is defined as

$$x^{n+1} = x^n + \frac{b_i - \langle a_i, x^n \rangle}{\|a_i\|^2} a_i^T, \quad (3.3)$$

where a_i is the i -th row of matrix A and \langle , \rangle denotes the inner product. The ART method projects the image into the hyperplane described by the equation in row i . Generally the method includes a relaxation parameter λ_n that controls the update size, and that decreases with the iteration number. This generally avoids the cyclical convergence that the method describes when the solution is not unique (the intersection of the hyperplanes is not a single point). By relaxing the update step, the algorithm converges to a single point. Generally the algorithm is also run with some inequality constraints, the most common one being a positivity constrain for x , as negative values are not physically possible.

Studies on the convergence of the ART algorithm show[23] that randomly choosing the order of the rows in each iteration (n) increase the convergence rate, even more if the probabilities of picking rows are different than one (different methods propose different probabilities)[64][35].

However, the ART method has a major disadvantage: the image x^{n+1} needs to be updated i times each iteration. In current CT applications, and specifically in CBCT, the amount of rows in the matrix i.e. the total amount of independent pixel measurements in the detector is a massive number. Following the same definition of standard medical image size from the thesis, a 512×512 detector, with 360 projection means that the amount of rows is in the order of 10^8 . In order to update the image less, the Simultaneous Iterative Reconstruction Technique (SIRT)[28] can be used, a method

that is very similar to Cimmino's method, that updates the image using simultaneously (instead of sequentially) all data in the measurement b , thus each iteration is a single update. While SIRT generally solves the problem of the high amount of updates in ART, it suffers from a very slow convergence in comparison, and will generally plateau in a solution that is not as good as what ART provides. The SIRT algorithm can be described in matrix form as

$$x^{n+1} = x^n + \lambda_n V A^T W^{-1} (b - Ax) \quad (3.4)$$

where $V = 1/\text{diag}(\sum_j a_{ij})$ and $W = \text{diag}(\sum_i a_{ij})$.

However, middle ground has also been proposed. Kak and Andersen proposed[5] the Simultaneous Algebraic Reconstruction Technique (SART) on where the image is updated using simultaneously all data from each X-ray projection, but still updating the image multiple times per iteration. Finally, the update can also be done using block-based methods, or Oriented Subsets (OS) with a variety of methods generally described as OS-SART[9] methods.

Similarly as with ART, the order of the subsets in both OS-SART and SART have influence in the convergence, with a lower impact than in ART. In this work an three methods have been implemented, a completely ordered method, a randomized ordered method with full sampling (i.e. all projections are ensured to be used once and only once per iteration) and an angular distance based one. This last one orders the subsets by selecting the next one as the subset with largest angular distance from the ones already used. The heuristic rationale is that the projections at larger angular distance update the image by a bigger step than projections angularly near. In all further result in this thesis, the default ordering is random, unless otherwise explicitly stated.

Relaxation parameter λ

As previously mentioned, changing the relaxation parameter per iteration can be of advantage, by avoiding cyclical convergence and often by increasing the general convergence rate. One of the commonly used methods for the reduction of lambda is simply reducing it by a reduction factor each iteration as

$$\lambda_{n+1} = \lambda_n * r_\lambda \quad (3.5)$$

where r_λ is some value close to one, such as $r_\lambda = 0.99$ or $r_\lambda = 0.999$. However this method, while useful to avoid cyclical convergence in ART methods, is of less use in simultaneous methods, as it generally slows the convergence rate.

It is worth noticing that this family of algorithms is very closely related to the well

known gradient descend methods, as the gradient of equation 3.2 is proportional to $A^T(Ax - b)$, or in other words $V = I$ and $W = I$ in equation 3.4. The gradient descend methods have been widely studied in the past years[65][51], as the Neural Networks community tries to find faster converging methods to train the nets they research. Among other methods proposed, Nesterov proposed an accelerated version of the gradient descend[40], that obtains a rate of convergence of $1/n^2$. The proposed update updates the result image in each iteration by pushing it in the current update and previous update direction combined. Nesterovs Accelerated Gradient (NAG) defines

$$\lambda_{n+1} = \frac{1 + \sqrt{1 + 4\lambda_n^2}}{2} \quad (3.6)$$

$$\gamma_n = \frac{1 - \lambda_n}{\lambda_{n+1}} \quad (3.7)$$

$$y^{n+1} = x^n - \frac{1}{\beta} \nabla f(x^n) \quad (3.8)$$

$$x^{n+1} = (1 - \gamma_n)y^{n+1} + \gamma_n y^n \quad (3.9)$$

with $\lambda_0 = 1$ and β being the Lipschitz smoothness of the function f . The line in equation 3.8 can be replaced by the SART/OS-SART/SIRT update on equation 3.4 to obtain an accelerated convergence rate. Some experimental results on the convergence of the algorithms can be found in Chapter 5.

3.3.2 Conjugate Gradient Least Squares

The conjugate gradient for the least squares problems (CGLS) is, at its name says, an algorithm that solves the least squares problems for the normal equations (equation 3.10) using the conjugate gradient method. As a very short description of the method, CGLS is a 2-norm minimization method that iterates through Krylov subspaces. Doing this, each step minimizes the next biggest eigenvector of the residual of the 2-norm of the normal equation, thus updating the solution by the biggest linear step possible. This results in a superior convergence compared to other iterative methods[33], and Krylov subspace methods are the fastest iterative solvers for linear equations.

$$A^T Ax = A^T b \quad (3.10)$$

However, these methods have their drawbacks, as when only the approximated transpose of the matrix A is known and when rounding errors appear after several iterations, the update step may be wrongly computed. The solution to this is restarting the algorithm, by recomputing the initial steps using as a prior image the current

solution of CGLS.

The full description and implementation of the algorithm can be found in table 4.1. For further reading about this method, the paper by Shechuk is suggested[58]. Various different Krylov subspace methods are also available in the literature, such as LSQR[50], GMRES[14], Bi-CGStab[69], among others.

3.3.3 Total variation minimization with POCS

Sometimes solving a regularized problem may result in a better final image than just trying to solve the data constraint with the model. This is especially useful in more ill-conditioned problems, such as when the data is very noisy (thus the model does not fit the data with accuracy) or when few projections are available (the system is more under-determined). In these cases, regularization can add a user constraint in the image domain that pushes the algorithm towards a specific solution among all the multiple possibilities. While a variety of regularization techniques and norms exist, the most suitable for CT imaging is the total variation (TV) norm.

The total variation norm is defined as the sum of the 2-norms of the directional gradients of the variable,

$$\|x\|_{\text{TV}} = \sum_n \left\| \sum_{\alpha} \partial_{\alpha} x_n \right\|_2. \quad (3.11)$$

Applied to CT imaging, the total variation norm is the sum of the total change occurred in the image. An image with less total variation would be an image that would have less change, or more flat, same valued regions. Regularizing with the TV norm as a minimization term will yield an image that is piecewise smooth and it happens that most of the objects imaged in CT scanners are piecewise smooth in linear attenuation, even more in medical CT imaging.

However, solving the minimization problem in equation 3.2 is not trivial with the TV regularization. One of the first robust algorithm is the so called Adaptive Steepest Descend, Projection Onto Convex Subsets, or ASD-POCS algorithm[61]. This algorithm not only minimizes the data constraint with TV regularization but also adaptively controls the TV minimization update, in order to adapt its strength according to the data constraint update. Several adaptations and improvements of this algorithm have been proposed in the literature[CITES], all based in the same mathematical basis.

ASD-POCS

The previous algorithms discussed in this chapter were unconstrained minimization methods. While the TV minimization problem can be solved similarly (see section 3.3.4) formalizing the algorithm as a non-linear constrained minimization adds an advantage in the case where the system is under-determined. In an unconstrained problem such as in equation 3.2, the balance between the data constrain and the regularization constrain can be tuned via a hyperparameter, but in the case of an under-determined system, multiple solutions for the data fidelity term may exist. By reformulating it as it is shown in the rest of this section, the image with the same data fidelity 2-norm but the lowest TV norm can be chosen.

The minimization will yield an image \vec{x}^* that minimizes

$$\vec{x}^* = \arg \min_{\vec{x}} \|\vec{x}\|_{\text{TV}} \quad (3.12)$$

subject to

$$\|A \cdot \vec{x} - \vec{b}\| \leq \epsilon, \quad (3.13)$$

$$\vec{x} \geq 0. \quad (3.14)$$

As previously described in this chapter, the data fidelity on equation 3.13 while desired to be zero, it will never reach to zero, due to inconsistencies in the data, model, noise, etcetera. Thus, in this algorithm it is introduced as a inequality constrain, instead of as the minimization problem itself. This introduces the parameter ϵ in the algorithm, the maximum 2-norm allowed for the data inconsistency. The problem in hand is now non-linear, due to the constraints, but convex.

The conditions for a constrained minimization to find the optimal solution can be obtained by satisfying the Karush Kuhn-Tucker conditions (a generalization of the Lagrange multiplies for inequality constraints). First, the Lagrangian for the current problems needs to be defined, as

$$\mathbf{L} = \|\vec{x}\|_{\text{TV}} + \lambda_0 \cdot (\|A \cdot \vec{x} - \vec{b}\|^2 - \epsilon^2) - \vec{\lambda} \cdot \vec{x}, \quad (3.15)$$

where $\vec{\lambda}$ is a vector of the same size as the image, but λ_0 is a single value. Two inequality constraints are imposed to the Lagrange multipliers, namely non-negativity

$$\lambda_i \geq 0, \quad (3.16)$$

and complementarity

$$h_i(\vec{x})\lambda_i = 0, \quad (3.17)$$

where $i = 0, 1, \dots, N_{pixels}$, and h_i is an alternative form of the inequality constraints as

$$h_0(\vec{x}) = \|A \cdot \vec{x} - \vec{b}\|^2 - \epsilon^2 \leq 0 \quad (3.18)$$

$$h_i(\vec{x}) = -x_i \leq 0 \quad i \in [1, N_{pixels}] \quad (3.19)$$

Thus, only when the inequalities are violated does h_i turns non-zero, and with the complementarity condition, does the corresponding λ_i turns zero. A solution can be found for \vec{x} when the gradient of the Lagrangian is zero, and if the differential operator is defined as

$$\nabla_{\vec{x}} Q(\vec{x}) = \sum_i \partial_{x_i} Q(\vec{x}) \vec{\delta}_i \quad (3.20)$$

where $\vec{\delta}_i$ is the Kronecker delta. The gradient of the Lagrangian can be then written as

$$\begin{aligned} \nabla_{\vec{x}} \mathbf{L} &= \nabla_{\vec{x}} \|\vec{x}\|_{TV} + \lambda_0 \nabla_{\vec{x}} h_0(\vec{x}) + \sum_{i=1}^{N_{pixels}} \lambda_i \nabla_{\vec{x}} h_i(\vec{x}) = 0 \\ &= \nabla_{\vec{x}} \|\vec{x}\|_{TV} + 2\lambda_0 A^T \cdot (A \cdot \vec{x} - \vec{b}) - \vec{\lambda} = 0 \end{aligned} \quad (3.21)$$

Further simplification can be applied to equation 3.21. As the non-negativity constraints are only active in zero valued voxels, the Lagrange multipliers are zero for strictly positive voxels. Thus, by adding an indicator function

$$\vec{x}_{indic} = \begin{cases} 1 & \vec{x} \neq 0 \\ 0 & \vec{x} = 0 \end{cases} \quad (3.22)$$

the Lagrangian gradient can be shortened to

$$\nabla_{\vec{x}} \mathbf{L} = \text{diag}(\vec{x}_{indic}) (\nabla_{\vec{x}} \|\vec{x}\|_{TV} + \lambda_0 \nabla_{\vec{x}} h_0(\vec{x})) = 0. \quad (3.23)$$

Separating this new equation into two vectors,

$$\begin{aligned} \vec{d}_{TV} &= \text{diag}(\vec{x}_{indic}) (\nabla_{\vec{x}} \|\vec{x}\|_{TV}) \\ \vec{d}_{data} &= \text{diag}(\vec{x}_{indic}) (\nabla_{\vec{x}} h_0(\vec{x})) \end{aligned} \quad (3.24)$$

brings to the Karush Kuhn-Tucker conditions: \vec{x} will be an optimal condition if \vec{d}_{TV}

and \vec{d}_{data} are pointing in exactly the opposite direction. In practice the algorithm will only check if the vectors are pulling in opposite direction (by computing the dot product) and that the inequality constraints are satisfied. By checking the direction of the vectors the algorithm ensures that even if the data constrain is satisfied, only the optimal solution regarding both TV norm and data fidelity is chosen.

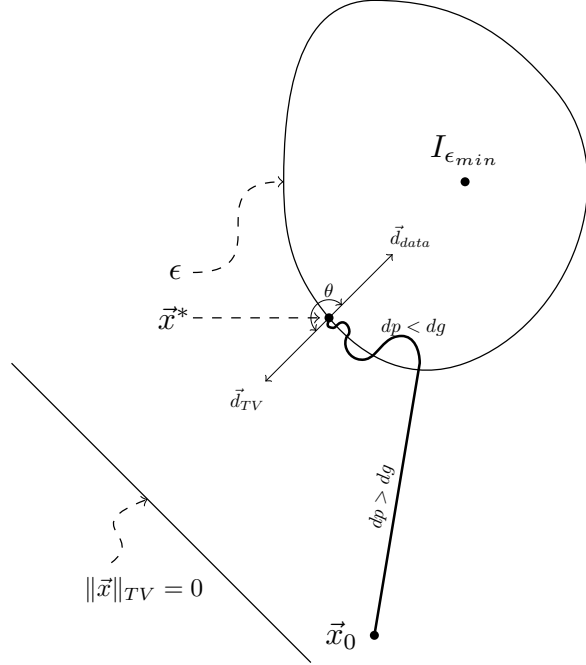


Figure 3-1: Conceptual diagram of the ASD-POCS algorithm path to the solution.

Figure 3-1 shows a conceptual diagram of the ASD-POCS algorithm. There is an area around the image with minimum data constrain, $I_{\epsilon_{min}}$. The solution \vec{x}^* generally lies on the boundary of the area with the user specified ϵ . From an initial image \vec{x}_0 , the algorithm walks towards the area of acceptable ϵ more strongly than towards the area of minimum TV, as the step sizes of the vectors \vec{d}_{TV} and \vec{d}_{data} , dp and dg respectively, are adaptively controlled to be $dp > dg$. Once the image is within acceptable 2 norm, then the step size is changed in order to have stronger \vec{d}_{TV} ($dp < dg$). The optimal solution can be found when both vectors point in opposing direction, or in other words, when the angle between them is 180 degrees, or the cosine of it is -1,

$$\cos \theta = \frac{\vec{d}_{\text{TV}} \cdot \vec{d}_{\text{data}}}{\|\vec{d}_{\text{TV}}\| \|\vec{d}_{\text{data}}\|}. \quad (3.25)$$

The pseudocode for the algorithm can be seen in algorithm 1. The algorithm is

essentially solving the two vector in equation 3.24, the data vector in lines [5-8] and the TV vector in lines [18-22]. Line [9] enforces the positivity constrain. In the algorithm, d_{tv} is initialized according to α , an user specified TV hyperparameter for TV, together with dp , the step size performed by the data constrain. After the TV minimization is performed, the step size of the TV vector is rechecked. If the TV minimization step is too big (bigger than the data step size), and the desired ϵ is still not achieved, the step size is reduced further. This method of adaptively setting the step size of the TV iteration relating to the data step size is what ensures the optimal condition is achieved. Finally, the stopping criteria relies in either achieving the desired ϵ with a desired $\cos \theta$, or stopping due to reaching a maximum amount of iterations (β decreases with iteration number). In the original proposition of the ASD-POCS algorithm (and shown here), the data constrain is solved using SART, however any other algorithm solving the same minimization problem can be used here (e.g. CGLS or OS-SART).

The algorithm has 7 parameters that need to be set up: β and β_{red} are the initial value and reduction ratio of the SART hyperparameter, similarly α and α_{red} serve as hyperparameter and reduction ratio for the TV minimization. r_{max} controls the maximum allowed ratio of change between the data minimization and the TV minimization, in order to adapt the step sizes. The number of iterations the TV minimization performs per iteration of the data minimization is defined as n_{TV} . Finally, the allowed data error is ϵ , as described before. The initial values of the variables in the algorithm are a key factor on its convergence. Empirical tests show that wrong parametrization of the algorithm can lead to severely noisy reconstructions. A study of the sensitivity of these parameters to changes has been performed by Lohvithee *et al*[36]. The study shows that some parameters can be safely set up to a static value regardless of the data, such as the data hyperparameters, but that ϵ , n_{TV} and α are critical parameters to tune in order to get an usable reconstruction, and they are heavily data dependant. While some algorithms have successfully replaced the initial set of α by some data based heuristics [CITE PCSD]¹ to the best of the authors knowledge there is no mathematical proposal for setting these parameters. The biggest drawback of this method is that several reconstructions may be needed to find the best parameters for an specific application.

Note that this minimization approach, while used for TV minimization in the original article, can be used for a variety of different minimization functions. For example, the TV minimization step could be replaced by a prior image minimization[CITE PICS], or any other convex minimization function. Similarly, the data minimization step can

¹These algorithms, namely PCSD and Aw-PCSD, are also available in TIGRE, by Manasavee Lohvithee.

be replaced by any other minimization algorithm, as long as it minimizes the problem in equation XX

Algorithm 1 ASD-POCS

```

1: Set:  $\beta, \beta_{red}, n_{TViter}, \alpha, \alpha_{red}, r_{max}$ 
2:  $\vec{x} = 0;$ 
3: while Stopping criteria not met do
4:    $\vec{x}_{prev} = \vec{x}$ 
5:   for  $n_{angles}$  do
6:      $\vec{x} = \vec{x} + \beta V A^T W^{-1} (\vec{b} - A \vec{x})$                                  $\triangleright$  SART update
7:   end for
8:    $\beta = \beta * \beta_{red}$ 
9:    $\vec{x} = \max(0, \vec{x})$                                                $\triangleright$  Enforce positivity
10:   $\vec{x}_{out} = \vec{x}$ 
11:   $\epsilon_{now} = \|A\vec{x} - \vec{b}\|$                                           $\triangleright$  Current  $\epsilon$ 
12:   $dp = \|\vec{x} - \vec{x}_{prev}\|$                                           $\triangleright$  Change in  $\vec{d}_{data}$ 
13:  if first iteration then
14:     $d_{tv} = \alpha * dp$                                           $\triangleright$  Initialize TV hyperparameter
15:  end if
16:   $\vec{x}_{prev} = \vec{x}$ 
17:
18:  for  $n_{TViter}$  do                                          $\triangleright$  TV update
19:     $\vec{dx} = \nabla_{\vec{x}} \|\vec{x}\|_{TV}$ 
20:     $\hat{\vec{dx}} = \vec{dx} / \|\vec{dx}\|$ 
21:     $\vec{x} = \vec{x} - d_{tv} \cdot \hat{\vec{dx}}$ 
22:  end for
23:   $dg = \|\vec{x} - \vec{x}_{prev}\|$                                           $\triangleright$  Change in  $\vec{d}_{TV}$ 
24:  if  $dg > r_{max} * dp$  and  $\epsilon_{now} > \epsilon$  then
25:     $d_{tv} = d_{tv} * \alpha_{red}$ 
26:  end if                                          $\triangleright$  Check stopping criteria
27:   $\cos \theta = \vec{dp} \cdot \vec{dg} / \|\vec{dp}\| \cdot \|\vec{dg}\|$ 
28:  if ( $\cos \theta < -0.9$  and  $\epsilon_{now} < \epsilon$ ) or  $\beta < 0.005$  then
29:    Stop
30:  end if
31: end while

```

B-ASD-POCS- β

Xue *et al*[77] proposed a faster converging modification of the ASD-POCS algorithm by adding a relaxed Bregman iteration to the overall algorithm. The Bregman iteration updates the projection data with part of the remaining error, thus reducing the residual faster and reaching convergence faster. The top level pseudo-code of the B-ASD-POCS-

β can be seen in algorithm 2.

Algorithm 2 B-ASD-POCS- β

```

1: Set:  $\beta, \beta_{red}, n_{TViter}, \alpha, \alpha_{red}, r_{max}$ 
2:  $\beta$  update ratio:  $c < 1$ 
3:  $\beta$  update period:  $T$ 
4:  $\vec{x} = 0;$ 
5: while Stopping criteria not met do
6:   for  $n_{Bregman}$  do
7:     ASD-POCS algorithm
8:   end for
9:    $\vec{b} = \vec{b} + \beta \cdot (\vec{b}^0 - A \cdot \vec{x})$ 
10:  Update  $\beta = c \cdot \beta$  if current iteration is update period  $T$  multiplier
11: end while

```

In the article, the authors show that this approach results in a faster (less amount of iterations) convergence, getting to a solution faster than in the standard ASD-POCS approach. This algorithm however requires 3 extra parameters for tuning.

The gradient of the TV norm

In order to minimize the TV norm via gradient descend, the gradient of the TV norm needs to be computed, $\nabla_{\vec{x}} \|\vec{x}\|_{TV}$, being \vec{x} the vectorized form of a N-dimensional image.

The main challenge wit the $\nabla_{\vec{x}} \|\vec{x}\|_{TV}$ term is that $\|\vec{x}\|_{TV}$ is not differentiable in the general case. However, in the CT case, \vec{x} can be described as x_{ijk} , a regularly discretized mesh of directional indices i, j, k of maximum value $i_{max}, j_{max}, k_{max}$. The gradient of x has an additional Cartesian index α :

$$g^\alpha = (\nabla x)^\alpha = \partial_\alpha x \quad (3.26)$$

$$g_{ijk}^\alpha = \partial_\alpha x_{ijk}. \quad (3.27)$$

The TV norm can me then defined as sum of the 2-norms of the gradient of x , g , over the Cartesian coordinate, resulting in a scalar.

$$\|x\|_{TV} = \sum_{ijk} \sqrt{\sum_\alpha (g_{ijk}^\alpha)^2} = \sum_{ijk} \sqrt{\sum_\alpha (\partial_\alpha x_{ijk})^2}, \quad (3.28)$$

This is the term that the total variation regularization algorithm minimizes with a

gradient descend. In order to perform this, the gradient of this term with respect to x is needed, now defined in a scalar field

$$(\nabla_x \|x\|_{TV})_{ijk}. \quad (3.29)$$

This derivative can be expanded to a 3 component value for each x_{ijk} as:

$$\begin{aligned} (\nabla_x \|x\|_{TV})_{ijk} &= \frac{\partial}{\partial x_{ijk}} \|x\|_{TV} = \partial_{x_{ijk}} \sum_{i'j'k'} \sqrt{\sum_{\alpha} (\partial_{\alpha} x_{i'j'k'})^2} \\ &= \sum_{i'j'k'} \partial_{x_{ijk}} \sqrt{\sum_{\alpha} (\partial_{\alpha} x_{i'j'k'})^2} \\ &= \sum_{i'j'k'} \frac{\sum_{\alpha} (\partial_{\alpha} x_{i'j'k'}) \partial_{x_{ijk}} (\partial_{\alpha} x_{i'j'k'})}{\sqrt{\sum_{\alpha} (\partial_{\alpha} x_{i'j'k'})^2}}. \end{aligned} \quad (3.30)$$

This term now contains ∂_{α} derivatives, i.e. derivatives in the Cartesian coordinate system $[x, y, z]$. These are defined as

$$\begin{aligned} \partial_x x_{i'j'k'} &= \lim_{h \rightarrow 0} \frac{x_{i'+h,j',k'} - x_{i',j',k'}}{h} \\ \partial_y x_{i'j'k'} &= \lim_{h \rightarrow 0} \frac{x_{i',j'+h,k'} - x_{i',j',k'}}{h} \\ \partial_z x_{i'j'k'} &= \lim_{h \rightarrow 0} \frac{x_{i',j',k'+h} - x_{i',j',k'}}{h}. \end{aligned} \quad (3.31)$$

However, x is discrete, thus the limit definition of the derivative can not be used to numerically compute it, but an approximation of it can. By setting $h = 1$, equation 3.31 becomes the backward finite differences of the first order approximation of a derivative, a very computationally cheap operation. The derivative w.r.t. the Cartesian coordinate can be rewritten as

$$\begin{aligned} \partial_{\alpha} x_{i'j'k'} &= \delta_{\alpha x} (x_{i',j',k'} - x_{i'-1,j',k'}) + \delta_{\alpha y} (x_{i',j',k'} - x_{i',j'-1,k'}) \\ &\quad + \delta_{\alpha z} (x_{i',j',k'} - x_{i',j',k'-1}) \end{aligned} \quad (3.32)$$

where δ_{α} is a Kronecker delta for the Cartesian axis. The other partial derivative term that appears in equation 3.30 is $\partial_{x_{ijk}} (\partial_{\alpha} x_{i'j'k'})$. As the derivative is w.r.t. x_{ijk} , each component of x is an independent variable, thus $\partial_{x_{ijk}} (\partial_{\alpha} x_{i'j'k'})$ is zero everywhere but

in indices $i = i' \wedge j = j' \wedge k = k'$, where the derivative is 1. The term then becomes

$$\begin{aligned}
\partial_{x_{ijk}} \partial_x x_{i'j'k'} &= \partial_{x_{ijk}} (x_{i',j',k'} - x_{i'-1,j',k'}) = \delta_{i',i} \delta_{j',j} \delta_{k',k} - \delta_{i'-1,i} \delta_{j',j} \delta_{k',k} \\
&= \delta_{i',i} \delta_{j',j} \delta_{k',k} - \delta_{i',i+1} \delta_{j',j} \delta_{k',k} \\
\partial_{x_{ijk}} \partial_y x_{i'j'k'} &= \partial_{x_{ijk}} (x_{i',j',k'} - x_{i',j'-1,k'}) = \delta_{i',i} \delta_{j',j} \delta_{k',k} - \delta_{i',i} \delta_{j'-1,j} \delta_{k',k} \\
&= \delta_{i',i} \delta_{j',j} \delta_{k',k} - \delta_{i',i} \delta_{j',j+1} \delta_{k',k} \\
\partial_{x_{ijk}} \partial_z x_{i'j'k'} &= \partial_{x_{ijk}} (x_{i',j',k'} - f_{i',j',k'-1}) = \delta_{i',i} \delta_{j',j} \delta_{k',k} - \delta_{i',i} \delta_{j',j} \delta_{k'-1,k} \\
&= \delta_{i',i} \delta_{j',j} \delta_{k',k} - \delta_{i',i} \delta_{j',j} \delta_{k',k+1}.
\end{aligned} \tag{3.33}$$

These terms are practically a selecting function for i', j', k' , matching only in the indices $i, i+1, j, j+1, k, k+1$ in the sum of the right hand side of equation 3.30. However the indices are limited to $i' \in [1, i_{max}]$, $j' \in [1, j_{max}]$ and $k' \in [1, k_{max}]$. As boundary conditions, Neumann boundary conditions are set to zero. To enforce that, a Kronecker deltas can be introduced for each index, $(1 - \delta_{i,i_{max}})$, with the same approach with the other indices.

Finally, substituting in equation 3.30, the gradient of the TV norm can be described as

$$\begin{aligned}
(\nabla_x \|x\|_{\text{TV}})_{ijk} &= \sum_{i'j'k'} \frac{\sum_{\alpha} (\partial_{\alpha} x_{i'j'k'}) \partial_{x_{ijk}} (\partial_{\alpha} x_{i'j'k'})}{\sqrt{\sum_{\alpha} (\partial_{\alpha} x_{i'j'k'})^2}} \\
&= \sum_{i'j'k'} \frac{\partial_x x_{i'j'k'} \partial_{x_{ijk}} (\partial_x x_{i'j'k'}) + \partial_y x_{i'j'k'} \partial_{x_{ijk}} (\partial_y x_{i'j'k'}) + \partial_z x_{i'j'k'} \partial_{x_{ijk}} (\partial_z x_{i'j'k'})}{\sqrt{\sum_{\alpha} (\partial_{\alpha} x_{i'j'k'})^2}} \\
&= \frac{\partial_x x_{i,j,k} + \partial_y x_{i,j,k} + \partial_z x_{i,j,k}}{\sqrt{\sum_{\alpha} (\partial_{\alpha} x_{i,j,k})^2}} \\
&\quad - \frac{(1 - \delta_{i,i_{max}}) \partial_z x_{i+1,j,k}}{\sqrt{\sum_{\alpha} (\partial_{\alpha} x_{i+1,j,k})^2}} - \frac{(1 - \delta_{j,j_{max}}) \partial_y x_{i,j+1,k}}{\sqrt{\sum_{\alpha} (\partial_{\alpha} x_{i,j+1,k})^2}} - \frac{(1 - \delta_{k,k_{max}}) \partial_z x_{i,j,k+1}}{\sqrt{\sum_{\alpha} (\partial_{\alpha} x_{i,j,k+1})^2}}.
\end{aligned} \tag{3.34}$$

Equation 3.34 is the numerical approximation of the gradient of the total variation norm, and describes scalar field of the same size of the image. The same approach can be used with central and forward differences to obtain a similar equation, however central differences may not correctly minimize the TV norm of the image. As central differences do not take into account the value of the current voxel ijk , a chequerboard pattern would have zero TV norm, and this is the opposite of the purpose of the algorithm,

therefore only numerical approximations of derivatives that take immediately adjacent pixel values into account can be used (such as forward or backward finite differences).

3.3.4 Total variation regularization via Rudin-Osher-Fatemi model

A different minimization approach to POCS is the approach proposed by Jia *et al*[26], that uses the Rudin-Osher-Fatemi (ROF) model for total variation minimization, widely used in the denoising literature[52][17][71]. By starting from the same minimization problem, namely

$$\hat{x} = \arg \min_x \|Ax - b\|^2 + \lambda \|x\|_{TV}, \quad (3.35)$$

a forward-backward splitting algorithm[15] is used to split the minimization into two alternating steps, the TV and the data steps. If the optimality condition is considered to be

$$\frac{\partial}{\partial x_\alpha} \|Ax - b\|^2 + \lambda \frac{\partial}{\partial x_\alpha} \|x\|_{TV} = 0, \quad (3.36)$$

being α the set of Cartesian coordinates, then the problem can be split into the following equations, where g is a auxiliary function and $\mu > 0$:

$$\lambda \frac{\partial}{\partial x_\alpha} \|x\|_{TV} = \mu(x - g) \quad (3.37)$$

$$\frac{\partial}{\partial x_\alpha} \|Ax - b\|^2 = -\mu(x - g). \quad (3.38)$$

By solving for g , the simplified version of the algorithm can be seen in 3.

Algorithm 3 TV minimization with ROF model

- 1: Solve: $g = x - \frac{\lambda}{\mu} \frac{\partial}{\partial x_\alpha} \|Ax - b\|^2$ ▷ SART
 - 2: Minimize: $x = \arg \min_x \|x\|_{TV} + 0.5 * \mu \|x - g\|^2$
 - 3: Enforce positivity: $x = \max(0, x)$
-

The first line of the algorithm its essentially a gradient descend iteration, which can be replaced with a SART iteration. Note that the this iteration can be replaced by other data-minimization algorithms such as CGLS. The second line is the ROF model, widely researched in image denoising. The ROF model tries to find the image x with minimum total variation subject to having the minimal deviation from its original value g . By changing the value of he hyperparameter μ , the strength of this regularization is controlled. A high μ will ensure that the image is very similar to its original value, while a small μ will be more lax. The advantage of this approach compared to the ASD-POCS algorithm is that it requires no extra projection or backprojection operations.

Additionally, minimizing the ROF model is a very well studied problem in the image processing field, and it has lead to finding computationally efficient methods.

In the article by Jia *et al*, they solve the ROF model via gradient descend and controlling its step size with Armijo's rule. In this work a different approach is taken, based on the image processing literature.

Primal Dual formulation of the ROF model

As previously shown in line 2 of algorithm 3, the ROF model can be formulated as

$$\hat{x}_{ROF} = \arg \min_x \|x\|_{TV} + \frac{\mu}{2} \|x - g\|^2. \quad (3.39)$$

A solution of this problem using a primal-dual (PDU) approach has been proposed in literature[79], by changing the minimization equation to a saddle point optimization problem. While a wide variety of methods have been proposed to minimize the ROF model[52][71][10], the PDU method has the advantage of being very parallelizable, thus a perfect fit for GPU computing. The dual variable can be proposed by using the TV definition of $\|x\|_{TV} = \|\nabla x\|$ and observing the following consequence of the Cauchy-Schwartz inequality

$$\|\nabla x\| = \arg \max_{\|\mathbf{p}\| \leq 1} \|\mathbf{p} \nabla x\|, \quad (3.40)$$

where $\mathbf{p} = (p^1, p^2, p^3)^T$ (for the 3D case) is the said dual variable. Note that each p^i is the size of the image x . Equation 3.39 can be then rewritten as

$$\hat{x}_{ROF} = \arg \min_x \arg \max_{\|\mathbf{p}\| \leq 1} \|\mathbf{p} \nabla x\| + \frac{\mu}{2} \|x - g\|^2. \quad (3.41)$$

The primal and dual updates can be both obtained from this equation. For the primal update, differentiating the equation according to x results in

$$-\nabla \cdot \mathbf{p} + \mu(x - g) = 0, \quad (3.42)$$

and one can solve it for x by performing a gradient descend update as

$$x^{n+1} = x^n(1 + \tau_P^n) + \tau_P^n \left(g + \frac{1}{\mu} \nabla \cdot \mathbf{p} \right), \quad (3.43)$$

where τ_P is the primal step size. The dual update can be computed similarly, by

differentiating equation 3.41 according to \mathbf{p} , the following equation is obtained:

$$\nabla x + \mathbf{p}\alpha = 0, \quad (3.44)$$

where α is a Lagrange multiplier for the inequality constrain $\|\mathbf{p}\| \leq 1$. This equation can be maximized with a gradient ascend method as

$$\mathbf{p}^{n+1} = \Pi_{B_0}(\mathbf{p}^n + \tau_D^n \nabla x), \quad (3.45)$$

where $\Pi_{B_0}(\mathbf{p}) = \frac{\mathbf{p}}{\max\{1, \|\mathbf{p}\|\}}$ is a projection onto the unit ball centred in the origin.

The PDU algorithm consists in updating \mathbf{p} and x iteratively, by alternating the updates. In [79][31] a step size update is proposed for the primal and dual step sizes:

$$\begin{aligned} \tau_D^n &= 0.3 + 0.02n \\ \tau_P^n &= \frac{1}{\tau_D^n} \left(\frac{1}{6} - \frac{5}{15+n} \right). \end{aligned} \quad (3.46)$$

The same update is used in this work, as the images in their work are structurally similar to CT images and empirical test showed satisfactory results. The algorithm can be shown to converge as it is shown in [80] that the primal-dual gap decreases with each update of x^n , and the gap is suggested as a control variable for the stopping criteria. In this work the algorithm has been implemented without the stopping criteria check, and an user specified parameter for the number of iterations is passed as an input, with a default value of 50, as it empirically showed good results.

The discretization of the divergence and gradient operators are a key factor when numerically computing the PDU algorithm, as they need to be consequent with each other. Thus, the gradient can be approximated using forward differences, but as the divergence is the adjoint of the gradient, it must be approximated with backwards differences.

3.4 Discussion

Chapter 4

GPU methods in tomography

Tomographic reconstruction in 3D is not only challenging due to the mathematics of the reconstruction, but also comes with a significant computational burden. As an example, the detector may have 512^2 pixel per projection and the size of the reconstructed image is generally of the order of 512^3 voxels in medical applications. However, in micro-tomography the detectors can get to sizes such as 2000^2 pixels per angle with images of 2000^3 voxels. Such sizes are considerably big for standard computers and applying reconstruction techniques. Both “one pass” as FDK or iterative methods are massively computationally expensive, needing up to weeks to reconstruct the image if run on CPUs. This is in most cases an unreasonable waiting time, as images are required for immediate diagnosis or treatment adjustment when taken, so a faster solution is needed.

In iterative reconstruction techniques, the computational problem relies on the matrix A , generally used twice per iteration in most algorithms, by doing a projection ($A \cdot x$) and a backprojection ($A^T \cdot b$). The construction of this matrix is not possible in 3D tomography, due to its size. If we consider the medical case sizes presented before, with projections over 360 different angles, building explicitly the A matrix would require thousands of gigabytes of RAM memory just to store the 0.0017% of the matrix that has non-zero values. In order to avoid that, the common technique is to compute $A \cdot x$ and $A^T \cdot b$ as a single operation instead of computing A explicitly. This is possible because the matrix-vector operation $A \cdot x$ describes the result of the integral of the x-rays over the image and $A^T \cdot b$ describes a “smear” of the projection data onto the image in the corresponding voxels. Interestingly, both of this operands necessitate a massive amount of very independent and simple calculations.

Over the past years computational technology has evolved significantly. But Moore’s law, which expresses the halving of transistor size every two years, is coming to an end

due to physical laws. Transistors are currently on the 14nm scale and, while they are expected to reach 5nm by 2020, this clearly already breaks Moore’s law. As transistors reach this scale, quantum mechanics starts to have an important effect, especially quantum tunnelling where the electrons could just “jump”¹ to the other side of the transistor regardless of its state. Unless a breakthrough in the understanding and manufacturing of new materials that can overcome such effects is discovered, 5nm transistors is approximately the hard limit to how far processors can evolve. To overcome this limitation, research in different computer architectures has been a hot topic in the past decades. This lead to two separate, but similar advances: High Performance Computers (HPCs) and Graphic Processing Units (GPUs). HPCs developed in order to be able to accommodate the growing computational demands of researchers and industry, where big data and heavy parallel computations became more common. These are massive installations with an enormous power consumption and running costs. GPUs instead, advanced their technology in order to accommodate the more demanding graphic (or visual) specifications of mainly the video-game industry in personal computers. GPUs are intrinsically designed to run in personal devices, such as laptops or mobile phones, so they are designed to be not only fast but small, low consumption and cheap overall.

The computations on high-end graphics in video-games require similar algorithms and processes than some of the big computational problems in both industry and research. It turns out that the development of high throughput GPUs for video-games has brought a tool that can significantly help research methods nowadays, to the point that a new term has been coined: GPGPUs or General Purpose GPUs. GPGPUs are widely used in research, for example in molecular dynamic simulations[49], astrophysical hydrodynamics[56], artificial intelligence[4], and many more. The massively parallel architecture and large number of independent processors make GPGPUs the perfect tool to deal with computed tomography applications.

This chapter describes the core computational code used in this work. First, a further description of the GPU architecture is given. Then, the special features of these processors that make tomography, and especially iterative reconstruction algorithms, a good fit for GPGPUs is shown. Next, a detailed description is given of how the projection operator has been implemented and optimized for two different projection approaches. And finally, a similar description for both of the backprojection modes implemented is given.

This chapter focuses on CBCT geometry, but parallel geometries are also implemented in the code. Everything (both computational and algorithmic) discussed for CBCT is essentially the same for any other geometry, with some minor tweaks

¹Explanations about quantum mechanics are far beyond the goals of this thesis.

applied. All the methods discussed in this section and in the TIGRE toolbox are available open source and free to use/access in the paper[6] and GitHub repository github.com/CERN/TIGRE.

4.1 Hardware used in this research

Prior to the description of hardware architectures and programming tricks, it is important to describe the hardware that this research was developed on. While the work presented here applies to almost all different hardware types, it may not be 100% applicable to any GPU. GPUs are constantly changing so some features and computational tricks used for the acceleration of CT code are recent additions to GPGPUs and similarly new improvements to GPGPUs will come in the future that may render obsolete the information presented in this chapter. Therefore, this work presents techniques and benchmarks based on the hardware that was available and, while most of the techniques are applicable to most of GPUs, the mileage may vary. Additionally, most of the terminologies used in this chapter are related with NVIDIA/CUDA.

The research on this (and further) chapters of this thesis has been performed on a PC with a Windows 7 x64 operating system, with 32Gb of on board RAM, and a SSD hard drive. The GPU used was a NVIDIA Tesla 40k, that has 2880 stream processors, a clock frequency of 745-875 MHz and an on board RAM of 12GB. The processing power is generally described in terms of floating-point operations per second or FLOPS, and this particular GPU has a theoretical throughput of 4.29-5.04 TFLOPS on single-precision numbers.

4.2 GPGPU architecture

In order to better describe how GPU acceleration boosts tomographic reconstruction, a description of the hardware architecture of GPUs is required. As previously mentioned, GPUs are a technology that evolved from the increasing requirements of the entertainment industry in general but particularly from video games. In order to be able to have more realistic real-time graphics, where the environment reacts to the user interface by changing light reflections, textures, and simulating the physics of objects, a high throughput hardware is required. All these effects need a large amount of simple arithmetic to be computed and a fast access memory, faster than any modern CPU can handle. For that reason computers started having GPUs, special dedicated hardware that included hundreds of small, low-power, low-speed processors. These processors are significantly worse than any CPU, but the high number of them

allows very high throughput for any arithmetically heavy algorithm. However, this high computation-intensive output design also means that GPUs perform weakly on programs that need control flow and caching. This information is key for the correct design of GPU algorithms as will become more evident further in this chapter.

The general diagram of the GPU architecture is presented in figure 4-1. It has 3 main parts, the computational core, the device memory (DRAM) and the communication with the CPU via PCI express (PCIe). The principal part of the GPU is the computational part. This consists of several stream multiprocessors (SMs), 15 in the Tesla k40, that are responsible for the distribution of the instructions to the stream processors (SPs) or CUDA cores. Each of the SPs (2880 in total) can run a single *block* of instructions at any time, each of them consisting of up to 1024 parallel² *threads*. These blocks must be running the same algorithm, or *kernel*. Theoretically, each of the SPs can have 64 *concurrent warps*, or execution instructions running at the exact same clock cycle, each of these warps having 32 threads. This means that the Tesla k40 can have a theoretical maximum of 30720 arithmetic operations simultaneously executing. This is never reached as some of this time may be spent in flow control or memory reads, thus slowing the execution.

The second part of the GPU are the memory types. There are 3 types of memory in the GPU: registers, shared memory and device random access memory (DRAM). The main difference between them is in accessibility (what subset of the SPs can access it) and speed. The lowest level memory is register memory. This is a thread level memory, used to store all local variables during execution. It is fast access and low in size. No other thread or block can access this memory. The second memory type is shared memory. This memory is used when blocks need to share information, such as the result of a computation in the middle of the kernel. Each SM has its own shared memory and it is local to them. All blocks can access to it, but careful usage of it is needed as the parallel nature of the computation could mean multiple writing on the same memory by different blocks. This memory is bigger (up to 48KB) and it is fast access, but slower than registers. Finally, there is DRAM memory. DRAM memory is a global large (12GB) memory on the board. This memory is widely used as it is the place where memory before kernel calls is allocated and where the results are stored after kernel calls. However, GPU code will often need to work with big data, thus the DRAM read/write is also commonly used within kernels. DRAM accessing can lead to significant bottlenecks as a single memory access needs 200 to 300 clock cycles to be carried.

²In GPU computing, one should not confuse *parallel* with *concurrent*. Parallel means that the same instruction is divided into pieces, but they are not necessarily executed at the same time.

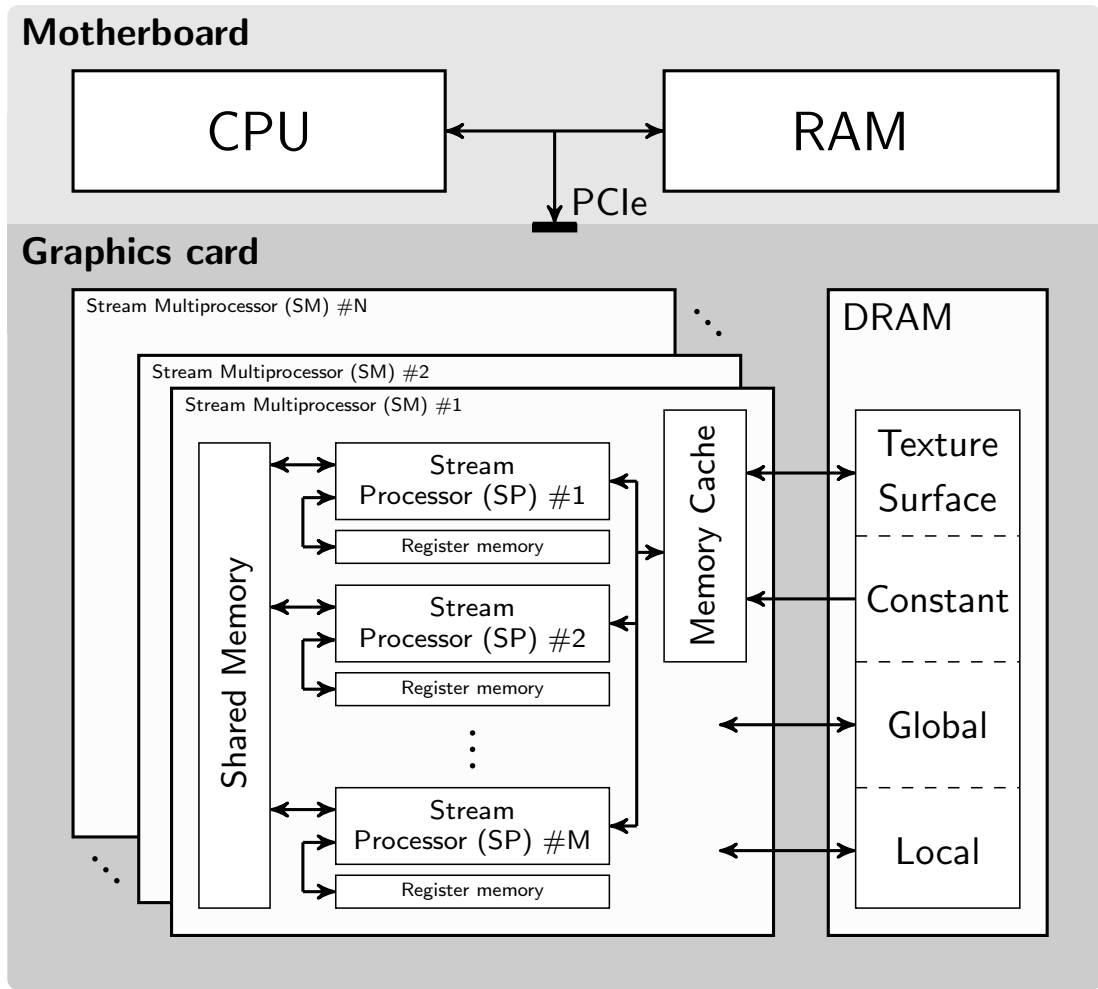


Figure 4-1: Diagram of the basic architecture of a GPU. It shows how processing units and memory is structured inside a graphics card.

To improve memory throughput, the GPU contains so-called L1/L2 cache memory on each of the SMs. This cache is designed to improve execution of *memory coalescing* warps. The cache, having a faster communication bus with the threads (needing about 80 cycles for a single memory read) stores a large amount of memory each time a single read to the DRAM is performed. The memory is loaded with locality, i.e., a memory chunk around the first sampled value is loaded, as the cache expects subsequent memory reads to be adjacent. Thus, when designing kernels, the order of the memory access can have a big influence on the final speed of the program.

Two memory types can be used when data locality needs to be exploited in cache access: texture and surface memory. The difference between them is that the former is read only while the later can also be written. These memories can be defined as 3D shaped, thus data locality can be exploited in all spatial dimensions. Additionally, both can be accessed with floating point index values, and the memory value is returned with user-chosen interpolated methods. If cached memory is desired, but not in a spatially correlated form, then the read only constant memory can be used. This memory is still cached and can be used to speed up values that may be needed often. Then there is the global memory, which is read and write but not cached. Finally, local memory is an extension of shared memory when it gets filled.

The third important section is the communication between CPU-GPU. This is done via PCI-express ports and it is a slow communication process. Passing data from CPU to GPUs is relatively fast (500Mb/s), but can be a bottleneck in memory-heavy applications such as CT imaging.

4.2.1 Exploiting GPGPUs for CT

In CT, two main operations need to be accelerated: projection and backprojection. While iterative algorithms are defined as algebraic methods using a big system matrix A , the matrix itself is rarely used alone in the equations, it is generally used as $A * x$ or $A^T * b$. Fortunately, these two operations have a physical meaning, as the projection is the integral of the image over the straight X-ray paths, and the backprojection is the “smearing” of the detector data over the image back in the direction of the source, also following straight paths. While computing the values of the rows and columns of the system matrix seems hardly possible in real time, these two operations can be performed abstracting from their algebraic equivalent. The projection operation is an integration over independent, yet closely related, straight paths. By being able to sample the image domain in parallel, the operation can be performed at high speed. Similarly, the backprojection relies on building straight lines from the source to the voxels or detectors (dependent on the backprojection type), and sampling the projections. These

operations are completely independent, hence the idea for GPU parallelism as threads will reach their maximum performance when they do not need to communicate with each other. Additionally, both operations need accurate sampling over large volumes, thus texture memory with interpolation is ideal as it is hardware optimized, giving faster interpolated values than in a CPU or any possible interpolation kernel. Thus the massive parallelism and texture memory are they key features of GPU computing that make it the ideal tool for accelerating tomography. The following sections provide more details.

4.3 The projection operator

The projection operator is the numerical equivalent of the X-ray integral that defines the model of X-ray tomography (see equation XX). This operator models the idealized physics, where all the X-rays have an infinitely small width and travel in a straight path to the center of each detector pixel, and all with the same energy. While this may not represent the physics accurately enough to be a reliable X-ray simulation tool, it is exactly what iterative methods need, the $A * x$ operation.

There are several method to simulate forward projection, all of them easily parallelizable. One of these is the distance-driven projection [38][54], where the ray-voxel and detector intersections are all projected in a mid-plane and values are accumulated there. Alternatively, the voxel-driven projector[16], where the whole voxel (square or other shape[32]) is projected onto the detector and its values spread among all the corresponding pixels. With a similar approach, the separable footprints technique[37][74] approximates the footprint of the voxel in the detector for speed-up. According to the authors it is more accurate than the distance-driven projection and faster than both the voxel-driven and distance-driven ones. Finally, in ray-driven projection[60][75][11] methods the line path is integrated. Among these, the most important variations worth mentioning are the infinitesimally small exact path, area path, and the grid-interpolated path. The exact path computes either the length of an infinitesimally narrow path or the area of a finite width path over each voxel and uses that as a weight for the integral. The grid-interpolated projector instead sets a fixed sample length and interpolates voxel values. According to a study by Fang and Mueller[76], the most accurate methods are the ray-driven ones.

This work has focused on the infinitesimally small ray-voxel intersection and grid-interpolated methods only because in both the desired accuracy and speed have been reached. The grid-interpolated method also is a key method for the following chapters (see Chapter 6 for more information). As the projection is basically an integral of

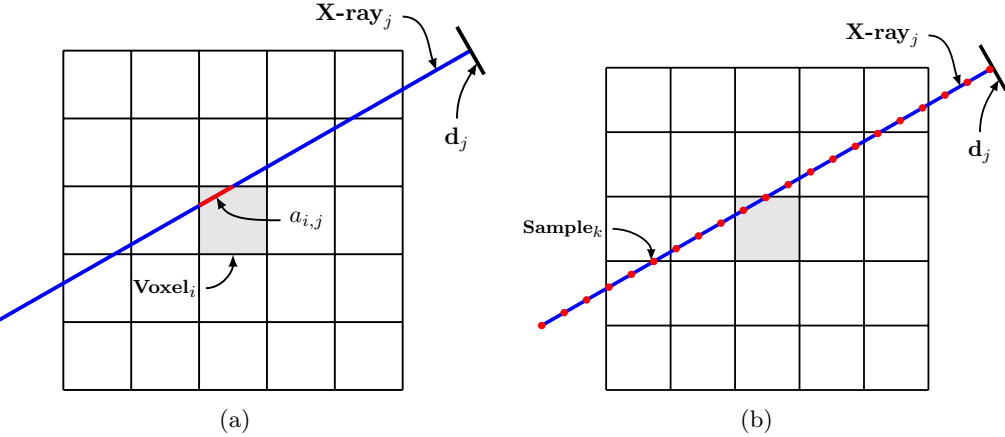


Figure 4-2: (a) Diagram of the projection operation using the line-voxel intersection methods and (b) diagram of the interpolated sampling method.

a volume over thousands of independent paths, it is straightforward to parallelize by independently computing each ray. The ray-voxel intersection method is equivalent to the algebraic representation, where the A matrix contains the length of the intersection between voxels and the path. Those are multiplied and added to the voxel values themselves to obtain the detector values. However, while not feasible in CPUs, the grid-interpolated method can use the practically free (i.e., very little time overhead) texture memory interpolation for speed-up in GPUs. The difference between the methods can be seen in figure 4-2.

4.3.1 Ray-voxel intersection method

As previously mentioned, this method relies on accumulating the length of the intersection between a straight path and voxels multiplied by the voxel value. The X-ray integral from equation XX can be discretized as in equation 4.1, where d_{uv} is the detector value of X-ray uv , $\mathbb{I}(ijk)$ are the voxel values of the image and $l_{uv,ijk}$ the length of the path within each voxel. Note that here $l_{uv,ijk}$ are the same values as the elements of matrix A . Computing $l_{(uv,ijk)}$ requires some geometrical computations, not only the reliable detection of the intersections between the lines and voxel boundaries, but also avoiding computing it on voxels where the line does not intersect.

$$d_{(uv)} = \sum_{ijk=0}^{N_{\mathbb{I}}} l_{(uv,ijk)} * \mathbb{I}(ijk) \quad (4.1)$$

The algorithm to compute d_{uvj} has been taken from Jacobs[20] improvement on

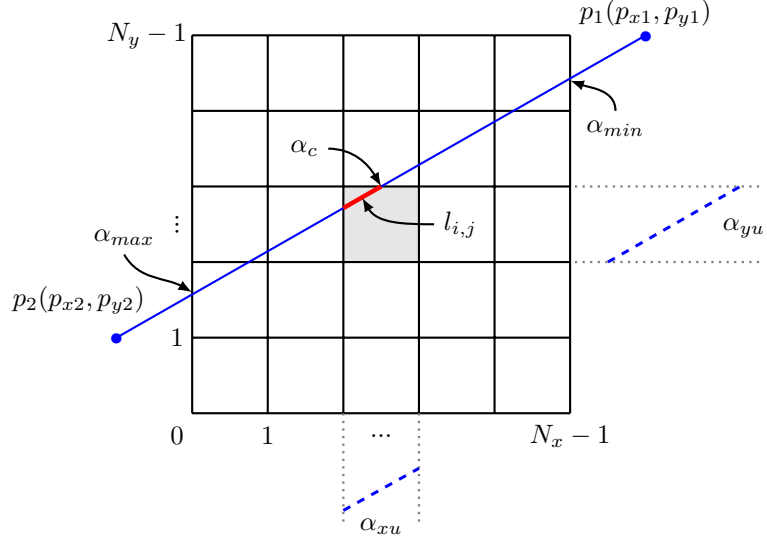


Figure 4-3: Diagram of the relevant variables for Jacobs' ray-tracing algorithm.

Siddon's method[60]. For the sake of clarity, the algorithm is described for the 2D case, but the extension to 3D is trivial. The algorithm is based on computing the intersection between the path and the x and y planes and iterating over the ray until the next intersection is found. The diagram of the variables used in the algorithm can be seen in figure 4-3. The following derivation assumes that the pixels are of size 1 and the image domain starts at $(0, 0)$, as this assumption reduces the number of operations needed. Assuming non-trivial rays from point (p_{x1}, p_{y1}) to point (p_{x2}, p_{y2}) , the parametric representation of the ray is

$$p_{12} = \begin{cases} p_x(\alpha) &= p_{x1} + \alpha(p_{x2} - p_{x1}) \\ p_y(\alpha) &= p_{y1} + \alpha(p_{y2} - p_{y1}), \end{cases} \quad (4.2)$$

where $\alpha \in [0, 1]$. In order to know the number of intersections, the initial and final intersections of the ray in the image are needed. The intersection points in terms of alpha can be defined as

$$\alpha_x(i) = \frac{(i - p_{x1})}{p_{x2} - p_{x1}} \quad (4.3)$$

$$\alpha_y(j) = \frac{(j - p_{y1})}{p_{y2} - p_{y1}}, \quad (4.4)$$

where i and j are indices of the pixels. If the number of planes is defined as N_x and N_y , one can compute the minimum and maximum α values (i.e., values of the line at

the boundary of the image) by comparing the values of α in each direction as

$$\alpha_{min} = \max \left(\min (\alpha_x(0), \alpha_x(N_x - 1)), \min (\alpha_y(0), \alpha_y(N_y - 1)) \right) \quad (4.5)$$

$$\alpha_{max} = \min \left(\max (\alpha_x(0), \alpha_x(N_x - 1)), \max (\alpha_y(0), \alpha_y(N_y - 1)) \right). \quad (4.6)$$

Note that this is equivalent to writing

$$\alpha_{min} = \max (\alpha_{xmin}, \alpha_{ymin}) \quad (4.7)$$

$$\alpha_{max} = \min (\alpha_{xmax}, \alpha_{ymax}). \quad (4.8)$$

Next, the planes where the rays first cross in each direction need to be computed. This can be achieved by looking at the different α values. For the x dimension, equations 4.9-4.12 show how to compute the plane index i_{min} and i_{max} if $p_{x1} < p_{x2}$ and equations 4.13-4.16 when $p_{x1} > p_{x2}$. The same logic applies to j_{min} and j_{max} .

$$\alpha_{min} = \alpha_{xmin} \rightarrow i_{min} = 1 \quad (4.9)$$

$$\alpha_{min} \neq \alpha_{xmin} \rightarrow i_{min} = \lceil p_x(\alpha_{xmin}) \rceil \quad (4.10)$$

$$\alpha_{max} = \alpha_{xmax} \rightarrow i_{max} = N_x - 1 \quad (4.11)$$

$$\alpha_{max} \neq \alpha_{xmax} \rightarrow i_{max} = \lfloor p_x(\alpha_{xmax}) \rfloor \quad (4.12)$$

$$\alpha_{min} = \alpha_{xmin} \rightarrow i_{max} = N_x - 2 \quad (4.13)$$

$$\alpha_{min} \neq \alpha_{xmin} \rightarrow i_{max} = \lfloor p_x(\alpha_{xmin}) \rfloor \quad (4.14)$$

$$\alpha_{max} = \alpha_{xmax} \rightarrow i_{min} = 0 \quad (4.15)$$

$$\alpha_{max} \neq \alpha_{xmax} \rightarrow i_{max} = \lceil p_x(\alpha_{xmax}) \rceil. \quad (4.16)$$

At this point, the α_x and α_y values of the first intersection point can be obtained by substituting either (i_{min}, j_{min}) or (i_{max}, j_{max}) (depending on the relationship of p_1 and p_2) into equations 4.3 and 4.4. Additionally, one can compute the number of planes that the ray crosses (N_p) with the following equation:

$$N_p = (i_{max} - i_{min} + 1) + (j_{max} - j_{min} + 1). \quad (4.17)$$

In order to be able to start iterating over a given line there are just two pieces of

information missing, namely the initial pixel coordinates and the α_u , the maximum step in each direction for a unit of change. The initial pixel coordinates can be computed as

$$i = \left\lfloor p_x \left(\frac{\min(\alpha_x, \alpha_y) + \alpha_{min}}{2} \right) \right\rfloor \quad (4.18)$$

$$j = \left\lfloor p_y \left(\frac{\min(\alpha_x, \alpha_y) + \alpha_{min}}{2} \right) \right\rfloor. \quad (4.19)$$

The maximum α that can happen in a unit of change in each direction, or α_{xu} and α_{yu} are defined as in equation 4.20. Additionally it is useful to have a variable that controls the unit direction of the ray, i_u and j_u , as in equation 4.21.

$$\alpha_{xu} = \frac{1}{|p_{x2} - p_{x1}|} \quad (4.20)$$

$$i_u = \begin{cases} 1 & \text{if } p_{x1} < p_{x2} \\ -1 & \text{otherwise} \end{cases} \quad (4.21)$$

Defining l_{tot} as the Euclidean distance between p_1 and p_2 and initializing the current α , $\alpha_c = \alpha_{min}$, the iterative method to follow the X-ray path can be described as follows. Check if the next intersection is in x or y by comparing the α values of each direction, then choose to update the direction that has a smallest α . When updating, compute the length of the next distance and update the α , pixel index and integral values. The update when $\alpha_x < \alpha_y$ can be seen in equations 4.22-4.25, and the opposite case in equations 4.26-4.29.

$$d_{ray} = d_{ray} + (\alpha_x - \alpha_c) \cdot l_{tot} \cdot \mathbb{I}(i, j) \quad (4.22)$$

$$i = i + i_u \quad (4.23)$$

$$\alpha_c = \alpha_x \quad (4.24)$$

$$\alpha_x = \alpha_x + \alpha_{xu} \quad (4.25)$$

$$d_{ray} = d_{ray} + (\alpha_y - \alpha_c) \cdot l_{tot} \cdot \mathbb{I}(i, j) \quad (4.26)$$

$$j = j + j_u \quad (4.27)$$

$$\alpha_c = \alpha_y \quad (4.28)$$

$$\alpha_y = \alpha_y + \alpha_{yu} \quad (4.29)$$

This process is repeated N_p times and, while there may be degenerate cases where a

cross-section between an x and y plane is repeated, the algorithm will compute a length of zero the second time, thus resolving the situation without need of a check.

This algorithm is highly parallelizable. It needs no memory but for a few scalars and, once the values of the required variables are computed, the iterative process that takes most of the time is defined by 4 simple equations. A few straightforward optimizations are also possible, such as multiplying by l_{tot} outside the for loop, in the end of the iterative process and precomputing the few scalar operands that are reused during the process to minimize the number of algebraic operations.

From the iterative section, the memory reads, $\mathbb{I}(i, j)$, are the most computationally expensive part. As previously commented, a single memory read takes 80 cycles as a best case, compared to just one for an algebraic operator involving two scalars. This is true for proper memory access. If the memory is accessed in a random manner, the memory latency increases massively. Thus making sure that single warps (32 simultaneous threads) read from memory in a similar matter is key. Additionally, *thread divergence* can slow down the overall execution. Thread divergence refers to the case where, due to control flow such as a different path in an **if** condition, threads compute different things and finish at different times. If this happens, they will stay idle until the slowest threads are finished, effectively wasting time. In order to decrease memory latency, texture memory is used. One of the features of texture memory is that the cache will assume data locality, thus loading a chunk of memory around the sampled value. If threads read around it, then the memory reads are faster. In order to implement that, the X-rays are divided into $\text{divU} \times \text{divV}$ pieces, and launched in each block together, as seen in figure 4-4. This ensures that the all rays are as close to each other as possible and hence that samples are taken next to each other. Interestingly, this approach also minimizes thread divergence, as X-rays very close to each other will cross each voxel boundary in a similar manner, and will most likely have the same N_p number of intersections. It is important to note though that the figure oversimplifies the real case scenario. The concurrent memory reads are not happening in a parallel plane to the detector as, due to the cone angle, some paths are longer than others and some paths can intersect more voxels than others. However, if $\text{divU} \times \text{divV}$ is small enough, then this divergence is small enough that it has no effect on the computation time because the difference in the source-to-detector direction is still within the cached memory size.

4.3.2 Grid-interpolated methods

The grid-interpolated method is significantly less complex than the ray-voxel intersection method. As shown in figure 4-2(b), it merely relies on sampling the X-ray

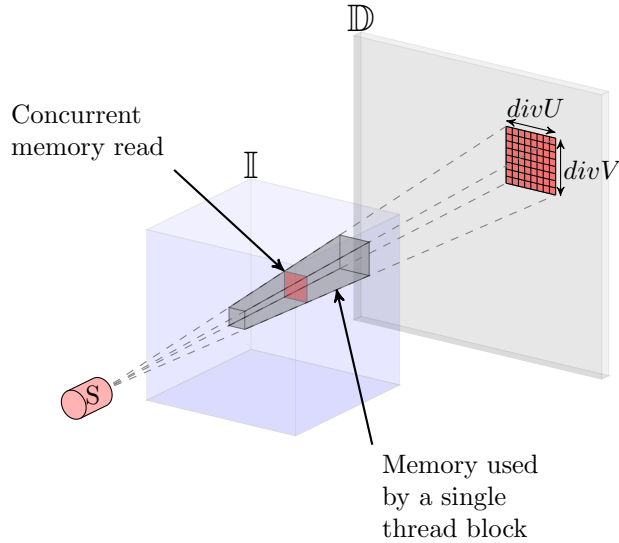


Figure 4-4: Diagram of the block level execution and memory access to increase data locality. Each block is composed of $divU \times divV$ rays, which are executed in parallel. This ensures that the concurrent memory reads are spatially adjacent, thus decreasing memory latency.

paths with a uniform Euclidean sampling rate. It can be described using equation 4.30 and its pseudocode is given in 4.

$$d_{(uv)} = \sum_{\alpha} \Delta l * \mathbb{I}(p_x(\alpha), p_y(\alpha), p_z(\alpha)), \quad (4.30)$$

where α is the parameter of the line equation and takes decimal values between 0-1 if defined in terms of the source and detector locations (see equation 4.2). Note that now the image \mathbb{I} is sampled using not integer values, but decimal values, thus requiring interpolation. The texture memory cache includes hardware accelerated linear interpolation, so this is interpolation method used. Whereas in equation 4.1 the length in this projection method, Δl , is a constant the same for all samples and thus can be taken out of the summation.

The memory latency is significantly decreased by choosing the same structure for block and thread organizing as used in the other method and shown in figure 4-4. The sampling rate of α is the relevant parameter to set and, as discussed by Jia *et al*[25], it defaults to half the voxel size to ensure all data are used. The implementation in TIGRE additionally blocks the user from choosing a sampling rate larger than a voxel by limiting it to that size and changing the interpolation to nearest neighbour.

This method of projection is arguably more realistic than the ray-voxel projection

Algorithm 4 Grid interpolated projection

- 1: Precompute geometric constants
- Require:** N_{ray} threads organized in $\text{divU} \times \text{divV}$ blocks
- 2: **for** X-ray path **do**
- 3: Compute $[x_p, y_p, z_p]$ sample position
- 4: Sum+= $\text{Image}(x_p, y_p, z_p)$
- 5: **end for**
- 6: $\text{Detector}(u, v) = \Delta l \cdot \text{Sum}$

Ensure:

in the case where the voxel size is very big (the resolution is very low) as it treats image information as a continuous domain instead of square boxes.

4.3.3 Comments on optimization

In order to minimize the computation times several optimization tricks have been used in both projection types. As one of the challenges of GPU programming is that often the only way of knowing how to accelerate code or what approach to use is intuition and testing, describing the optimization tricks and tests used for acceleration can be important. Three tricks that are worth mentioning are implemented, namely choosing an optimal coordinate system, precomputing geometric unit changes, and the way out of bounds memory is handled. Aside from these, other small tweaks can be found in the code, such as never computing trigonometric functions inside the kernels, but they are all relatively trivial and no further comment on them will be made.

Optimal coordinate system

When designing a kernel one of the main considerations is to minimize the amount of arithmetic operations happening inside. In tomography specifically, the geometry is the most variable of the parameters. Images can be arbitrarily fine or coarse and voxels can be anisotropic with a wide range of sizes in each direction and so can the detector. Thus, when writing the kernel, a coordinate system is needed that can accommodate the flexibility of the geometry while still being minimal in arithmetic operations. In TIGRE, the following has been chosen for the projector operator.

As the image memory is static, and data needs to be sampled from it in the projection coordinate system, the image will never move, while the detector and the source will rotate around the axis of rotation. Thus the new system (x_p, y_p, z_p) is aligned with the image edges and it is centred at the first lexicographically indexed voxel, at the bottom corner of the image as seen in figure 4-5. Additionally, the units of the new system are set as voxels, regardless of the size of the voxels in each direction. This

new system reduces the amount of arithmetic operations as each sample point is now an index in the image memory, while in each kernel the vector from the source to the detector position must be computed arithmetically. Thus, in the main loop where the new sample location is needed, once the next point in the line is computed no more operations are needed to convert to memory index. This alone saves a significant time.

Precomputation of geometry

In order to generate the new coordinate system, some transformations need to be applied to the input geometry, as the units, source location and detector locations need to be set up. All these operations are performed outside the kernel and output 2 points and 2 vectors. The points are the location of the source and first detector pixel with respect to the new coordinate system origin, rotation angle and other geometric definitions. The vectors describe the unit change in projection coordinate systems of the detector pixel location, thus by knowing the location of the first detector pixel and their unit changes, finding any detector pixel location from its index is trivial.

Additionally, the advantage of structuring the geometry computations as described is that new geometric transformations can be implemented with zero increase in computational cost. For example, the addition of the rotation with 3 degrees of freedom of the detector, offset of the image with respect to the axis of rotation or offset of the detector implies no change in computational cost, the only change needed is the change in the 2 points and vectors described.

Sampling outside the image

In the ray-voxel method, sampling outside the image is not a worry as the amount of cross-sections and the initial intersection are computed in the algorithm. However, in the grid-interpolated method, a start and end point for sampling need to be chosen.

As the texture memory is cached and handled differently than a direct read into memory, it has multiple tunable features. One of these is the possibility of selecting the behaviour when a memory read is out of bounds, which in the case of this work is set to zero. It is important to note that this means the code will not generate an error for out of bounds memory reads. Two versions of the grid-interpolated method can be tested, one where there is a conditional check to see if the current point is inside the image and if true then sample, and another where the line is sampled from the source to the detector. Empirical tests show that avoiding the conditional statement and sampling over the whole path is 33% faster than checking if the sample is within bounds, even with geometry definitions where more than 50% of the samples lie outside the image.

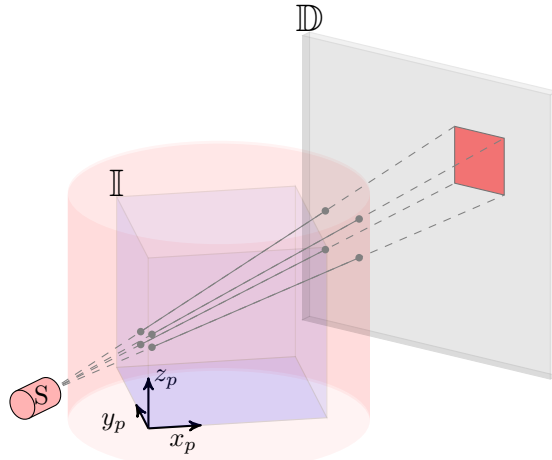


Figure 4-5: Diagram of the projection coordinate system and sampling region. In both projection operations the new coordinate system $((x_p, y_p, z_p))$ has its origin on the lexicographically first voxel center. The red cylinder shows the sampling region for the grid-interpolated method, where the kernels sample from memory.

This can be explained by the fact that CUDA cores are quite slow with code control flow and possibly³ by the cache taking virtually no time returning a zero value when accessed out of bounds.

Sampling the x-ray path from the start to the end is not optimal either, even avoiding conditional statements. To minimize the memory reads, the diameter of a cylinder that encloses the image is precomputed and the rays are sampled from the beginning of the cylinder to either the detector or to the end of the cylinder, whichever comes first. This approach speeds the projection kernel by another 20%. This is shown in figure 4-5.

4.3.4 Differences between operators

The projection operators, while effectively simulating the same physics, have slightly different results due to the methods used. The difference between the two projection operators is enhanced when the voxel size of the images is very big, i.e., when the image has low resolution. Figure 4-6 shows this effect. A projection of the 3D Shepp-Logan phantom is shown at different resolutions for both projection types. In the figure, four image resolutions can be seen for the same size, 64^3 , 128^3 , 256^3 and 512^3 from top to bottom. From left to right the first two columns show the ray-voxel intersection and the grid-interpolated method, while the last two columns show a zoomed in version of

³This is undocumented so, while it is very likely, it is hard to claim with full certainty.

the same projections. Figure 4-7 shows the differences between the projections.

The ray-voxel intersection method does introduce higher aliasing-like artefacts to the projection, as opposed to the interpolating method that smooths everything. Note however that when the image resolution gets higher, the differences are almost indistinguishable. None of the projection modes is better or worse. One could argue that the ray-voxel method aligns better with the discretization of the domain, or that the interpolated method is better because it generates images that are closer to what is measured in a real detector.

When used in reconstruction, the differences between the images reconstructed with algorithms using one or the other projection types are insignificant, with generally a maximum value of about 0.1% of the highest value in the image. This can be seen in figure 4-8, where a reconstruction of the XCAT[57] phantom of size 256^3 using OS-SART with 200 iterations and 100 projections is shown. It shows the result using both projection operators, and figure 4-9 the contrast enhanced differences (the colourmap is enhanced to 10% of the maximum data value) of both reconstructions against the original image. Both reconstructed images are visually very similar and the enhanced difference images show structural differences in the error, but they are still of the same level. The sum of square errors shows a slight higher value for the ray-voxel method, but not big enough to be significant. This difference is even smaller when working with higher resolution images. TIGRE defaults to the interpolated projection in the algorithms.

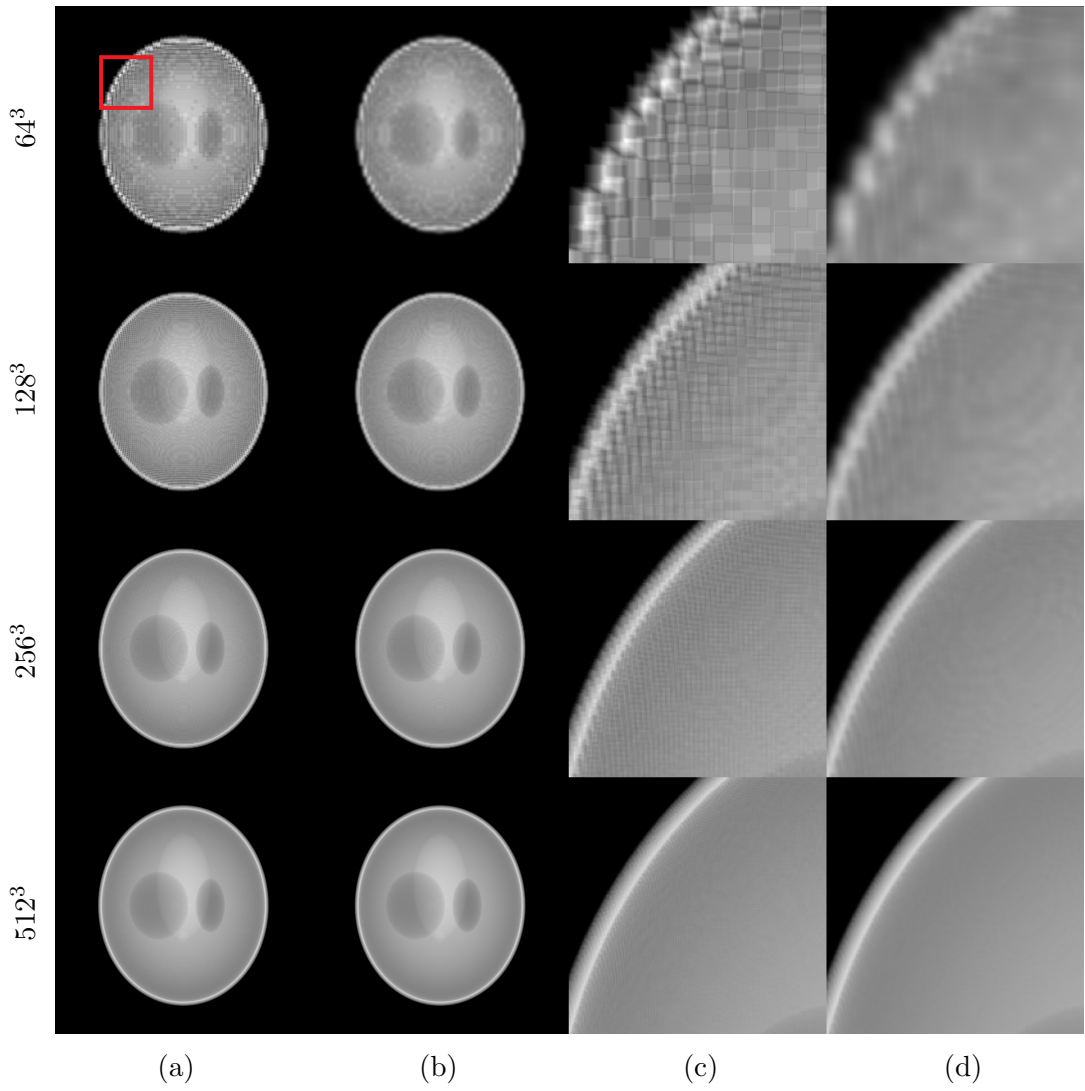


Figure 4-6: Different projection modes for different image resolutions. From top to bottom, the image resolution is 64^3 , 128^3 , 256^3 and 512^3 respectively. From left to right, (a) the ray-voxel intersection projection; (b) the grid-interpolated projection; (c) a zoomed in version of (a); and (d) a zoomed in version of (b).

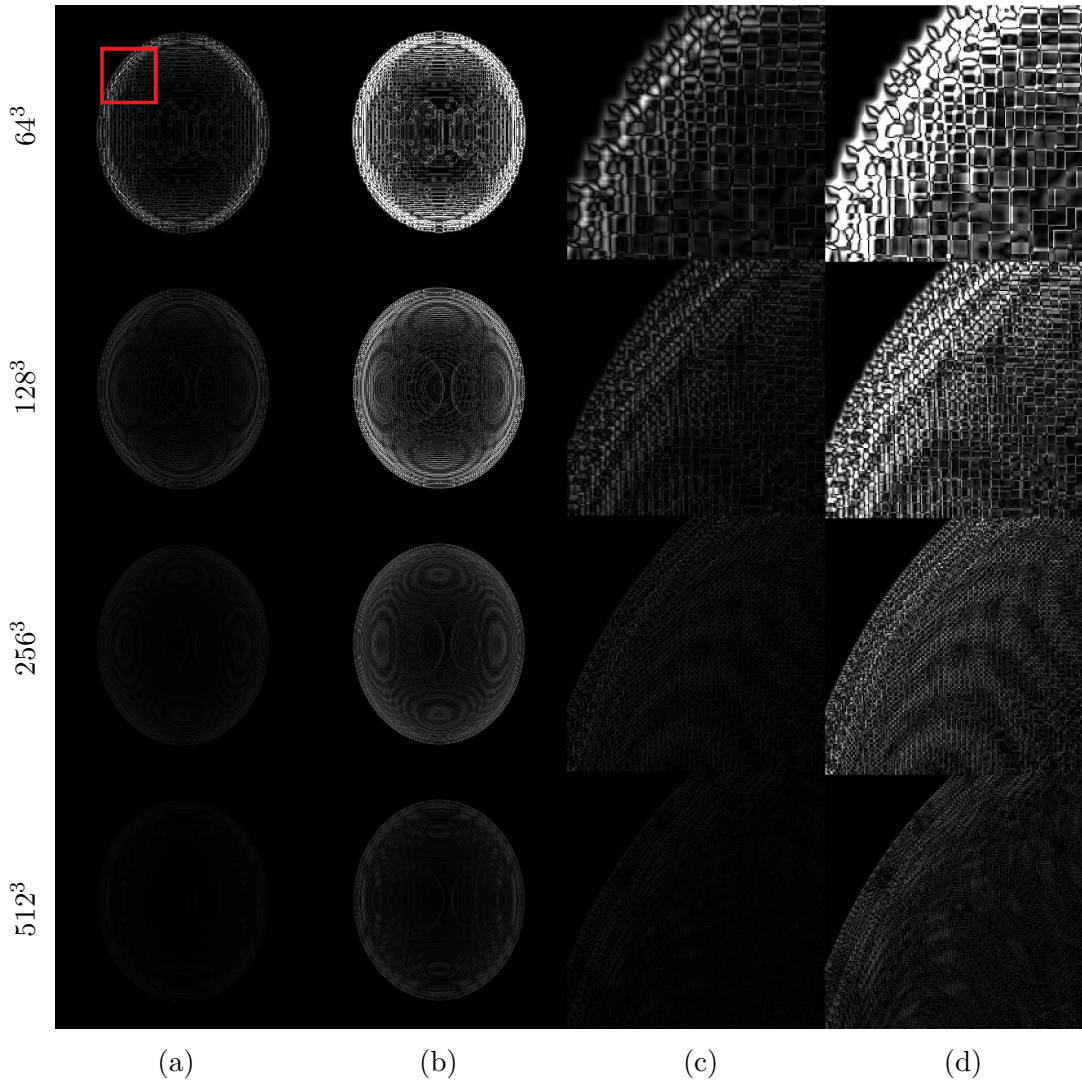


Figure 4-7: Difference between projection modes for different image resolutions. From top to bottom, the image resolution is 64^3 , 128^3 , 256^3 and 512^3 respectively. From left to right, (a) the absolute difference between the projections; (b) contrast enhanced version of (a) by cropping the colourmap to 25% of the maximum; (c) a zoomed in version of (a); and (d) a zoomed in version of (b).

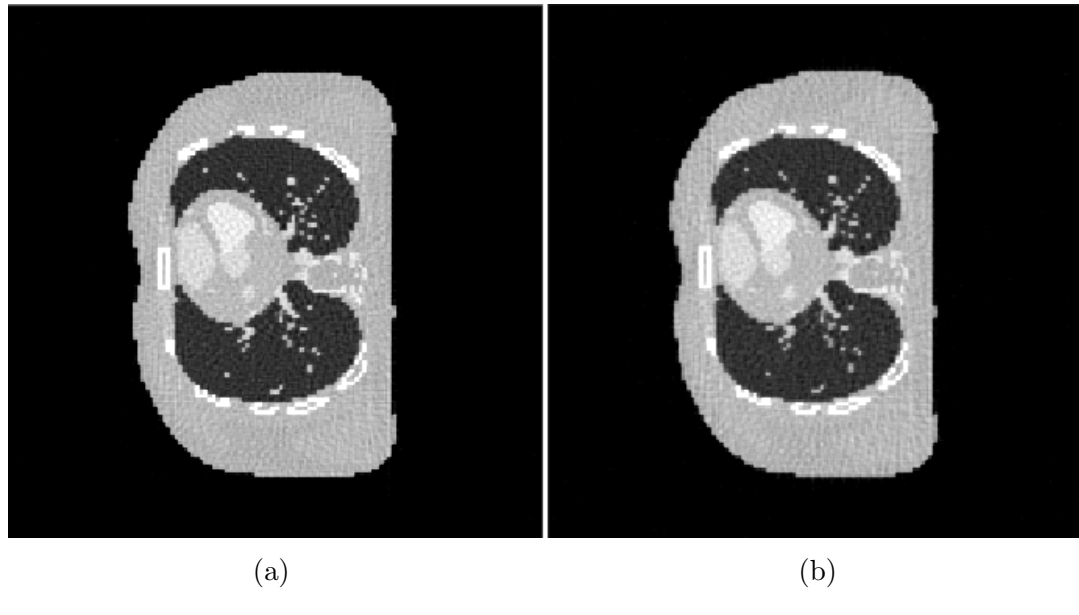


Figure 4-8: XCAT phantom reconstruction of size 256^3 using OS-SART with 200 iterations and 100 angularly uniformly sampled projections. (a) Reconstruction using ray-voxel intersection projection and (b) using the interpolated-projection method.

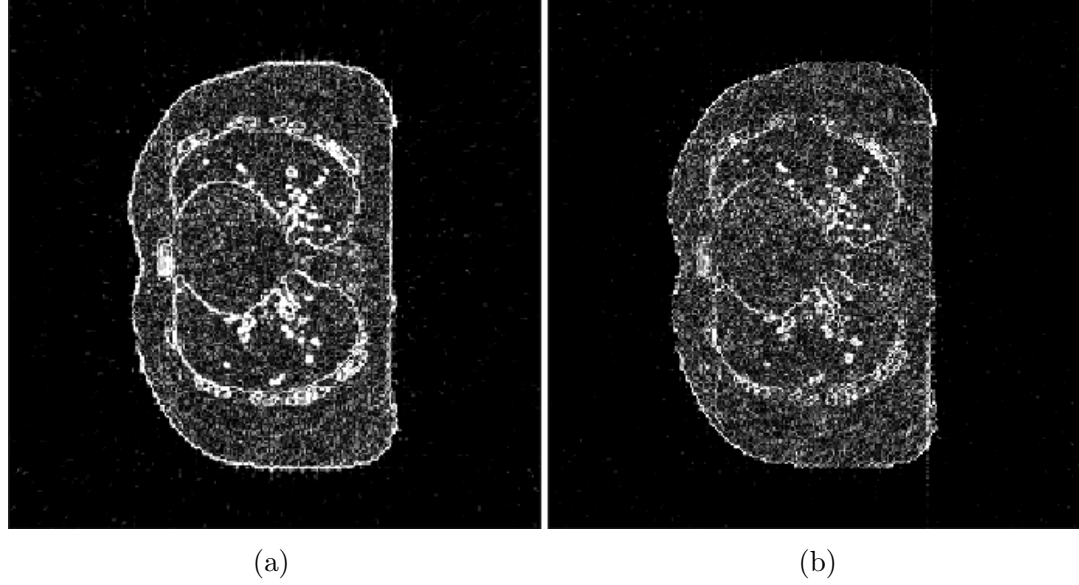


Figure 4-9: Difference between the original XCAT phantom and the reconstructions of figure 4-8. The colour limits have been set to 10% of the maximum intensity of the original data. (a) Difference using ray-voxel intersection projection and (b) difference with the interpolated projection method.

4.4 The backprojection operator

The backprojection operator (or $A^T * b$ in algebraic notation) is the operator that updates the image using the information in the projection images. This update is performed by an operation often described in the literature as a smearing of the projection data into the image, as if it were butter on toast, but following the path from detector to source.

As with projection, multiple methods to perform this operation have been proposed in the literature. The most commonly used method is voxel-driven backprojection[53][42], where the path from the source to each voxel center is generated and extended until the detector is reached. Then the value in the detector is sampled (using interpolation, as it is likely that it does not fall in the center of a pixel) and the voxel value updated.

Other methods include the separable footprints method[37], where the footprint of the voxel in the detector is precomputed and approximated and the voxel values are updated according to the detector values overlapping the voxel footprint. A conceptually similar backprojection relies on having spherical shaped image value representation, instead of square voxels[81]. The backprojection using basis-functions also updates the image values according to the footprint of these spherical voxels.

The distance-driven method[54] is also applicable to backprojection by performing the same operation as for projection: the computation of all voxel-pixel intersections in an imaginary mid-plane. Finally, ray-voxel intersection driven methods also exist[46], in both single ray or multiple ray per voxel modes. This method requires multiple voxel updates per backprojection, but can give a matched result, i.e., the backprojection method is the same as the projection method. This has been shown to give better results[41] and allows the use of any iterative method Krylov subspace methods require matched backprojection.

In this work, voxel-driven backprojection has been implemented. The rationale being that it is a method which is fast and easy to implement yet accurate. Additionally, a quasi-matched backprojection can be implemented to allow Krylov subspace algorithms (see section 4.4.2 for more information). Finally, this method is most appropriate for the method proposed in Chapter 6.

4.4.1 Voxel-driven backprojection

The underlying idea of voxel-driven backprojection is simple, the path between the source and the center of each voxel is computed and the intersection of that path with the detector is computed. Then, the detector is sampled at the intersection point (using interpolation) and the voxel is updated with that value. Due to the cone angle,

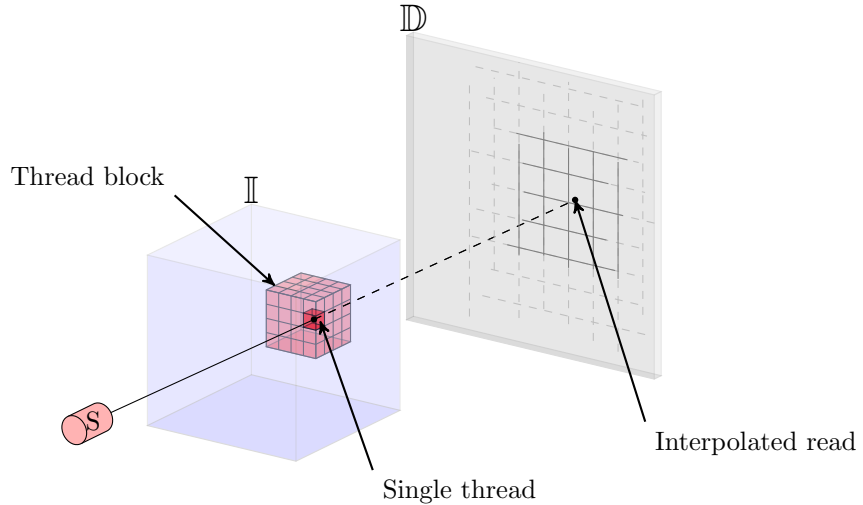


Figure 4-10: Simple voxel-driven backprojection. Each kernel is subdivided into square blocks and each thread updates a single voxel using interpolated memory reads in the detector.

a weighting factor is also applied to each voxel (more details are given in the next section).

To accelerate this operator in a GPU, the naive approach is to assign a thread per voxel and to assign a square amount of threads to a single block (by dividing it into $\text{divX} \times \text{divY} \times \text{divZ}$ threads) to maximize cache hits on texture memory (used for the interpolation of the detector values). The block size is empirically set to 8x8x8 for fastest execution. This approach, shown as a diagram in figure 4-10 and as pseudocode in algorithm 5, does indeed result in a fast kernel. However, the backprojection requires a significantly higher total number of threads than the projection operation, while repeating the same thing for each voxel (in multiple backprojection updates) and reading in the same memory very often. In order to improve the cache memory hits and minimize redundant arithmetic computations, a series of improvements have been studied by Papenhausen *et al*[45] and further optimized by Zinsser *et al* [82].

The main idea behind the optimization is the minimization of memory latency. In order to do that a multiple voxel, multiple projection per thread kernel is designed. If in each of the threads when a single voxel is updated multiple projections (32 in this case) are used, these will be spatially nearby, thus the L2 cache will speed up the memory reading process provided the angular distance between projections is small. Additionally, if each of the threads computes a small subset of voxels ($N_{voxelThread}$) in the z direction (8 in this case), not only are the memory cache hits are likely to be

Algorithm 5 Naive voxel-driven backprojection

```
1: for Projection do
2:   Precompute geometric constants
Require:  $N_{voxel}$  threads organized in  $\text{divX} \times \text{divY} \times \text{divZ}$  blocks
3:   Compute  $[u, v]$  sample position
4:   Compute  $w$  weight
5:    $\text{Image}(x, y, z) += w \cdot \text{Detector}(u, v)$ 
Ensure:
6: end for
```

increased, but also the computational operations reduced as the computation of the location of each voxel requires fewer operations. In general these tweaks increase the occupancy of the SMs, decreasing the amount of time the threads stand idle waiting for memory. The diagram of the new optimized kernel is shown in figure 4-11 and its pseudocode is given in algorithm 6. The code is divided in pieces to allow each block to have $\text{divX} \times \text{divY}$ threads each (16×32 in this case). To minimize global memory reads, the image voxel values that are updated in each kernel are pre-loaded. Then, for each projection, the geometric constants that describe the location of the detector and image pixels are loaded from constant memory. Next, the backprojection is performed for each voxel being updated. This approach further increases occupancy as in execution the thread does not wait for the memory read to finish before computing the next loop, thus hiding memory latency even more. Finally, the image is updated with the auxiliary variable. This step also decreases the memory latency, as fewer global memory write operations are needed.

4.4.2 Backprojection weights

Due to the cone shape the backprojection needs a weight for each voxel, as different paths have different ray lengths and hence have a different effect in the detector. In the projection operator, the length of the path is used in each detector pixel as a weight for the update, but in the backprojection operation the weight is not as straightforward to compute. In the algebraic definition of iterative algorithms, the weight of each voxel is the length of a specific ray within that voxel. If the matrices were fully known, it would be straightforward to compute (as it is the sum of the columns of A), however this doesn't apply to voxel-driven backprojection. In the GPU version, a projection to compute such lengths per backprojection would be needed, ultimately slowing the code considerably.

Algorithm 6 Optimized voxel-driven backprojection

```

1: for  $N_{kernels}$  do
2:   Precompute geometric constants per projection
Require:  $\text{divX} \times \text{divY}$  threads organized in  $\frac{N_x}{\text{divX}} \times \frac{N_y}{\text{divY}} \times \frac{N_z}{N_{voxelThread}}$  blocks
3:   for  $N_{voxelThread}$  do
4:     auxImage(voxThread)=Image( $x, y, z$ )
5:   end for
6:   for Projections (in this kernel) do
7:     Load geometric constants for this projection
8:     for  $N_{voxThread}$  do
9:       Compute  $[u, v]$  sample position
10:      Compute  $w$  weight
11:      auxImage(voxThread) $+=w \cdot \text{Detector}(u, v)$ 
12:    end for
13:   end for
14:   for  $N_{voxThread}$  do
15:     Image( $x, y, z$ )=auxImage(voxThread)
16:   end for
Ensure:
17: end for

```

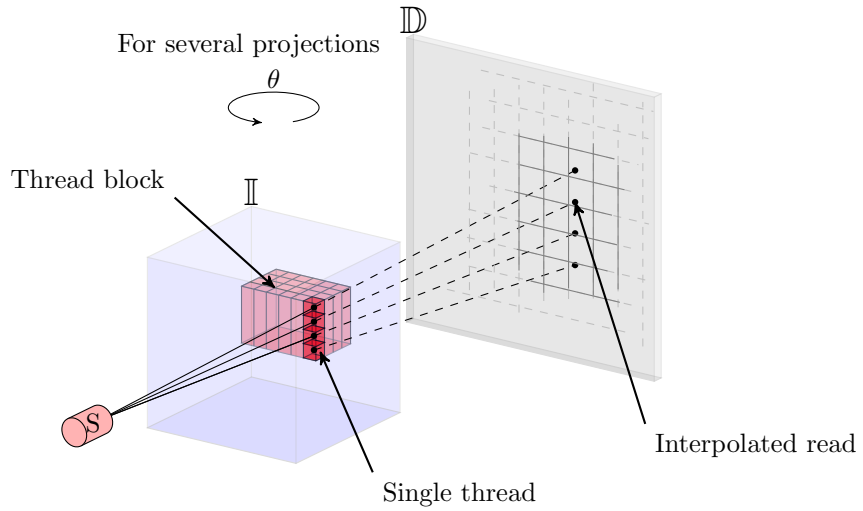


Figure 4-11: Optimized voxel-driven backprojection. Each kernel is subdivided into blocks and each thread updates a series of vertical voxels using interpolated memory. Each kernel additionally operates in a series of projections, not in a single one.

FDK weights

A simple approach is to use the weights of the FDK algorithm as backprojection weights. As described in section XX, the FDK backprojection weight is computed as

$$w_{x,y} = \frac{R^2}{(R + y \cdot \sin \theta - x \cdot \cos \theta)^2}, \quad (4.31)$$

where R is the distance from the source to the axis of rotation, θ the projection angle and x and y the location of the voxel. Note how this equation is independent of z , thus the weights can be precomputed after line 7 (instead of line 10) in algorithm 6, resulting in a minor speed-up.

Pseudo-matched weights

The FDK weights are good in the iterative algorithms that normalize the result of the backprojection afterwards (such as SART), as the overall scale and effect of the backprojections is removed in the algorithm by an opposing weighting factor. However, some algorithms require matched backprojection, i.e., a backprojection operator that is mathematically equivalent to the adjoint of the projection operator. This is not the case with FDK weights. Algorithms such as CGLS cannot work unless a matched backprojection is implemented. As previously explained, a fully matched backprojection, while possible, would slow down the kernels considerably due to the need of also computing projection operations in the backprojection. However Jia *et al*[26] propose a weight to match the backprojection.

In order to derive the weight, a functional analysis approach needs to be taken. For the sake of simplicity and cohesion with Jia *et al*, the notation in this section differs from the rest of the thesis.

If an image is represented as a function $f(\mathbf{x})$, where $\mathbf{x} = (x, y, z) \in \mathbb{R}^3$, a projection operator A^θ maps $f(\mathbf{x})$ onto a different function on the projection plane with angle θ as:

$$A^\theta[f](\mathbf{u}) = \int_0^{L(\mathbf{u})} dl f(\mathbf{x}_s + \mathbf{n}l), \quad (4.32)$$

where \mathbf{x}_s is the coordinate of the source, \mathbf{n} a unit vector in the projection direction and $\mathbf{u} \in \mathbb{R}^2$ the coordinates in the detector. $L(\mathbf{u})$ is the length of the X-ray path.

Let $f(\cdot) : \mathbb{R}^3 \rightarrow \mathbb{R}$ and $g(\cdot) : \mathbb{R}^2 \rightarrow \mathbb{R}$ be smooth enough functions in image and projection domain respectively. In order to have an operator $A^{\theta T}$ that is the adjoint of A^θ , it should satisfy the condition

$$\langle f, A^{\theta T} g \rangle = \langle A^\theta f, g \rangle, \quad (4.33)$$

where $\langle \cdot, \cdot \rangle$ is the inner product. In integral form, this inner product equality can be expressed as

$$\int d\mathbf{x} f(\mathbf{x}) A^{\theta T}[g](\mathbf{x}) = \int d\mathbf{u} A^\theta[f](\mathbf{u}) g(\mathbf{u}), \quad (4.34)$$

or if the functional derivative of both sides with respect to $f(\mathbf{x})$ is taken, then as

$$A^{\theta T}[g](\mathbf{x}) = \frac{\partial}{\partial f(\mathbf{x})} \int d\mathbf{u} A^\theta[f](\mathbf{u}) g(\mathbf{u}). \quad (4.35)$$

Equation 4.35 can be rewritten as

$$A^{\theta T}[g](\mathbf{x}) = \int d\mathbf{u} g(\mathbf{u}) \frac{\partial}{\partial f(\mathbf{x})} A^\theta[f](\mathbf{u}), \quad (4.36)$$

and equation 4.32 can be rewritten as equation 4.37 using a delta function.

$$A^\theta[f](\mathbf{u}) = \int d\mathbf{l} d\mathbf{x} f(\mathbf{x}) \delta(\mathbf{x} - \mathbf{x}_s - \mathbf{n}l). \quad (4.37)$$

Finally, by substituting equation 4.37 in 4.36, the adjoint of the projection operator can be expressed as

$$A^{\theta T}[g](\mathbf{x}) = \int d\mathbf{l} d\mathbf{u} g(\mathbf{u}) \delta(\mathbf{x} - \mathbf{x}_s - \mathbf{n}l) = \frac{L^3(\mathbf{u}^*)}{L_0 l^2(\mathbf{x})} g(\mathbf{u}^*), \quad (4.38)$$

where \mathbf{u}^* is the intersection point between the x-ray path and the detector plane, $l(\mathbf{x})$ the distance between the source and a voxel, and L_0 the source to detector distance. This equation, however, applies to the integral form of the description of the system, while ultimately in the computer the matrix form is used. By changing the inner product to a vector form, the final adjoint over all projections becomes

$$A^{\theta T}[g](\mathbf{x}) = \frac{\Delta x \Delta y \Delta z}{\Delta u \Delta v} \sum_\theta \frac{L^3(\mathbf{u}^*)}{L_0 l^2(\mathbf{x})} g^\theta(\mathbf{u}^*), \quad (4.39)$$

where $(\Delta x, \Delta y, \Delta z)$ are the sizes of each voxel in each direction and $(\Delta u, \Delta v)$ the sizes of the detector pixels.

This backprojector weight is very close to a matched backprojection operator. According to Jia *et al* the numerical errors are less than 1%. This work did not replicate their results. This mismatch can lead to inaccuracies in Hounsfield units in the final reconstruction and to divergent behaviour in the Krylov subspace algorithms, but only in late iterations.

4.4.3 Comments on optimization

To have a fast execution of the code, as for the projection, a geometry that minimizes the amount of arithmetic operations inside the kernels is proposed. The backprojection coordinate system (x_b, y_b, z_b) is defined to have unit sizes of the detector pixel size in u, v for y_b and z_b respectively, and 1mm in x_b . The origin of the system is located in the center of the first lexicographically ordered pixel in the detector and is always aligned to the detector (i.e., the image rotates while the detector-source system stays in the same location). All precomputing operations performed in the projection geometry are also performed in here.

In the CUDA sense, two extra optimizations have been performed. By defining `divX`, `divY` and `NvoxelThread` (from algorithm 6) as compilers, an instruction to the CUDA compiler can be passed to unroll all the loops. Loop unrolling refers to replacing a for loop by a repetition of each line of code per iteration, one after the other. By doing this, the kernel does not need to have flow control (loop iteration, condition, variable) that needs increasing and checking, thus increasing the total kernel performance by 20% in our case. A small speed-up is also obtained by defining the texture memory as layered memory, thus disabling interpolation in the third dimension.

4.5 Benchmark

This section shows the computational times for the projection and backprojection kernels. This section does test the performance of the kernels themselves, but the actual calls to the kernels do have some overhead of memory input and output, as it is a significant amount of memory that needs to be moved in every call. All computational time results show time per projection, for different image and projection sizes. Figure 4-12 shows the projection times in milliseconds for both ray-voxel intersection and grid interpolated projection modes. The projection operation is dependent in both detector an image size, and it takes about the same time for both types of projection, with maximum of 100ms with 1024^2 detector and 1024^3 image.

Figure 4-13 shows the backprojection times for FDK weights and pseudo-matched weights. As the kernels are optimized for adjacent projection calls the computational times do not scale with more projections, a test using the maximum projections per kernel is also performed. Figure 4-14 shows kernel times per projection when multiple projections are updated. The maximum computational time on these tests (1024^2 detector with 1024^3 image) show 75ms and 180ms for the FDK and pseudo-matched weights when a single projection is used, but 45ms and 99ms per projection when 32 projections (maximum simultaneously used projections in a single kernel) are used.

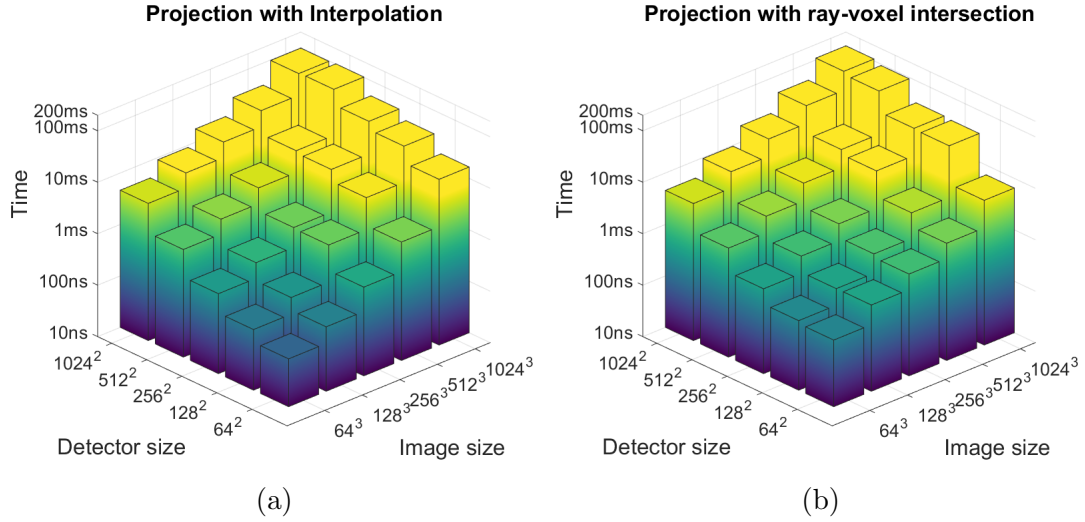


Figure 4-12: Computational times per projection for the projection operation for (a) grid interpolated (2 samples per voxel) and (b) ray-voxel intersection modes.

Note that generally the pseudo-matched weights are slower. This is explained by the fact that the chosen kernel structure completely masks the memory latency with FDK weights, but with matched weights the arithmetic operations for the weight need both more computations and registers, thus slowing down the kernel significantly. Additionally an extra multiplication kernel is needed for the final normalization from equation 4.39. Note also how the backprojection times are not dependant on the projection size, only in the image size. This is not a big surprise, considering how the kernels are designed.

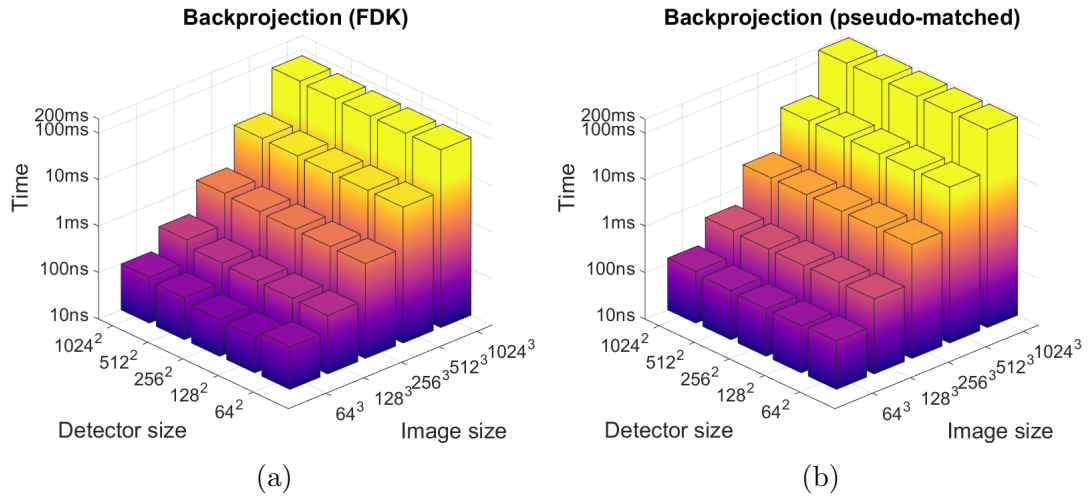


Figure 4-13: Computational times per projection for the backprojection operation when launched with a single projections for (a) FDK weights and (b) pseudo-matched weights.

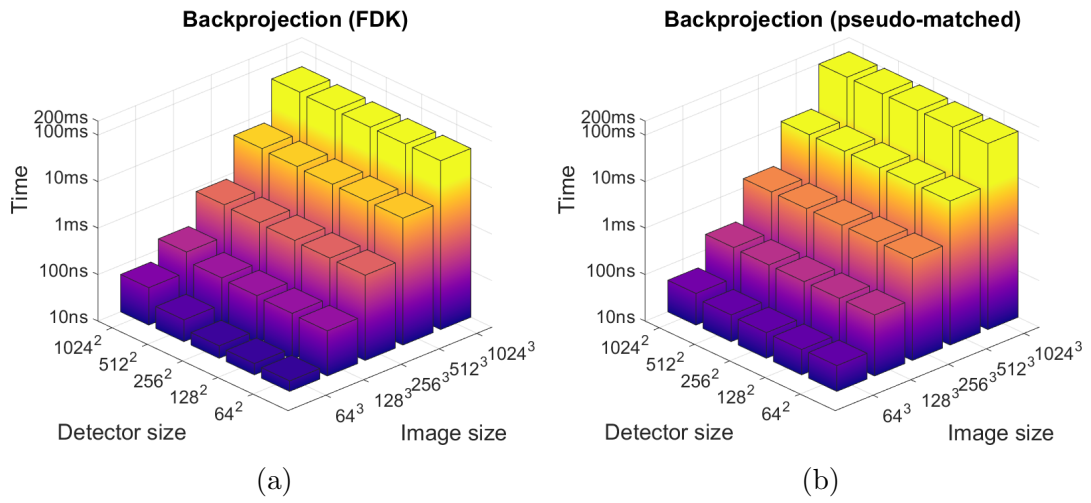


Figure 4-14: Computational times per projection for the backprojection operation when launched with 32 projections for (a) FDK weights and (b) pseudo-matched weights.

4.6 The TIGRE toolbox

In order to have an easy tool to implement algorithms but still have the GPU acceleration on hand, a MATLAB-CUDA toolbox has been created, the Tomographic Iterative GPU-based Reconstruction toolbox, or TIGRE toolbox. TIGRE is a modular, easy to use fast toolbox for cone and parallel beam computed tomography, focusing in the implementation of a variety of iterative reconstruction algorithms. All four families of algorithms described in chapter 3 are implemented in TIGRE, namely, FDK, statistical inversion (MLEM), the gradient descend family (SART,OS-SART,SIRT), Krylov subspace family (CGLS) and TV regularized family (ASD-POCS, OS-ASD-POCS, B-ASD-POCS- β , SART-TV). This section describes the features of TIGRE, the geometry supported, the general structure of the toolbox and how to implement an algorithm on it. This section is partially based in article [6].

4.6.1 Geometry in TIGRE

The geometry of CBCT in TIGRE can be represented as in figure 4-15. An X-ray source, S , is located at distance DSO from a centre of rotation O , where the origin of a cartesian coordinate system is located. The X-ray source irradiates a cone-shaped region containing the image volume \mathbb{I} and a detector \mathbb{D} measures the intensity of the photons attenuated following the Beer-Lamber law. The image is centred at position O' , which is displaced by $\overrightarrow{V_{orig}}$ from the coordinate system origin. The detector, located at distance DSD from the source and centred at D' , has an offset of $\overrightarrow{V_{det}}$ from D , which is a point lying in the xy -plane at distance $DSD - DSO$ from the origin. A projection coordinate system uv is defined centred at the lower left corner of the detector. During the measurement acquisition, the source and the detector rotate around the z -axis at an angle of θ from their initial position. Additionally, the detector can rotate on its own center by 3 axis of rotation, useful to account for mechanical errors[CITE]. Finally the center of rotation (COR) offset has also been implemented, a common offset in CT machines where the sample rotates, instead of the detector-source system.

While the diagram shows the geometry for CBCT, TIGRE also supports 3D parallel beam geometry, and by setting the offsets of the image accordingly, helical beam geometries. Additionally, if a correct size of the detector is chosen the geometry can be modified to allow 2D reconstruction, however TIGRE is not designed for 3D geometries, as GPU accelerations in 2D are not essential. Code snippet 4.1 shows the code to define the geometry in TIGRE.

The geometric variables described above are used in the TIGRE Toolbox to perform the necessary operations for image reconstruction, as shown in code snippet 4.1. It is

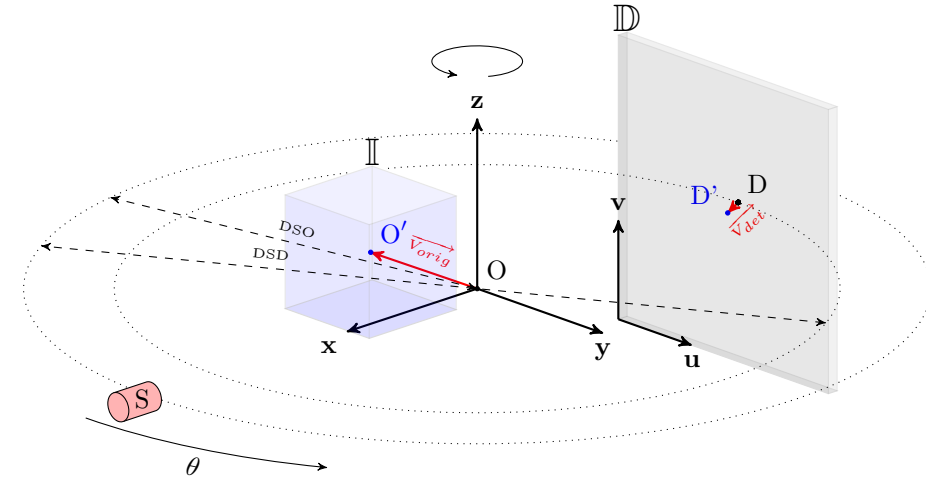


Figure 4-15: Diagram of the geometric definition of a TIGRE reconstruction. Image, and detector offsets are supported, as well as any arbitrary size for the image and the detector, both total and pixel-wise.

worth mentioning that both \vec{V}_{det} , \vec{V}_{orig} , COR and the rotation of the detector are vectors that can be defined per projection angle θ .

Code Snippet 4.1: Geometry definition in TIGRE

```
%>>> %% Geometry structure definition.
% Distances
geo.DSD = 1536; % Distance Source Detector
geo.DSO = 1000; % Distance Source Origin
% Detector parameters
geo.nDetector=[512; 512]; % number of pixels
geo.dDetector=[0.8; 0.8]; % size in mm of each pixel
geo.sDetector=geo.nDetector.*geo.dDetector; % total size of the detector in mm
geo.rotDetector=[0;0;0]; % euler angles of the rotation
% Image parameters
geo.nVoxel=[512;512;512]; % number of voxels in the image
geo.sVoxel=[256;256;256]; % total size of the image in mm
geo.dVoxel=geo.sVoxel./ geo.nVoxel; % size in mm of each voxel
% Offsets
geo.offOrigin =[0; 0; 0]; % V_orig
geo.offDetector=[0; 0]; % V_det
geo.COR=0; % Centre of Rotation offset
```

4.6.2 Structure

TIGRE has been designed to be modular, in order to facilitate prototyping with instant acceleration and to allow easy of the toolbox. The main building blocks are the projection ($A(x)$) and back projection ($A^T(b)$) operators. In the TIGRE Toolbox,

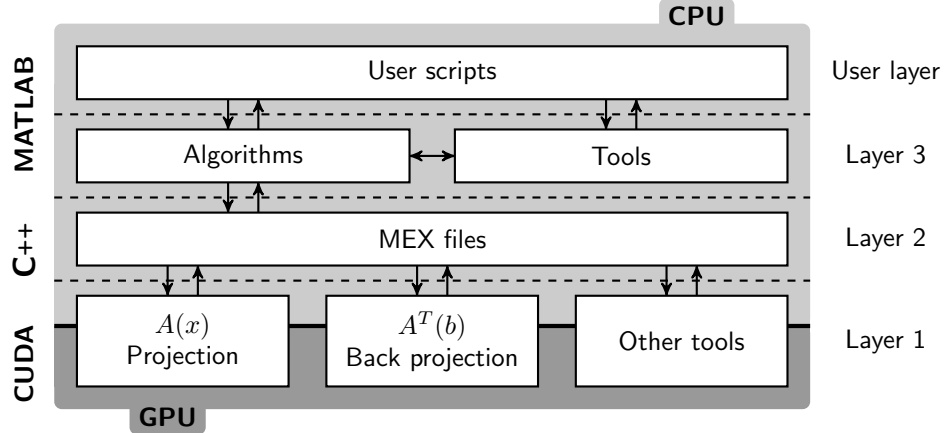


Figure 4-16: Diagram of the structure on TIGRE toolbox.

these two blocks have been optimized for GPU computing using CUDA, as described in the beginning of this chapter. They lie in the lowest layer of the toolbox design and are constantly used by the other layers. The algorithms themselves lie in the topmost layer and are all coded in MATLAB, which provides the power and flexibility of a high-level language. To be able to communicate between the low-level, hardware-oriented CUDA and the high-level, design-oriented MATLAB, a set of the so-called *MEX functions* are needed. The toolbox has been designed not to have any specific data types or classes. Instead, it comprises only the basic MATLAB types, such as matrices and structures.

The high level algorithms are designed to have multiple parameters and full customization. The only required parameters to all algorithms are the data, geometry, angles and number of iterations. Each algorithm has a series of tunable parameters. Generally every parameter affecting the algorithm can be set up to have a different value, allowing users that want to study algorithm behaviour full customization, but having default parameters in case the users want an easy-to use algorithm. Multiple algorithm initialization modes, angle ordering schemes and other features are also available.

Using TIGRE

This code demonstrates the reconstruction of the RANDO head phantom (data obtained in the Christie Hospital, Manchester, UK) using three different algorithms with the geometry defined in code snippet 4.1. The data set contains 360 equidistant projections. Once the data have been loaded using the code of snippet 4.2, the results of figure 4-17 can be obtained without the need for any more code. Information about

total computation time and computation time per iteration are shown. Only some of the possible optional parameters to the algorithms are shown in the snippet. The reader is referred to the published documentation for advanced options and for insight into their numerical ranges.

Code Snippet 4.2: RANDO head data reconstruction

```
% Define Geometry & load data

% From the data, the projection angles (in radians) must have been read
angles= 0:359*pi/180; % as an example

%% Reconstruct image with different algorithms
% FDK
imgFDK=FDK(data , geo , angles );
% CGLS
iterCGLS=15;
imgCGLS=CGLS(data , geo , angles , iterCGLS);
% OS-SART with multi-grid initialization
iterOSSART=70;
imgOSSART=OS_SART(data , geo , angles , iterOSSART , 'BlockSize' ,20 , 'Init' , 'multigrid' );
```

Implementation of an algorithm in TIGRE

To demonstrate the facility with which anyone can develop new algorithms using the TIGRE toolbox, this section presents a side by side comparison of an algorithm definition and its TIGRE equivalent code, using the GPU accelerated features. For the sake of brevity, the CGLS algorithm has been chosen. In table 4.1 the definition of the CGLS iterations and the implementation in TIGRE are shown. From the code snippet, it is worth highlighting the limited use of library related functions, as one of the strengths of TIGRE for the developer point of view is the easy to use Application Programming Interface (API). The only difference in the code from a completely standard MATLAB script is the use of the function Ax() and Atb(), the main building blocks of the toolbox. This allows anyone with MATLAB code for solving image reconstruction to easily modify their code by just changing the matrix-vector operations by TIGRE GPU functions. Note that the functions inside TIGRE do generally have more code than the one shown here, as several options and performance enhancing MATLAB tools are used.

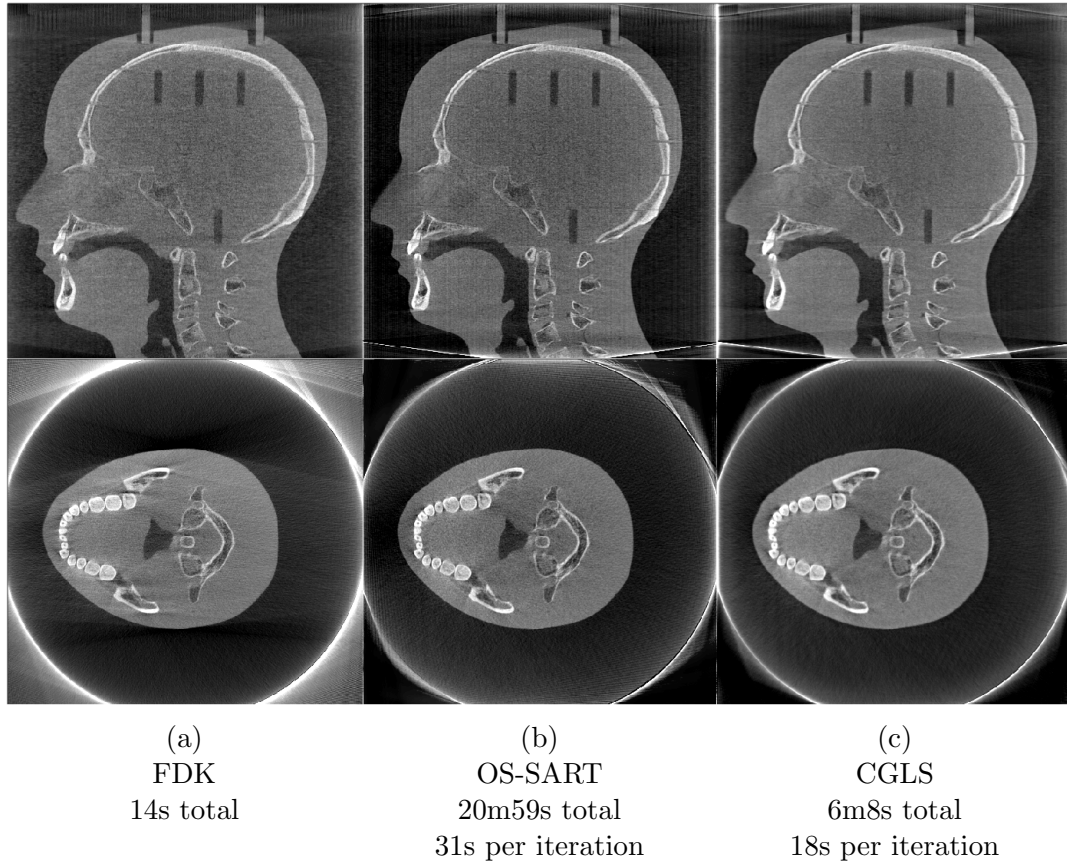


Figure 4-17: RANDO head phantom reconstructed with (a) FDK, (b) OS-SART 40 iterations and (c) CGLS 20 iterations, for 360 equidistant projections. The computational times are also shown.

Table 4.1: CGLS algorithm as definition, and implemented in TIGRE

```

 $x_0 = 0; d_0 = b; r_0 = A^T b; p_0 = r_0;$ 
 $t_0 = Ar_0; \gamma_{k-1} = \|r_0\|^2;$ 
for  $k = 1$  to  $k = \text{maxiter}$ 
     $\alpha_k = \gamma_{k-1} / \|t_{k-1}\|^2$ 
     $x_k = x_{k-1} + \alpha_k t_{k-1}$ 
     $d_k = d_{k-1} - \alpha_k t_{k-1}$ 
     $r_k = A^T d_k$ 
     $\gamma_k = \|r_k\|^2$ 
     $\beta_k = \gamma_k / \gamma_{k-1}$ 
     $p_k = r_k + \beta_k p_{k-1}$ 
     $t_k = Ap_k$ 
end

```

```

% Initialize variables
x=zeros(geo.nVoxel');
d=b;
r=Atb(b,geo,angles,'matched'); %TIGRE
p=r;
t=Ax(r,geo,angles); %TIGRE
gamma_1=norm(r(:));
% Loop until user defined maxiter
for k=1:maxiter
    alpha=gamma_1/norm(t(:));
    x=x+alpha*t;
    d=d-alpha*t;
    r=Atb(d,geo,angles,'matched');%TIGRE
    gamma=norm(r(:));
    beta=gamma/gamma_1;
    gamma_1=gamma;
    p=r+beta*p;
    t=Ax(p,geo,angles); %TIGRE
end
% x is the solution.

```

4.7 Summary

In this chapter we have presented a MATLAB/CUDA toolbox for fast 3D X-ray image reconstruction. While the toolbox has reasonably good performance – reducing to minutes an image reconstruction with complex iterative algorithms – and a wide variety of tools, improvements are possible.

The projection and back projection operators have been fully implemented in the GPU, but the algorithms are fully in CPU so a memory management overhead exists because the data need to be introduced and extracted from the GPU twice per iteration. This design has been proposed in order to have the algorithms in a high-level language, as an algorithm implementation cycle in a low-level language like C++ is significantly longer than in MATLAB. As an estimate, if the algorithms were written in C++/CUDA directly, an improvement in computation time of up to 50% could be achieved in some cases. However, this would increase the difficulty of adding new algorithms to the toolbox. The final decision was that the advantages of a high-level programming language for new algorithms are better than the possible benefits of dou-

bling the speed, which is already reasonably good.

Further improvements in the core GPU kernels of the toolbox would also be possible. While the speeds reached by this method are arguably state of the art, some improvements to the kernel structure to decrease even more memory latency and computational times have been proposed in the literature. It is impossible to know with certainty that any of the methods published will increase the speed of the code, partly because GPU architecture has changed over the past year massively, thus code may be faster in specific GPUs but slower in others, and partly because most of the published papers do not contain code to be benchmarked against, and use different geometric parameters each. Thompson and Lionheart[67] propose a method that exploits structure similarities and works if the cone angle is smaller than 45 degrees, that is the case of most commercial CBCT machines. The work in this thesis tries not to impose limitations on the possible geometries, but modifying the code to trigger the accelerated version proposed by Thompson and Lionheart is an interesting possibility. Chou *et al*[11] claim speed-up by re-structuring the kernels to launch multiple threads for multiple rays in parallel. While initial trials for replicating the multithreads in the early stages of the work in this thesis failed (as times where not changes) the projection operator has intensively been modified since then. This work has potential to accelerate up to 600% the projection operation according to the article. Finally, the method proposed by Gao[18] claims significant speed-up over the “naive” Siddon’s method, the code provided with their article shows slower execution for both the “naive” and accelerated versions than the code used in this work. Nevertheless, it would be worth implementing their approach.

The backprojection operator has been more optimized than the projection operation, using better techniques, thus speed-wise it is performing well. However, there are certainly faster methods, as TIGRE ranks between 5 and 7 in the RabbitCT⁴ benchmark. The RabbitCT benchmark is also recorded in different machines, thus some of the faster methods are due to multi-GPU parallelism exploits or just simply due to faster GPUs. That said, there is certainly room for improvement. Possibly the biggest improvement to the backprojection would be the implementation of completely matched projection adjoint code, as it leads to better reconstruction[41]. Thompson and Lionheart[67] propose a technique, so does Gao[18].

Comparing the forward and back projection speeds to the ASTRA toolbox[68], TIGRE is 2 times slower at its worst. This can be easily explained by two factors. Firstly, the geometric options for CBCT are more flexible in TIGRE than in ASTRA, thus requiring more floating-point operations. Secondly, ASTRA implements an advanced ray

⁴<https://www5.cs.fau.de/research/projects/rabbitct>

splitting that increases memory latency in the GPU and that makes use of overlaps between X-ray paths at different angles[44]. Adding all the discussed effects that would decrease the time performance, all algorithms run about 3 times more slowly in TIGRE than in ASTRA, which constitutes the state of the art. Numerically, the differences between ASTRA and TIGRE are in absolute value of the order of 10^{-3} , which is about 0.01% in relative terms. This difference can be attributed to accumulated floating point errors due to different numerical approaches in the GPU code.

To speed up further the toolbox, a multi-GPU approach could also be taken. Currently, TIGRE does not support multi-GPU architectures. A further weakness of the toolbox is the small number of functions for data loading and post-processing. However, work will be continued, hopefully filling this gap in the near future. The single GPU limitation of TIGRE also limits the image size. Currently, 12GB is the maximum amount of memory on a GPU board, thus limiting the possible size of the images that can be reconstructed. Nevertheless, there is no problem to reconstruct a 1024^3 image with most algorithms so the maximum image size is still big.

The TIGRE Toolbox has been designed with the objective of reducing the gap between image reconstruction research and the end users of tomographic images. While research in reconstruction creates new algorithms every year, end users only have access to FDK implementations. With these two groups in mind, the toolbox:

- has easy-to-use “black box” algorithms, making it extremely straightforward for researchers who are only interested in the quality of the images to test different algorithms without them requiring any knowledge of how the algorithms work;
- has easy-to-use building blocks (projection and back projection operators) that allow algorithm developers to test new methods using a high-level programming language but with the performance of the lowest level, GPU languages.

The code is released as open source under a BSD 3-clause license, allowing anyone to download, test, modify and improve it. While the toolbox was originally designed for CBCT image reconstruction, an option for 3D parallel-beam CT reconstruction has also been included allowing for more geometries, e.g., synchrotron data. Further tweaking the geometry structure of the toolbox also permits 2D fan- and parallel-beam reconstructions.

The minimum requirements to run the toolbox are strongly dependent on the image size desired, as memory is the strongest limiting factor both on the CPU and GPU side. Generally speaking, any NVIDIA GPU with a compute capability higher than 3.5 would be sufficient to reconstruct arbitrarily large images. We recommend having at least 3 times the desired image size in GPU memory and 8 times in RAM in the computer.

As an example, for a 512^3 image, 2GB of GPU memory and 6GB of computer RAM is the suggested minimum. The computing power (number of processors in the GPU and processor performance of the CPU) will have a strong effect on the speed of image reconstruction.

Chapter 5

Experiments and Applications

In the previous two chapters the mathematical and computational challenges of image reconstruction for CT have been discussed. In chapter 3, a detailed description of a variety of different algorithms has been presented, including the ART family of algorithms, CGLS, MLEM and few TV approaches for smooth reconstruction, as well as the classic FDK reconstruction. Additionally in chapter 4 the computational aspect of CT is discussed, on where the problems computing the exact adjoint of the projection operation and mainly the computational burden of some of the operations have been mentioned. Considering the variety of available methods and the specifics of the implementation of the software developed, the TIGRE toolbox, experiments on how these algorithms compare and behave are due. Further than that, the performance of these algorithm in different experimental datasets is also an important analysis.

This chapter shows experimental analysis on both of the topics. First a variety of convergence analysis with different algorithms using synthetic data are performed, showing the differences not only between algorithms, but also between option on parameter selections. The section tries to illustrate and perhaps help build intuition on all the different parameters and options that each of these algorithms has, both within the algorithms themselves and among the different ones. Additionally some highlights on the practical challenges that the use of the algorithms entail in real applications are given.

In the second section of this chapter, a few examples of some of the algorithms are shown in different CT applications, both cone and parallel beam. Data from various different applications, from medicine to science has been tested using the TIGRE toolbox. While quantitative analysis is not possible with these datasets because the truth is not known, some insight in how the algorithms behave in each case is discussed.

5.1 Algorithm Experiments

This section experiments with a variety of algorithms and parameter within them, and shows how they behave with different synthetic data in simulation studies.

5.1.1 Convergence rates

On chapter 3 the convergence rates of the algorithms has been mentioned, as well as computational times. Different algorithms will reach to different residuals at the same iteration, and thus understanding which ones can converge faster, thus theoretically give a better result earlier, is important. However, at the scale of the CBCT problem, faster no only means reaching a residual that is smaller in the same iterations, as the computational burden of each of the iterations also needs to be considered. And, as the backprojection operator is not exactly the adjoint of the projection operator, an effect that the classic formulation of these algorithms do not take into account can happen: divergence. All the algorithms (at least in this work) are mathematically designed to always reduce the residual each iteration, but that formulation relies on a correct adjoint operator. Thus, sometimes, when the algorithms in TIGRE have a solution very close to minimum residual solution, they may diverge. The code in the toolbox does generally check for divergence and stop, but one of the effect that can be observed is that some algorithm will always diverge in a residual that is larger than others. This means that some algorithm can, regardless of their computational times, reach to a better solution than others.

All test in this section are performed in the XCAT phantom[57], in a 128^3 voxel size and 256^2 detector. Different number of angles are used, always uniformly distributed along the full circle. Figure 5-1 shows cross sections of the phantom on its middle plane and figure 5-2 shows 3 projections of the phantom as simulated for the following tests.

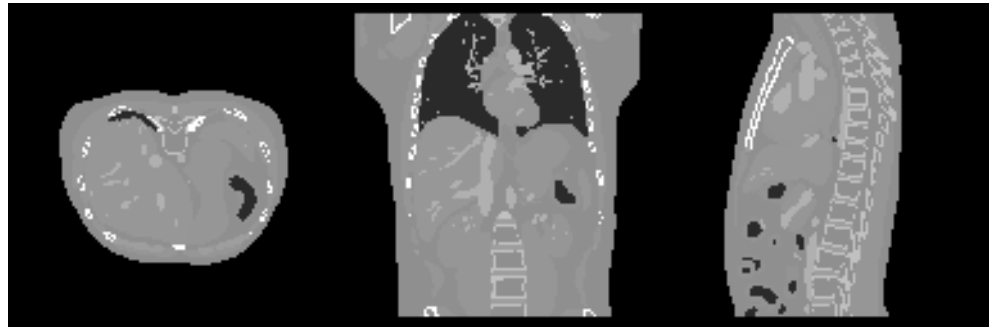


Figure 5-1: Cross section of the XCAT phantom in its middle plane in the three axis, for 128^3 voxels.



Figure 5-2: Simulate projections of the XCAT phantom in three different projection angles for a 256^2 detector.

Update ordering in SART. An analysis in the different ART-type algorithms is presented in this section first. One of the discussed parameters that has an effect in the convergence rate of the ART-type algorithms is the ordering of the used projections. Research has shown that in ART, the decrease of the residual with respect to how the rows are chosen for the updates is significantly changed[CITE], however in the algorithms feasible for big scale tomography, this effect is seen in a smaller scale. Figure 5-3 shows the convergence of SART during 150 iterations using 100 projections as data. The same configuration of SART is run using ordered, randomly ordered and angular distance maximizing ordering schemes for the update order. While minor, the figure shows how random ordering does generally increases the convergence rate of the algorithm, at no computational cost. This is the default value in the software. Note that in this test there is no reduction of the relaxation parameter λ .

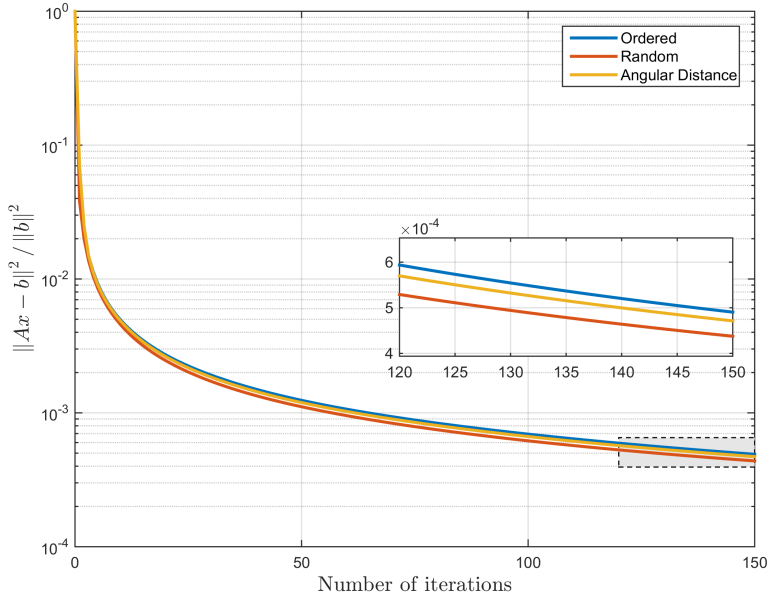


Figure 5-3: Normalized residual versus iteration of SART compared to different angle ordering schemes, using 100 projections and no relaxation parameter reduction

Comparison between SART, OS-SART and SIRT. These algorithms have very different convergence, as updating the image per-equation has the effect of converging faster. However, the computational times are greatly reduced by updating more rows at the same time. This effect can be seen in figure 5-4, on where the convergence versus iteration of these three algorithms is plotted. Note the convergence difference between SART and SIRT, where SIRT doesn't reach SART's residual even after 1000 iterations, however, each iteration of SIRT is two orders of magnitude faster than SART. OS-SART provides a middle ground alternative. Due to the specifics of the acceleration procedures for backprojection, OS-SART speeds are closer to SIRT than to SART (i.e. the speed does not change linearly with the image updates per iteration), however it is more prone to divergent behaviour in TIGRE. In the figure, OS-SART stops converging after 48 iterations. Of course, this behaviour is very data-specific, and there are multiple cases where it does not diverge. Figure XX shows the result images of these three algorithms after 150 iterations (48 for OS-SART). Note that the example being shown is low data, so even in the best case, the images are slightly noisy.

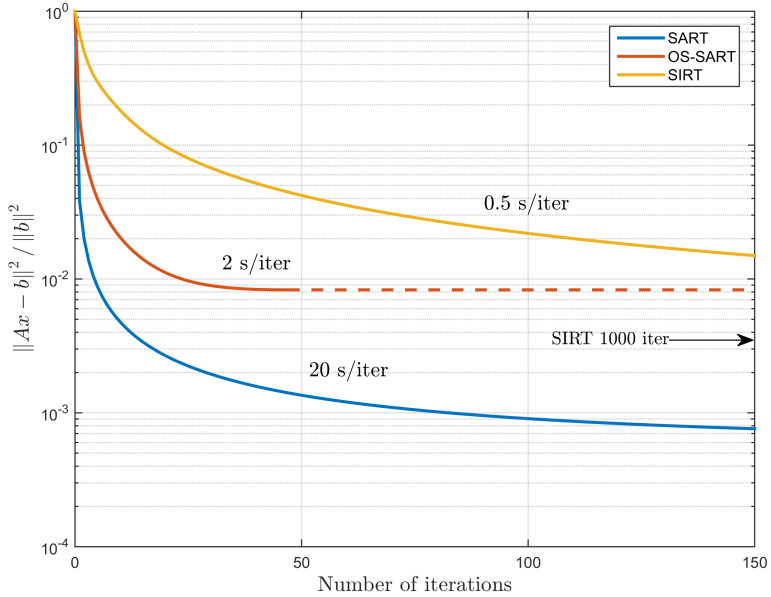


Figure 5-4: Normalized residual vs iteration number for SART, OS-SART and SIRT using 100 projections and no relaxation parameter reduction.

Relaxation parameter. The choice of a proper relaxation parameter does significantly change the speed on which a solution is found, and can avoid infinitely iterating through the same hyperplanes in case of an under determined or noisy solution. In TIGRE, two methods are present, as described in chapter 2: multiplying the relaxation parameter by a reduction factor after each iteration, and the Nesterov accelerated update, that does not technically update the relaxation parameter, but updates the image in each iteration using a iteration specific combination ration of the gradients of the current and previous iteration. It requires more memory, as it needs one extra image-sized variable to store the previous update, but the the algorithm finds a solution considerably faster, as it can be seen in figure 5-5. In the figure each of the SART, OS-SART and SIRT algorithms residual is plotted, and in each of them three versions are displayed, no relaxation parameter update, reduction with $r_{red} = 0.99$ and Nesterov update. In the plot it can also be seen that reducing the relaxation parameter by a ratio, while a good approach in SART-based hybrid algorithms, such as the TV minimizing ones in TIGRE, leads with slower residual reduction and ultimately with a worse image.

In figure 5-6, the solution found by the three algorithms using reduction of the relaxation parameter, using a Nesterov update and using static relaxation parameter of

$\lambda = 1$ can be seen side to side . The superior solution found by Nesterov is visually clear, and both SART and OS-SART reach a minimum in very few iterations. While SART does reach a better image (both in residual and error) without using Nesterov's update, the difference is minimal. It is important to note that using Nesterov's update, likely due to its fast convergence, leads to a faster divergent behaviour by the algorithms, thus the residual needs to be checked in each iteration leading to some computational overheat.

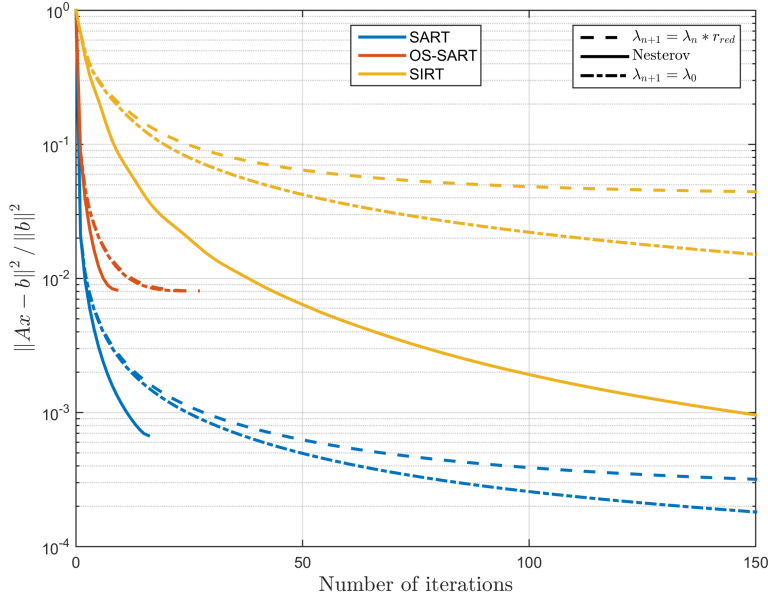


Figure 5-5: Normalized residual vs iteration number for SART, OS-SART and SIRT using 100 projections and different relaxation parameter reduction modes. If the relaxation parameter is reduced by a constant ratio the residual reduction worsens, and if reduced using Nesterovs update, it converges very fast.

5.1.2 Total variation minimization

There are 4 total variation minimizing algorithms in TIGRE, with 2 different minimization functional in total. As previously described, ASD-POCS, OS-ASD-POCS and b-ASD-POCS- β minimize the TV using a POCS minimization technique by minimizing the data constrain and TV norm independently using gradient descend. SART-TV however uses the ROF model for the TV-minimization step. The total variation algorithms are designed for applications on where the image is piecewise-smooth, as they will try to minimize the gradient on the image, by creating single valued patches in

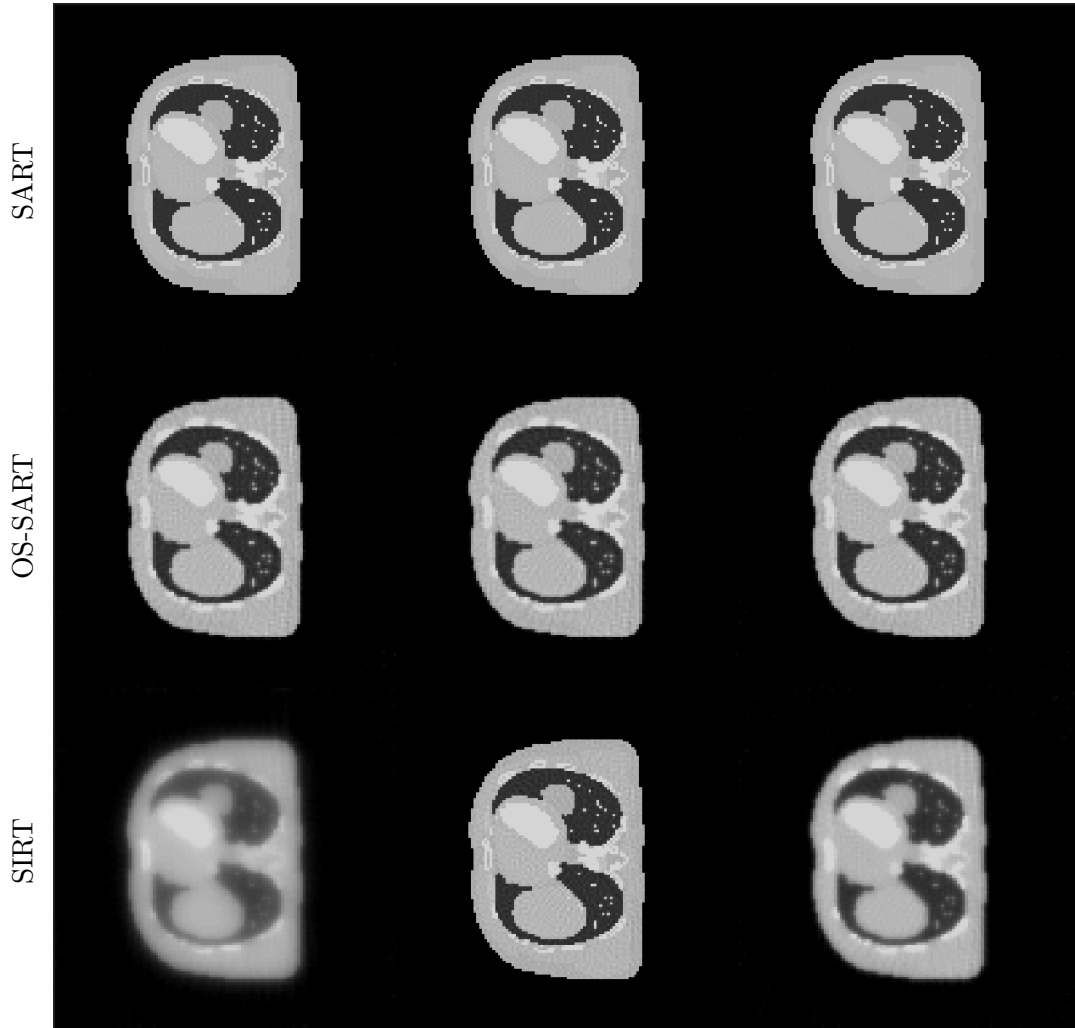


Figure 5-6: Reconstructed images with different relaxation parameter updates. OS-SART stops at iteration 24 in all but in the Nesterov case, where it stops in the iteration number 9. SART stops at iteration number 16 for Nesterov.

Table 5.1: NRMSE for the reconstructed images in figure 5-7

| | FDK | OS-SART | b-ASD-POCS- β | SART-TV | ASD-POCS | OS-ASD-POCS |
|-------|--------|---------|---------------------|---------|----------|-------------|
| NRMSE | 0.1373 | 0.0678 | 0.0338 | 0.0267 | 0.0304 | 0.0442 |

the image. In CT, the most noisy images are reconstructed when either the data is very noisy (generally due to small acquisition times and/or low energy X-rays) or when the data is limited, either from limited angle or more importantly limited amount of projections.

An example of the behaviour of the TV algorithms with the same dataset as in figures 5-1 and 5-2 is shown in figure 5-7. In this case, 30 uniformly sampled projections are used, perturbed with Poisson and Gaussian noise, to simulate photon scattering and electronic noise respectively. The figure shows FDK and OS-SART reconstructions, and the 4 mentioned TV algorithms. It is visually clear that the TV algorithms do provide a smoother reconstruction, and with less Normalized root mean squared error (NRMSE), as seen in table 5.1. The reconstruction by FDK is plagued with noise, and while the main structural features can be seen, most of the detail is lost. Even the bones themselves are practically indistinguishable from noise. OS-SART does reconstruct a smoother image, something predictable as it minimizes the 2-norm, and while one can see the more details in the image, it is still low. The rest 4 TV algorithms can be seen to flatten out the attenuation levels to similar values, thus reducing most of the noise. Additionally most of the features get clearly separated from the attenuation levels of the surrounding tissues and some of the algorithms (such as ASD-POCS) are able to reconstruct even single wide pixel structures correctly. It is important to note that while the parameters used to tune this specific TV reconstruction (available in the demo number 9 in the TIGRE toolbox), they are far from optimal and very sensitive[36]. When choosing the exact optimal parameters for the TV reconstruction algorithms, the result images tend to be significantly better than the ones shown here, but the parameter space is very data dependant and massive, thus to the author's knowledge, no parameter selection method has been proposed in the literature.

To illustrate the sensitivity to parameter selection, the algorithm SART-TV is run with 3 different values for number of TV-iterations per SART iteration for the same data set used in the previous test. The results can be seen in figure 5-8, where one can clearly see how a small changes can have a devastating effect in the output image. If a few more TV iterations are added to (b), the image gets a bit smoother and some detail is lost, as expected. However, if few iterations are removed from (b), the image can get completely destroyed. Note that these values are only applicable to this image

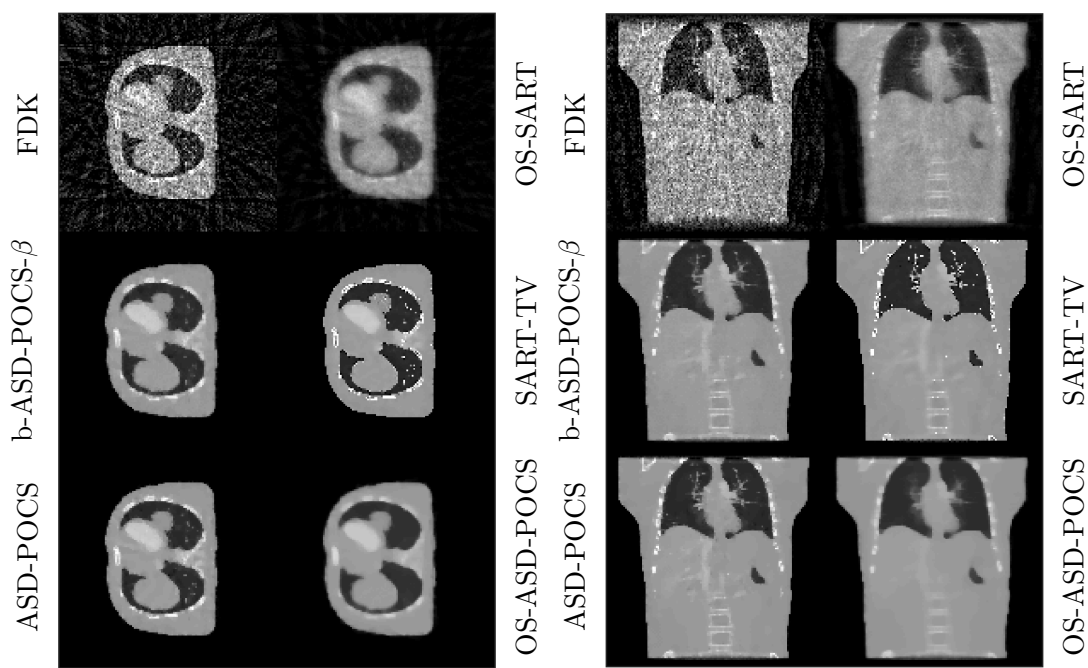


Figure 5-7: Reconstructed images using FDK, OS-SART and the TV algorithms b-ASD-POCS- β , SART-TV, ASD-POCS and OS-ASD-POCS with a limited amount and noisy data. Both figures show the same data and algorithms, but with a different cross-section of the image.

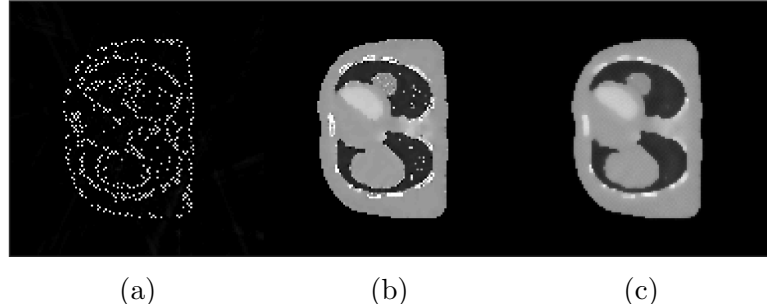


Figure 5-8: SART-TV algorithms with different amount of TV iterations per SART iteration, (a) 32 iterations, (b) 40 iterations, (c) 48 iterations.

with the exact amount of noise and projections. Different experiments may not show this behaviour or may be more intolerant to parameter change. This is arguably the biggest limitation for the common use of TV algorithms in real application. As an advantageous point, once the good parameters are found, generally the algorithm will perform similarly in similar images, thus application specific parameters may be an option.

5.2 Iterative Algorithms in Different CT Applications

This section tries to illustrate the effect of different algorithms within the TIGRE toolbox in a series of datasets.

5.2.1 Medical Head CBCT from The Christie Hospital

5.2.2 Cryo Soft X-Ray Tomography at Diamond Light Source

Cryo soft X-ray tomography (Cryo-SXT) is a relatively new[CITE] technology to image micrometer size biological samples in full 3D. Generally, cell-imaging is performed with electron microscopy (EM) machines and all its variants (transmission electron microscopy, scanning electron microscopy, cryo-electron microscopy, electron tomography, etcetera), however these techniques have very limited penetration (less than $1\mu\text{m}$) and thus often require slicing of the samples for volumetric imaging. Cryo-SXT uses the so called water window for X-ray energies around the 500eV energy range. Unlike in higher energies, where everything is invisible, water becomes transparent but carbon-based tissues are clearly visible on that range. Thus, while with lower resolution than most EM, Cryo-SXT allows for full volumetric visualization of the cells without damaging the samples. In order to be able to image in the extremely accurate setup in

both sample handling and X-ray parameters, these Cryo-SXT images are captured in synchrotron facilities. The data used in this work is from the B24 beam-line at the Diamond Light Source.

However, Cryo-SXT data has several sources of errors that make its reconstructed images significantly noisy. The typical penetration depth of soft X-rays is around $10\mu\text{m}$, while the samples are generally an order of magnitude bigger than that in height and width. Thus Cryo-SXT is a limited angle problem, where most of the datasets are sampled over a 120 degrees arc. In the extrema of this range, the images in the detector tend to have little or none information in some parts of the image due to photons not reaching the detector. Additionally, the low intensity and small sample size do mean that there the detector data is very noisy, as photons spread out more (in pixel dimension) and less photons reach the detector. The size of the sample also comes with errors in the mechanical systems of the imaging set up. When working in a scale of microns, any small vibration is visible and considerably offsets/perturbs the measured data. Generally this type of errors are removed by pre-processing using alignment techniques, but the algorithms involved are often not fault proof, and the data used in reconstruction ends up having some misalignment errors. Figure 5-9 shows two of the sinograms of the datasets, in where the noisy nature of the data can be visually appreciated. In the top figure, attenuation artefacts are visible. In the bottom figure one can see the darkening of the areas at high angles (upper and lower parts of the figure, at 25% of distance from the left) and areas that have been filled by the aligneation algorithm with a single value (mid-left edge and bottom right edge). These last errors do have no influence in FBP, as the high pass filtering of the data sets their values at zero, but are a source of artefacts in iterative algorithms. Both sinograms show a considerably high amount of random noise.

Few datasets have been reconstructed from this imaging modality using various algorithms and using various algorithms. Objective evaluation of the quality of the reconstructed image with each algorithm is not possible, as due to the noisy nature of the images, classifying some of the visual artefacts as data or noise is hard. Thus this section does not intend to claim that any of the algorithms perform better than the filtered backprojection (FBP), just highlight the differences.

The “2017_0207_Trypanosoma_33” dataset.

This dataset contains a section of an image containing few Trypanosoma, a unicellular parasitic protozoa that cause different illnesses, such as the sleeping sickness. In the images, the big circle within each of them, of similar attenuation level as the rest of the cells is the nucleus while the smaller circular features are organelles of the cell.

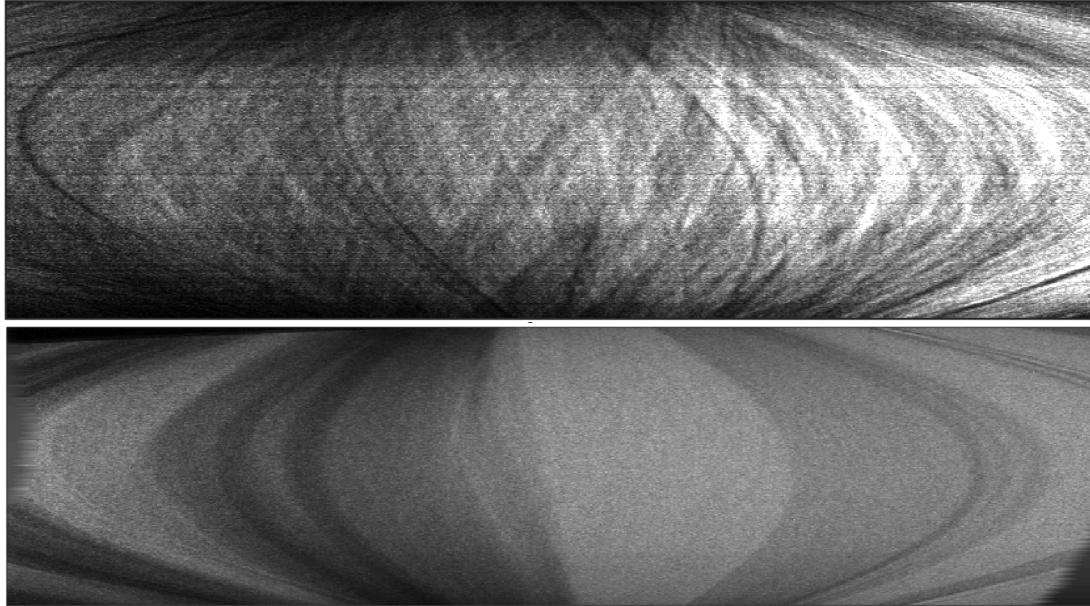


Figure 5-9: Sinograms of two different datasets of the data from a Cryo-SXT. The top figure shows attenuation artefacts over different individual measurements of the data and significant random noise over the whole sinogram. The bottom figure shows strong attenuation in high angles and artefacts generated by alignment.

Several algorithms have been used to test the effect of iterative algorithms. Initially SIRT and CGLS have been chosen. Both of these algorithms are expected to generate images with very few noise, but perhaps lose the most detailed information, or at least create smoother boundaries than FBP, as they minimize the L2 norm using all data in one go (per iteration). Result of these, compared to FBP can be seen in figure 5-10. SIRT generates a very smooth image without barely any noise, however the details are very smoothed also, specially the boundaries of the objects. However, very few iterations of SIRT have been performed in this dataset. More iterations will likely improve the quality of the result, but it is likely that hundreds of them are needed to obtain a good image. CGLS however seems to separate data from noise better, while also creating some smooth (not as much as SIRT) boundaries. However it is unclear to me how much of this is caused by misalignments on the data and how much by the algorithms themselves.

As shown before in this chapter, OS-SART can improve the convergence speed of SIRT sacrificing some computational time. SART can further this, however as these images are too big, the SART solution would take too long (around 7 hours for 50 iterations). Additionally, total variation minimization can be applied to remove the

noise that the images have. Figure 5-11 shows FBP, OS-SART, and ASD-POCS with 20 total variation iterations and using OS-SART instead of SART as data fidelity update (OS-ASD-POCS).

Note that the images have a darker vertical “band”, not as obvious in SIRT and CGLS. This is caused by some errors in the projections that with proper preprocessing step could be removed. OS-SART reconstruct a similar result than FBP, with slightly lower noise levels and extreme values. Less iteration of OS-SART would probably generate a less noisy image, however they will also likely show less contrast and features (similar as SIRT before). The total variation version of OS-SART generates a cleaner image, but it has a slight “watercolor” texture. The strength of the total variation can be controlled by the amount of iterations, increasing them enhances this effect. Figure 5-12 shows 0, 20 and 5 TV iterations. While the tuning of this value can not (yet) be done automatically, once the desired one is found it generally works for all similar images. The actual value of the reconstructed voxels is different in each algorithm. This can be explained by the nature of the data, as for example, half of the values are negative, which makes no sense physically. Thus, the visualization range has been tweaked to match histograms in the figures.

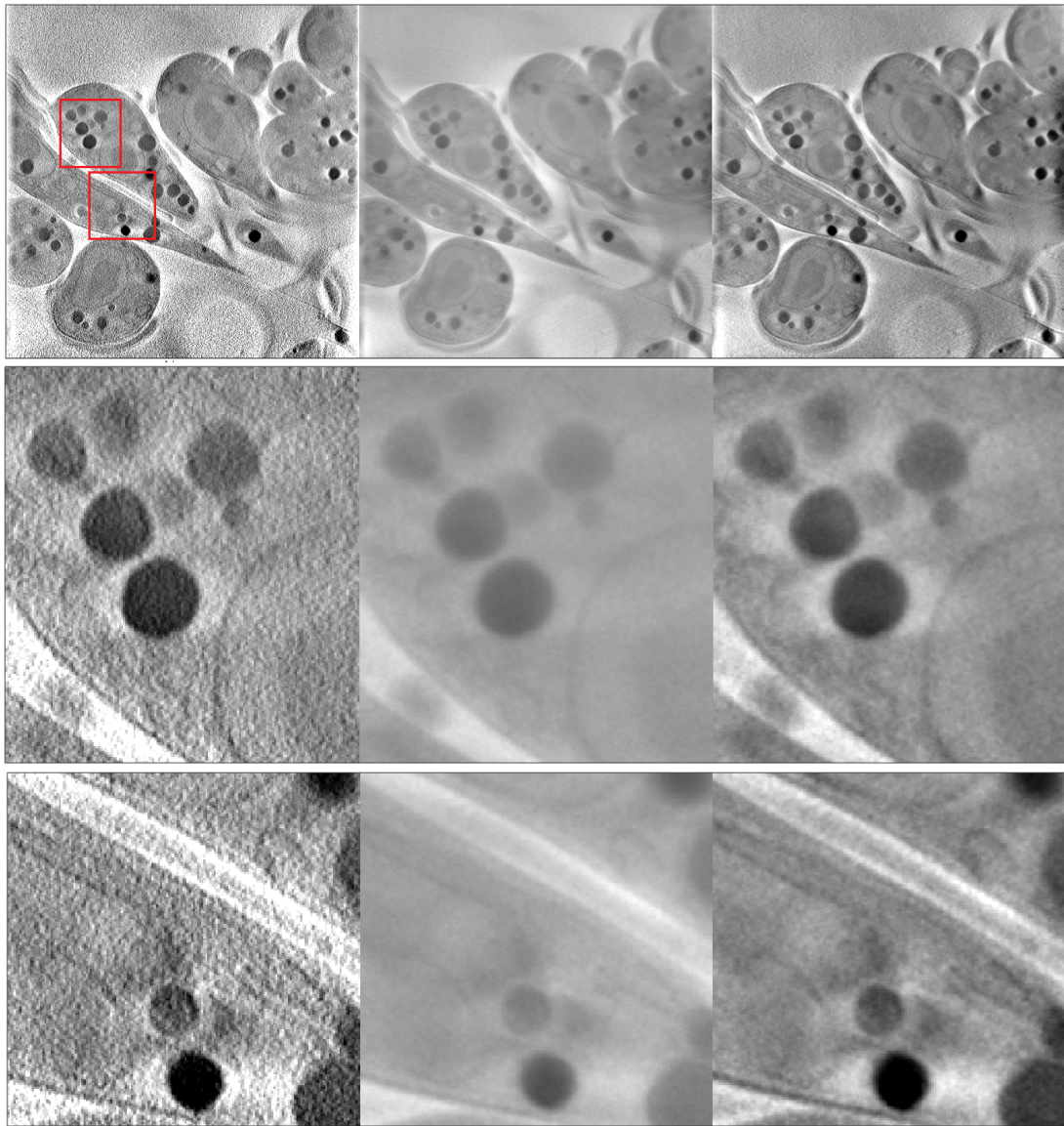


Figure 5-10: Columns: FBP, SIRT (20 iterations) and CGLS (7 iterations)

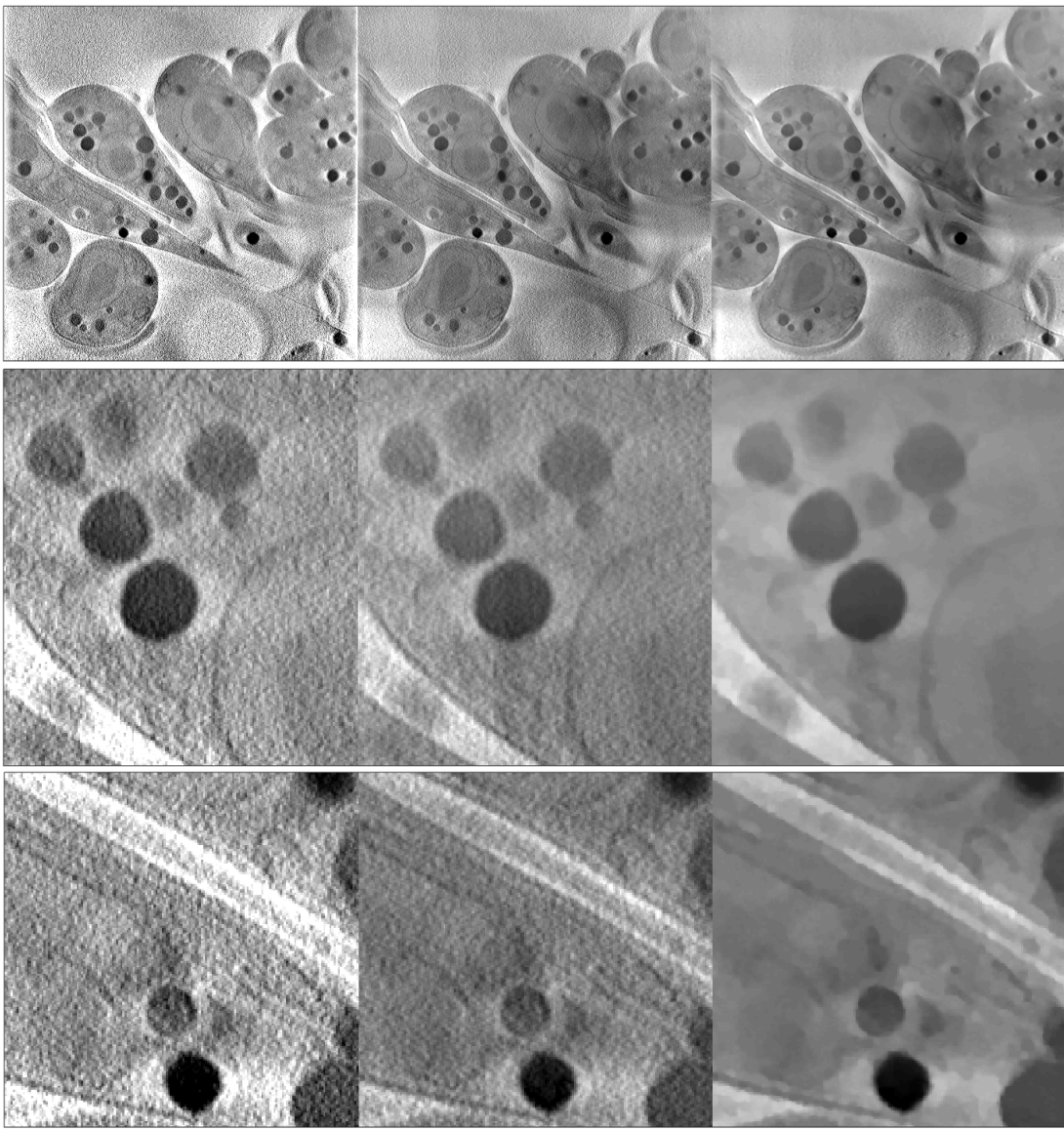


Figure 5-11: Columns: FBP, OS-SART (20 iterations) and OS-ASD-POCS (20 iterations, 20 TV iterations each)

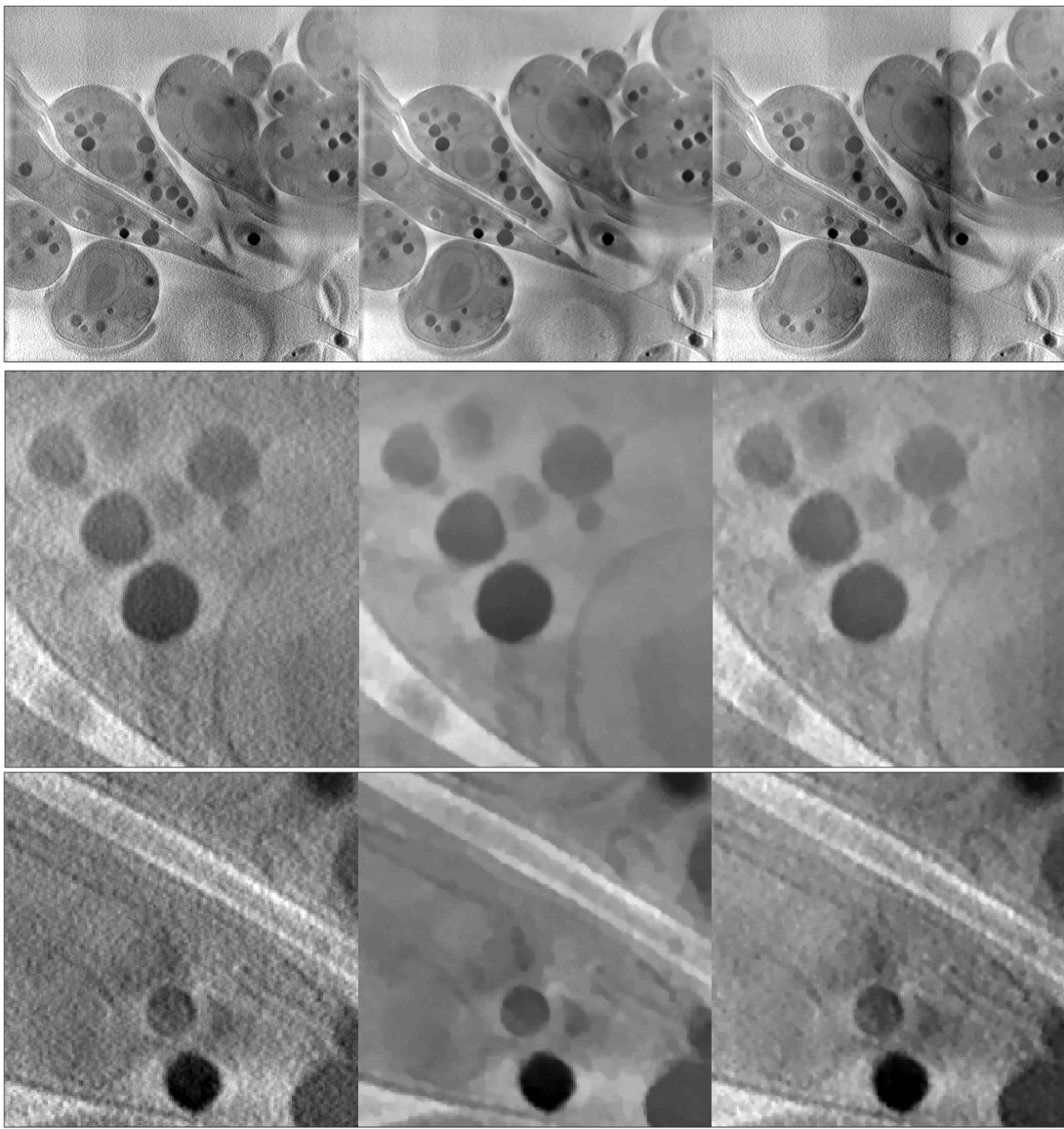


Figure 5-12: Columns: OS-SART (20 iterations, 0 TV iterations), OS-ASD-POCS (20 iterations, 20 TV iterations each), OS-ASD-POCS (20 iterations, 5 TV iterations each).

The “3_20160218_tomo_65t55_p5_area_2MB1_Export” dataset.

This dataset contains the zoomed area of a XXXXXXXXXXXXXXXX cell. The big smooth area in the top left side is the nucleus of the cell, while the rest are organelles on the cytoplasm of the cell. This dataset has is noisier than the previous one, and has a higher amount of small details on it. In figure 5-13 the reconstructed image can be seen, on where the columns show FBP, OS-SART, CGLS and OS-ASD-POCS algorithms, and the rows different zoomed areas of the image. In this dataset the iterative algorithms to have a strong influence in the removal of the noise. This is clearly apparent in the second row of the figure 5-13, on where the three iterative algorithms, specially the TV based one, remove significantly the noise of the organelles both in the left and right side of the image. in the left, a mostly smooth organelle is reconstructed with the iterative algorithms while FBP is very riddled with random-looking noise. In the right side of the image in this row, one can distinguish the black dots of inside the big circle in the iterative algorithms, where in FBP selecting these black dots as data rather than noise would be harder both to a trained human eye or a segmentation algorithm.

The “Grid1_Area2_Cell2_tomo3-All_60t60_p5d_6s_mb1_Export” dataset

This images also show a cell, with part nucleus and part organelles, as in the previous dataset. The same algorithms have been used, and the results can be seen in figure 5-14.

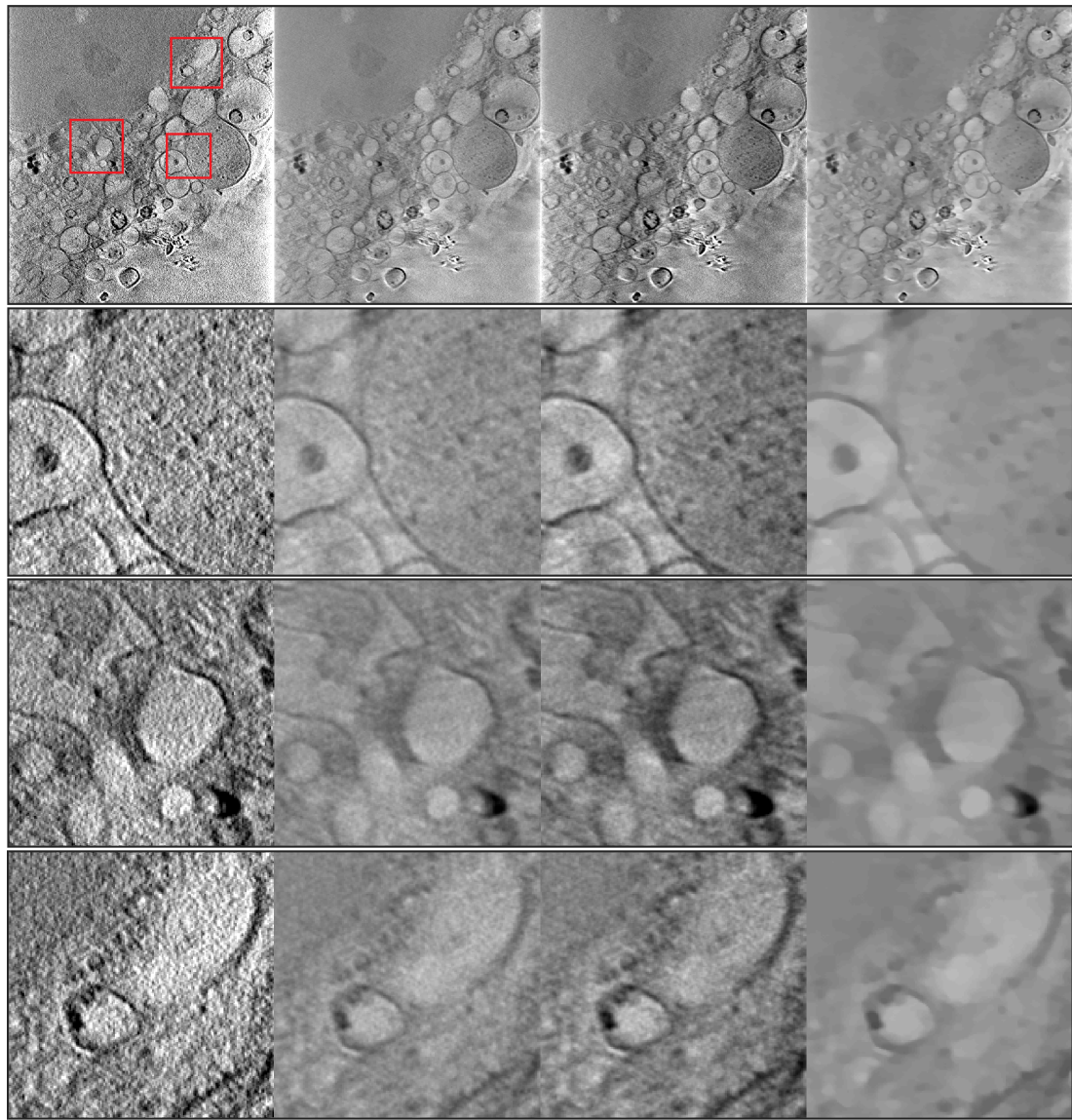


Figure 5-13: Columns: FBP, OS-SART (30 iterations), CGLS (7 iterations) and OS-ASD-POCS (30 iterations, 10 TV iterations each). The zoomed areas are highlighted in the FBP image.

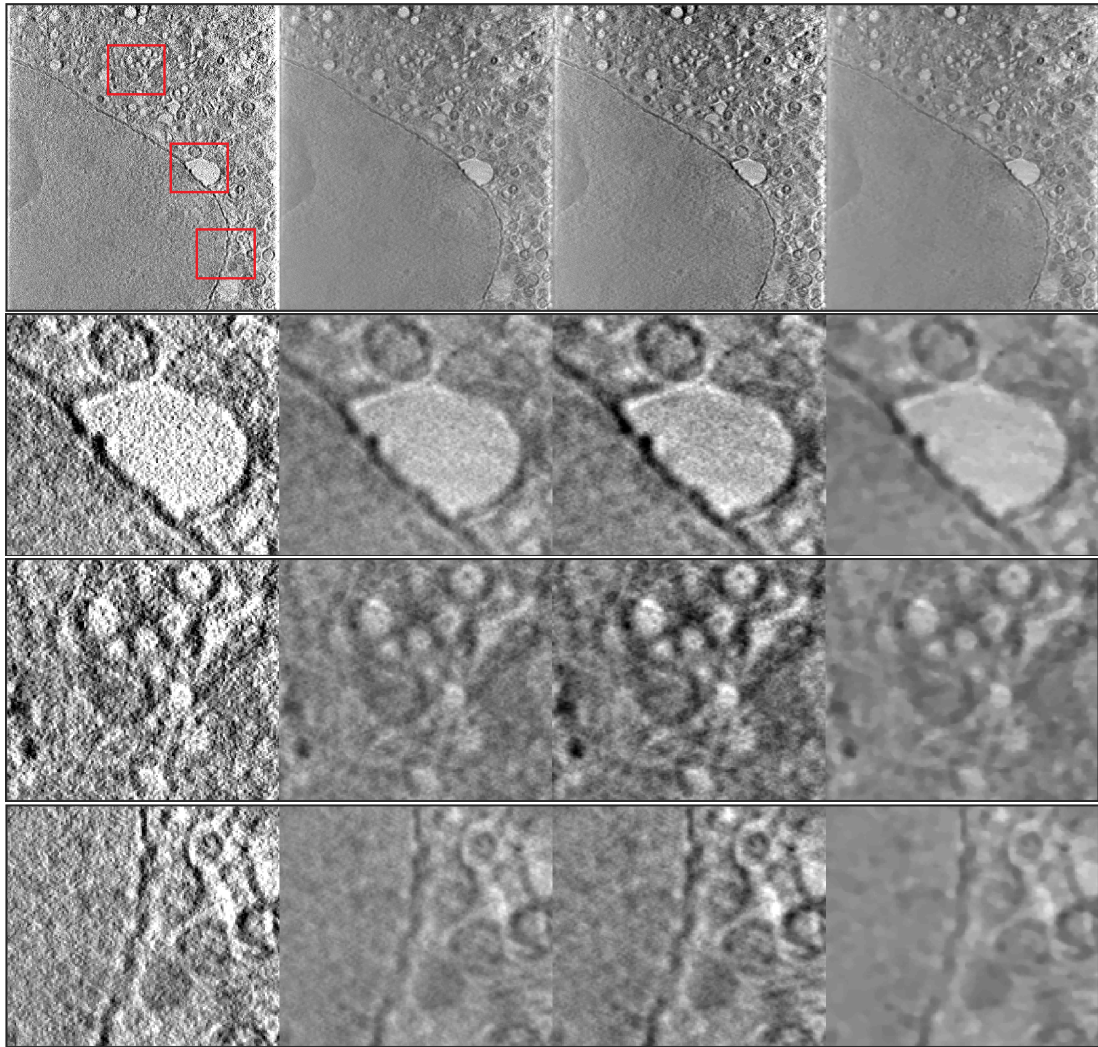


Figure 5-14: Columns: FBP, OS-SART (30 iterations), CGLS (7 iterations) and OS-ASD-POCS (30 iterations, 10 TV iterations each). The zoomed areas are highlighted in the FBP image.

Chapter 6

Motion compensation modelling

As broadly discussed in chapter 2, motion is a major source of error in tomographic imaging. The change in location of any image part, or human tissue in the medical field, will effectively be translated into blurring in the reconstruction step. This blurring imposes a big limitation on the possibility of treating cancer in lung and liver, as these are very mobile parts of the body. Having not only accurate spatial information, but also temporal information of these organs can potentially improve the treatment outcome. This means that good 4D imaging techniques can improve radiation therapy. Several methods have been proposed in the literature for compensating for motion in tomography, most of the relying on the binning of the data into multiple phases.

In this chapter a completely new approach is introduced and tested based on the ideas developed in the Proton Synchrotron (PS) at CERN for phase space tomography for non-linear motion to medicine. This new method can effectively remove any motion that happened during data acquisition while still using the information of the full dataset to reconstruct the image. This technique, relies in the approximate knowledge of the behaviour of the motion during the scan period and can reconstruct images in any chosen state of the motion.

The chapter introduces the ideas used in the tomography at the PS and explains how can they be transferred to X-ray absorption tomography, using the mathematics and computational techniques presented in previous chapters. First, a description of how to modify the standard GPU techniques and reconstruction algorithms to add the motion compensation is given. Then a series of proofs of principles are given, starting from a very basic motion model and ending using real patient data, using similar techniques than the ones available in a hospital. Finally, an in depth comment of the possibilities of the algorithms is given.

This chapter is widely based on the journal article “A general method for motion

compensation in X-ray tomography” [7].

6.1 Alternative motion modelling approach

Motion in tomography is a problem not only in X-ray modalities. Phase space tomography [2] is a hybrid algorithm that combines particle tracking in a computer model of a synchrotron with iterative ART to reconstruct an image of the population of a bunch of particles circulating in the accelerator. The particle motion involves non-linear rotation and is non-cyclic, but a 1D projection of the distribution can be completely acquired as a single snapshot on one turn of the machine. By tracking test particles to gain a knowledge of how the geometry of the 2D image plane (longitudinal phase space) deforms, the information in all the discrete time slices acquired over many turns can be translated back to the same instant and tomographically combined in a single image. Conceptually this means adding the motion information to the geometry of the model – in the A matrix – with which the problem is posed rather than inserting it somehow into the mathematics of the tomography by which a solution is found.

The concept can be transferred to standard absorption tomography, but the idea of following the motion of test points in a 3D image volume simply does not scale from the 2D tracking used for the modest number of pixels typical in phase space tomography. It would lead to unreasonable computing times and memory requirements. Instead, motion is modelled as a different effect with the same mathematical result. Thus a shift upwards of the voxels in a region of the image is modelled as a local shift downwards of the X-ray paths through a regular voxel mesh that remains frozen in the state at which the reconstruction is made. The motion can be arbitrary provided it does not send any voxels out of the image or add new ones to it.

The idea is illustrated in figure 6-1, where two different states of motion are sketched. In order to reconstruct at the initial time (a), the measurement at detector element d_k at later time (b) is back projected along the deformed line of response in (a) and so combined with the measurement at element d_j made directly at the earlier time. Likewise, if the later time is chosen for the reference state at which to reconstruct, the integral over the deformed line of response in (b) provides the attenuation figure needed to project onto d_j in order to iterate the measurement at that element which was actually made at time (a). Note that the paths are not only bent (or ”warped”) but also stretched in some places and compressed in others.

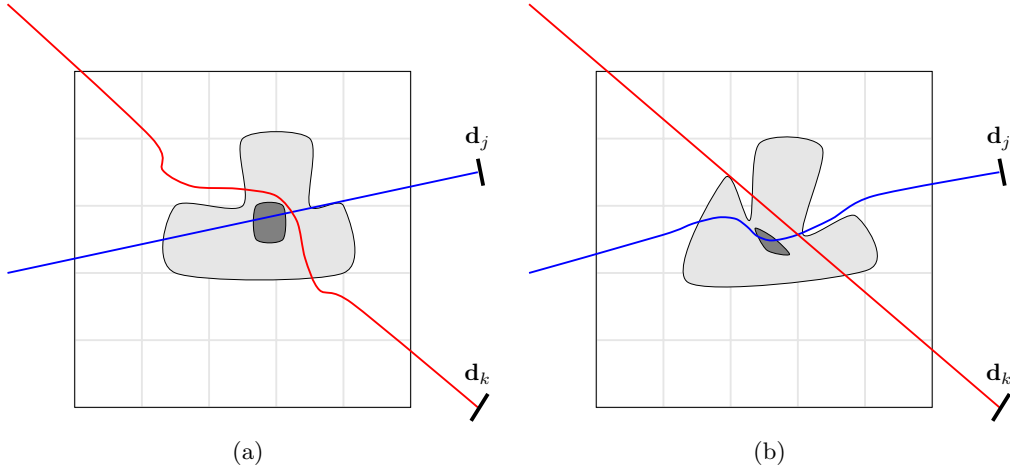


Figure 6-1: The integral over a path in image (a) yields the same result as the integral over the same coloured path in the deformed image (b).

6.1.1 Warped projection operator in a GPU

The warped X-ray paths cannot be easily translated into classic projection operators. Evaluating the length of a curvilinear path accurately inside every voxel it traverses would require a set of complex numerical methods which would inevitably increase the computation time significantly. Instead, the uniformly sampled projection method explained in chapter 4 is used, for which the ray-warping operation becomes a straightforward modification of the code. Rather than sampling at each image coordinate along a straight line, the vector field at that coordinate is first added and then the image is sampled.

The pseudocode in a GPU is outlined in algorithm 7. One thread per X-ray is launched to compute N_{ray} threads organized in $\text{divV} \times \text{divU}$ blocks. This means that instead of computing each of the path integrals in lexicographical order, small subsets of blocks (in the detector) are computed together. This decreases the memory latency and increases the overall speed of the kernels by up to 300% in our tests. For more information about GPU memory access and optimal X-ray indexing we refer the reader to the work by Chou *et al*[12]. As information about the texture cache is proprietary, empirical tests were made to find the best size for divV and divU . These showed 32×32 to be fastest on an NVIDIA Tesla 40k. Note that there are reportedly faster structures for GPU kernels[13], but our tests showed no such improvement so we have stuck to the simplest approach of one thread per ray.

Once an X-ray is selected, it is sampled over its path at every user-provided Δl step

Algorithm 7 Motion interpolated X-ray projection

```
1: Precompute geometric constants
Launch:  $N_{ray}$  threads organized in  $\text{divU} \times \text{divV}$  blocks
2: for X-ray path do
3:   Compute  $[x, y, z]$  sample position
4:   Sample  $[\text{DVF}_x, \text{DVF}_y, \text{DVF}_z] = \mathbf{DVF}(x, y, z)$ 
5:   Sum $+= \Delta l \cdot \text{Image}(x + \text{DVF}_x, y + \text{DVF}_y, z + \text{DVF}_z)$ 
6: end for
End Kernel
```

length. As previously mentioned, any real-valued coordinates, $p = [x, y, z]$, will yield a sample value using the interpolated read of texture memory. The point is first sampled over the relevant DVF, yielding the change in coordinates of that specific point, then the image is sampled at the new displaced coordinates, $q = p + \text{DVF}$. The DVFs needed are those that describe the deformation from all the shifted states back to the reference one of the reconstruction. Note that this description must be provided in the coordinate system of the reference state, so that $q - p$ is the extent of the inter-phase motion arriving at p rather than originating from it. This makes it more complicated than the forward mappings from the reference state to each of the others.

6.1.2 Warped back projection operator in a GPU

Warped back projection is simpler to compute as shown in the pseudocode outlined in algorithm 8. First, the standard back projection is computed using memory latency aware voxel ordering. Then, a second GPU kernel is launched with the same thread and block sizes and, for each voxel, a sample of the relevant shifted image is taken at $(x + \text{DVF}_x, y + \text{DVF}_y, z + \text{DVF}_z)$. This last step is basically a 3D interpolation. It is important to note that the DVFs used here are not the same as those for projection. And, although they are the inverse of each other, that inversion is not nearly as mathematically straightforward as a change of sign.

Several reportedly faster back projection operator structures exist in the literature. We found that the one by Zinsser *et al*[82] can lead to execution speeds up to four times faster, but only when multiple back projections are used at the same time in the kernel. Since the vector fields of the motion-compensated algorithm would generally be different for each back projection, this kernel structure will not accelerate the computation. However, as the drawbacks of using the more complex structure are negligible, it has nevertheless been implemented in our code. Thus, if a case is treated in which there is no motion to compensate, it will run more quickly.

Algorithm 8 Motion X-ray back projection

1: Precompute geometric constants

Launch: N_{voxel} threads organized in $\text{divX} \times \text{divY} \times \text{divZ}$ blocks

2: Compute $[u, v]$ detector position in line with a source-voxel direction

3: Sample $\text{Detector}(u, v)$

4: Compute corresponding weight w

5: $\text{WarpedImage} = w * \text{Detector}(u, v)$

Ensure:

Require: N_{voxel} threads, organized in $\text{divX} \times \text{divY} \times \text{divZ}$ blocks

6: Sample $[\text{DVF}_x, \text{DVF}_y, \text{DVF}_z] = \mathbf{DVF}(x, y, z)$

7: $\text{Image} = \text{WarpedImage}(x + \text{DVF}_x, y + \text{DVF}_y, z + \text{DVF}_z)$

End Kernel

6.1.3 Motion-compensated algorithm

Using any iterative CT reconstruction algorithm with warped projection and back projection is simple once the DVF_s are known. But first, a reference image is needed and the DVF_s from this reference state to the shifted states must be computed, together with the inverse DVF_s back to the reference. Once the DVF_s are known, the only modifications to a given algorithm are minor. Whenever the projection operator is used, the warped projection operator with the inverse DVF_s should be used instead. Likewise, for back projection, the warped version with the forward DVF_s should replace the standard code. This allows motion to be included in both operators inside any algorithm independently of the mathematics that invokes those operators.

6.2 Results

In order to validate the motion-compensation algorithm, two different tests were performed. The results are presented in this section. First, a proof of principle is established by subjecting a digital thorax phantom to a well-defined, if somewhat contrived deformation with time. In this case, the expected image at any instant is perfectly known, but despite this the inverse motion map must still be computed numerically and is necessarily only approximate. The motion moves all voxels within the image (but not the image boundaries) and the amplitude of the deformation is made substantially larger than any real movement in a breathing patient. A second test is performed using clinical 4D-CT images, where the motion is only approximately known. Nevertheless, even an approximate motion model can be exploited to significant beneficial effect.

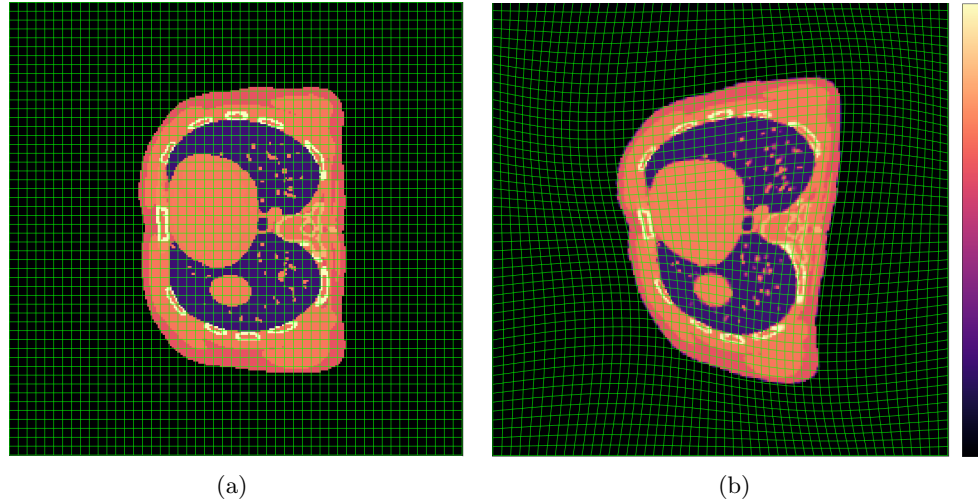


Figure 6-2: Transverse plane of the thorax phantom (a) without deformation and (b) at maximum deformation. A regular mesh overlay illustrates the motion map, although the actual voxels of the phantom are much smaller than this mesh size. The colour scale is linear attenuation coefficient in the range [0-0.045].

6.2.1 Arbitrary deformation of a digital phantom

The phantom used is a digital representation[1] of a human thorax comprising 256^3 cubic voxels. Motion is simulated according to equation 6.1 using 100 equidistant discrete steps of an arbitrary time scale t , which runs from 0 to 1, and using $L = 128$. This creates a steadily increasing sinusoidal deformation in all three spatial dimensions, displacing all voxels throughout the volume of the phantom. Only the boundaries at the faces of the cube and the three perpendicular mid-planes that intersect at its centre remain unshifted. Figure 6-2 shows a cross-section of the undeformed reference image at $t = 0$ and of the deformed image at $t = 1$. Not only are there no static regions, but the deformation is huge compared with real breathing[34], locally approaching three times that for a typical size of thorax.

$$\begin{aligned}
 V(x, y, z) = & (\\
 & 8 * t * \sin(x \cdot \pi/L) \sin(y \cdot \pi/L) \sin(z \cdot \pi/L), \\
 & 8 * t * \sin(x \cdot \pi/L) \sin(y \cdot \pi/L) \sin(z \cdot \pi/L), \\
 & 8 * t * \sin(x \cdot \pi/L) \sin(y \cdot \pi/L) \sin(z \cdot \pi/L)
 \end{aligned} \tag{6.1}$$

CBCT data are generated comprising 100 projections, one for each time step and covering a full circle. In order to benchmark the results, 100 CBCT projections are also

generated from the undeformed $t = 0$ data alone, providing a comparable dataset for reconstruction but from which motion is entirely absent. The images are reconstructed using 100 iterations of the SART algorithm.

Figure 6-3 shows cuts of three different CBCT reconstructions of the reference state. Motion is not included in the first and motion compensation is applied only in the last. The latter reconstruction is qualitatively almost identical to the static one despite the necessarily approximate inverse deformation map. However, the error in the inverse DVF, which is computed using a kernel splatting technique, is very small with more than 95% of the errors less than 0.05 voxels in absolute distance. This is typical of the numerical error that one can expect starting from a forward DVF that is well-known.

The error between the original phantom and each of the reconstructions is shown in figure 6-4. The image in the uncompensated dynamic case is highly saturated in various places, whereas the motion-compensated image has only slightly higher error overall than the static reconstruction. One would expect more iterations to reduce the error further. Cuts in the other planes are found to be qualitatively very similar.

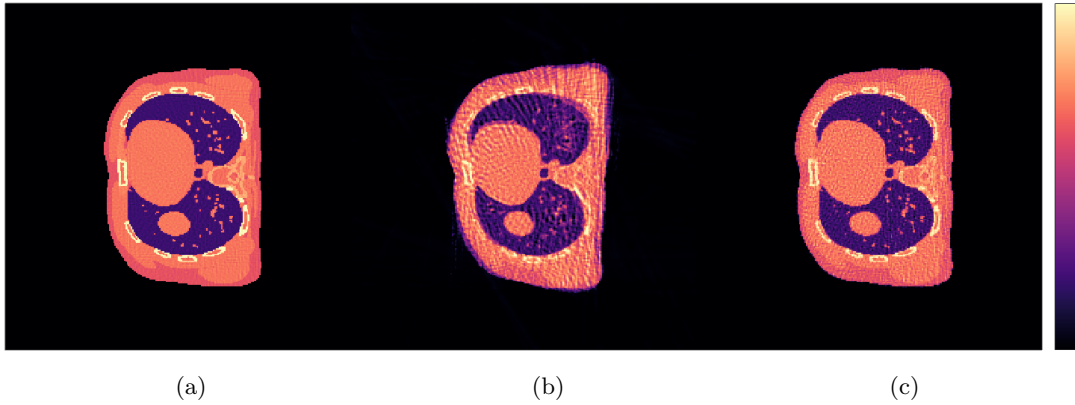


Figure 6-3: Transverse cross-section of the CBCT reconstruction made (a) using SART in the absence of motion; (b) with motion using uncompensated SART; (c) with motion using compensated SART. The colour scale is linear attenuation coefficient in the range [0-0.045].

Tellingly, the difference between the static reconstruction and the motion compensated one, as shown in figure 6-5, is quasi-uniform with no large differences at the boundaries between tissue types. This means that, while the error may be larger in the motion-compensated case, it will not prevent the correct delineation of an organ or a tumour.

This test demonstrates that the new method can handle arbitrary, non-cyclic motion and that it works well even when the inverse deformation map is not perfectly known.

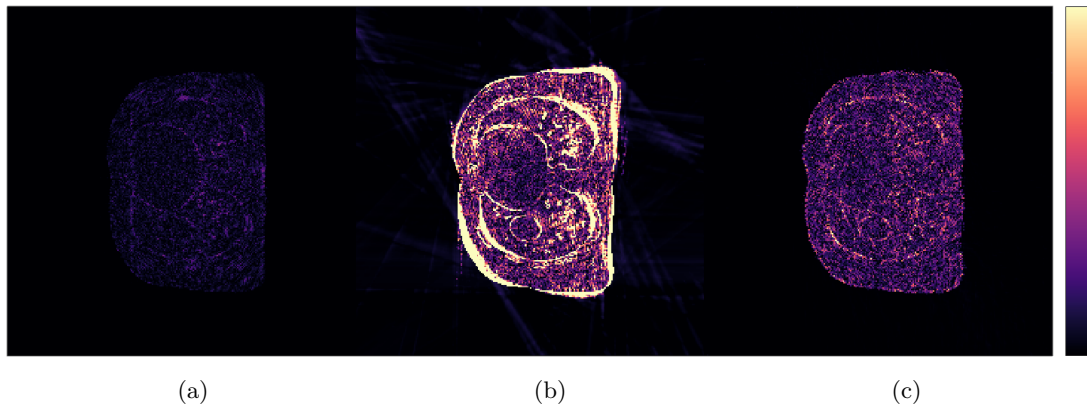


Figure 6-4: Transverse cross-section of the difference between the known phantom (figure 6-2(a)) and the CBCT reconstruction made (a) using SART in the absence of motion; (b) with motion using uncompensated SART; (c) with motion using compensated SART. The display range is significantly enhanced with respect to that of figure 6-3. The colour scale is linear attenuation coefficient in the range [0-0.01].

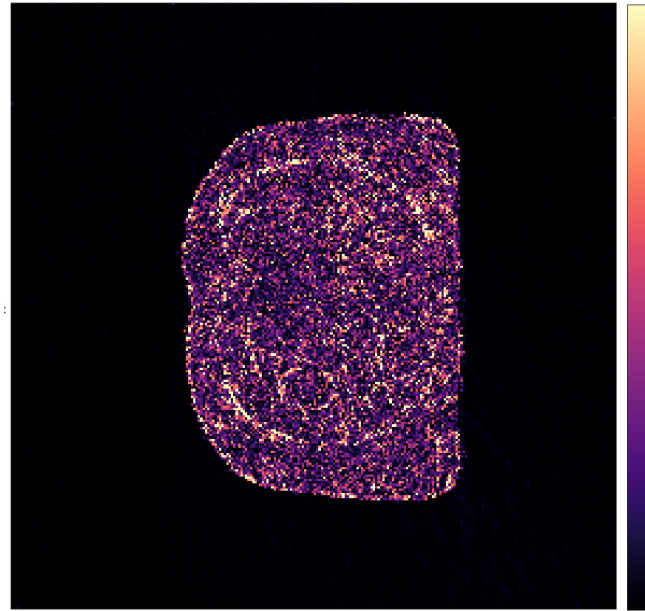


Figure 6-5: Transverse cross-section of the difference between the static reconstruction of figure 6-4(a) and the motion-compensated one of figure 6-4(c). The colour scale is linear attenuation coefficient in the range [0-0.005].

6.2.2 Real patient data

The second test is performed using clinical data with precomputed DVF_s, which are not entirely accurate. It is important to note that no real CBCT data are used, only 4D-CT image data. These are taken from the so-called POPI-model[70] and are publicly available[3]. The data comprise ten 3D-CT images (labelled from “0” to “9”) of the thorax equally spaced during the breathing cycle of a single patient. Additionally, motion maps generated by two different methods are provided by the authors describing the inter-phase motion of the voxels. We choose to use the maps that are generated by the parametric method for no specific reason as, statistically, both methods are reported to have similar errors. And we choose to use the 3D-CT image labelled “1” as the reference state to be reconstructed because the authors provide the motion vectors from this state to all the others. The reference state of the thorax can be seen in figure 6-6. The particular feature of a tumour is highlighted.

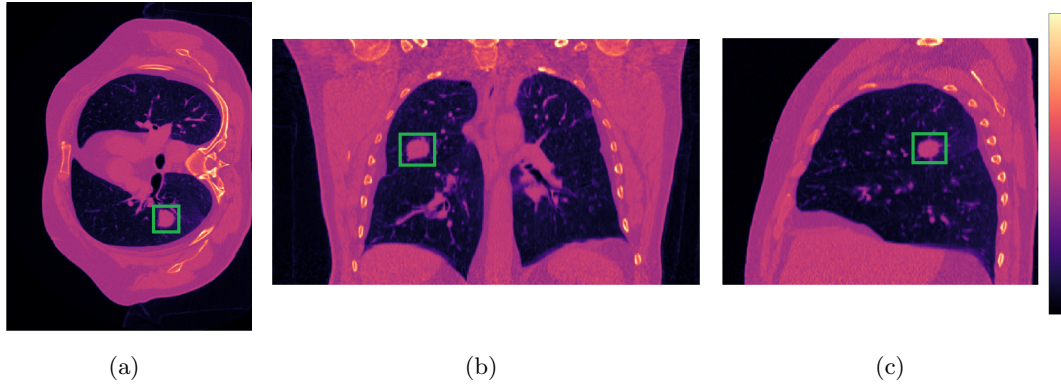


Figure 6-6: 3D-CT scan of a lung radiation therapy patient at breathing phase “1” cut to show the tumour (located inside the green rectangle) in the (a) transverse, (b) coronal and (c) sagittal planes. The colour scale is linear attenuation coefficient in the range [0-2000].

In order to simulate CBCT data, projections are generated from the phase-binned 3D-CT images. No extra noise is added as the images themselves are already noisy. One hundred equally spaced projections covering a full circle are generated for each of the ten states and from these a subset is chosen, 10 from each breathing phase, to give 100 projections each 3.6 degrees apart and spanning a complete breathing cycle. Note that the DVF_s are not used to approximate continuous movement as this would compromise the independence of the test that the quality of any subsequent motion-compensated reconstruction employing those DVF_s affords. In order to benchmark the

results, 100 CBCT projections are simulated from the state “1” data alone, providing a comparable dataset for reconstruction but from which motion is essentially absent.

There are four significant error sources inherent in the original 4D-CT data before a CBCT reconstruction is even attempted. There is that due to phase binning, which is particularly significant in the regions that move the most. This is visible in figure 6-6, for example in the lower boundary of the lungs. Another error source lies at the top and bottom (in the cranial-caudal direction) of the 3D-CT images. Due to the original data acquisition and reconstruction techniques, the images have increased noise-like errors in their extrema and, because of the randomness of these errors, the images are not entirely consistent with each other in these regions. The third main error in the source data is the inaccuracy of the DVFs in some areas. Finally, the inverse of the DVFs will have additional errors due to the numerical method used to invert them.

Given these numerous sources of error, one can expect streak artifacts in addition to the usual random noise exhibited in any reconstruction. As previously mentioned, it is a strength of the new motion-compensation method that it can be applied to any iterative algorithm, so one can be employed that reduces such artifacts by, for example, minimizing the total variation (TV). We elect to use both the well-known SART and the TV algorithm ASD-POCS[61] in this test.

Figure 6-7 shows cuts of four different CBCT reconstructions of the reference state. Motion is included in all except the first, but motion compensation is applied in only the last two. The SART algorithm is used in all cases except the last, which is processed with ASD-POCS. The second, uncompensated image has lost much of the detail inside the lungs, while the compensated algorithms, even with all the errors in the DVFs and data, reconstruct the tissue boundaries inside the thorax with higher accuracy. The last, TV case is particularly good. This is even more evident in figure 6-8, where the difference between the original 3D-CT image and each reconstruction is shown. One can see that the error is smaller overall in the motion-compensated cases, for which the discrepancy where the tumour is located is barely visible. Cuts in the coronal plane, which is the one containing the largest movement of the lungs, underscore the remarkable improvement in the motion-compensated images (see figures 6-9 and 6-10).

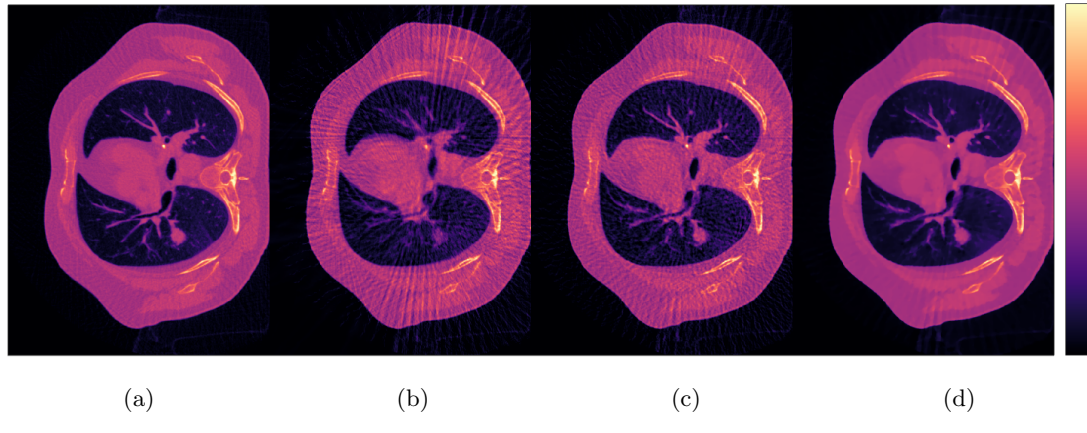


Figure 6-7: Transverse cross-section of the CBCT reconstruction made (a) using SART in the absence of motion; (b) with motion using uncompensated SART; (c) with motion using compensated SART; (d) with motion using compensated ASD-POCS. The colour scale is linear attenuation coefficient in the range [0-2000].

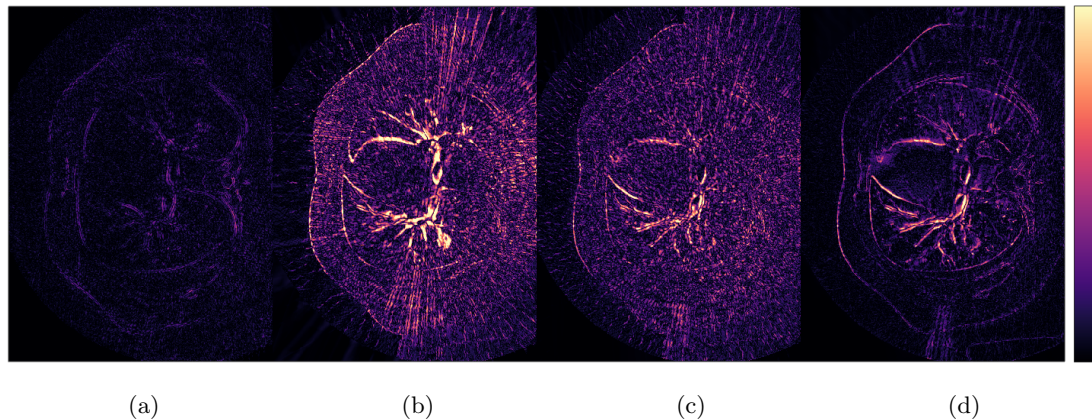


Figure 6-8: Transverse cross-section of the difference between the original 3D-CT image (figure 6-6(a)) and the CBCT reconstruction made (a) using SART in the absence of motion; (b) with motion using uncompensated SART; (c) with motion using compensated SART; (d) with motion using compensated ASD-POCS. The colour scale is linear attenuation coefficient in the range [0-400].

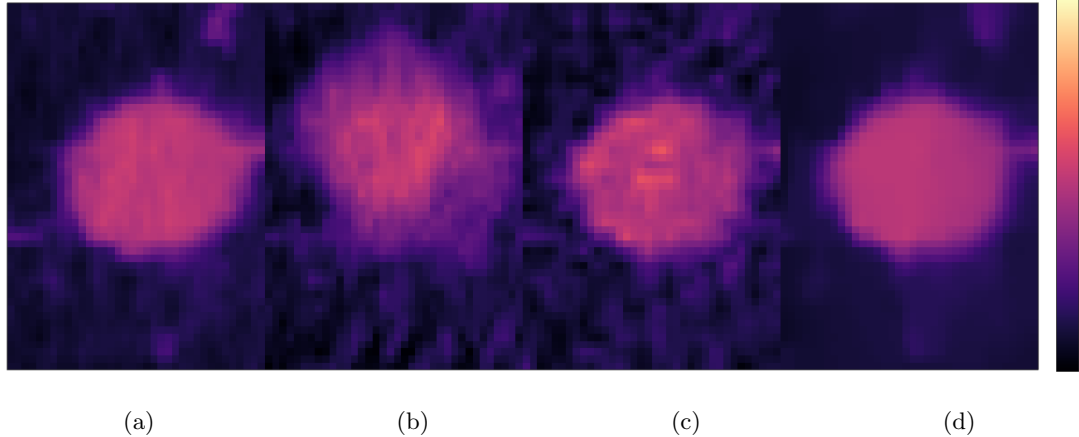


Figure 6-9: Zoom on the region where the tumour is located in a coronal cross-section of the CBCT reconstruction made (a) using SART in the absence of motion; (b) with motion using uncompensated SART; (c) with motion using compensated SART; (d) with motion using compensated ASD-POCS. The colour scale is linear attenuation coefficient in the range [0-2000].

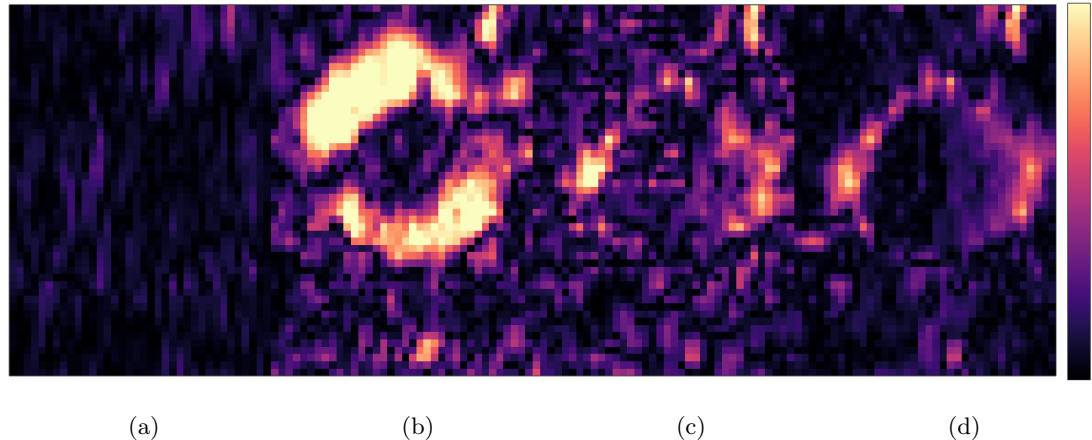


Figure 6-10: Zoom on the region where the tumour is located in a coronal cross-section of the difference between the original 3D-CT image (figure 6-6) and the CBCT reconstruction made (a) using SART in the absence of motion; (b) with motion using uncompensated SART; (c) with motion using compensated SART; (d) with motion using compensated ASD-POCS. The colour scale is linear attenuation coefficient in the range [0-400].

For a more quantitative assessment, the resultant images are cropped around the tumour taking a $36 \times 36 \times 26$ subset of voxels in the anterior-posterior, lateral and cranial-caudal directions (as indicated by the green rectangles in figure 6-6). Then, in order

to evaluate the quality of the reconstruction inside this box, three different indices are used to compare the original 3D-CT image with the four CBCT reconstructions of this test.

- Root Mean Square Error (RMSE) is defined

$$\text{RMSE} = \sqrt{\frac{\sum_{n=1}^N (\hat{p}_n - p_n)^2}{N}}, \quad (6.2)$$

where \hat{p}_n is a voxel in the original image, p_n a voxel in the reconstructed one and N is the number of voxels. A larger value means more difference.

- Universal Quality Image (UQI)[72] is a widely used index and is defined

$$\text{UQI} = \frac{2\text{cov}(\hat{\mu}, \mu)}{\hat{\sigma}^2 + \sigma^2} \cdot \frac{2\hat{\mu}\mu}{\hat{\mu}^2 + \mu^2}, \quad (6.3)$$

where cov is the covariance function and $\hat{\mu}, \mu$ are the means and $\hat{\sigma}^2, \sigma^2$ the variances of the original and reconstructed images, respectively. UQI yields a value between 0 and 1, increasing with increasing similarity.

- Segmentation mismatch. A segmentation value using Otsu's method[43] is computed for the original image and all voxels in the reconstructed image are identified as lying inside or outside the tumour according to that value. Then the number of voxels that are mislabelled by that segmentation is counted. A larger value means more difference.

The results for each index applied to the subset of voxels in the region of the tumour is shown in table 6.1. As expected, the SART reconstruction even in the absence of motion in the data does not reproduce the original image with any great accuracy as the data are still not perfect and CBCT reconstruction has its limitations. Nevertheless, it is a sufficiently good reconstruction to take as a benchmark for the others. Indeed, it should be stressed that, although the CBCT data here are artificial, in a practical scenario the equivalent static dataset would require a full order of magnitude more radiation dose to acquire than the dynamic one because of phase binning. In comparison with this static CBCT case, uncompensated SART applied to the dynamic data has considerably worse reconstruction quality, missing almost 10% of the tumour by segmentation. Motion-compensated SART performs significantly better, getting closer to the static SART values. Finally, the motion-compensated ASD-POCS results are very similar to those of the reconstruction without any motion. One would expect more advanced TV algorithms to perform even better.

Table 6.1: Tumour reconstruction quality by different algorithms

| | RMSE | UQI | Seg. mismatch |
|-----------------------------|--------|--------|---------------|
| SART without motion | 67.18 | 0.9656 | 1108 (3.288%) |
| SART with motion | 172.12 | 0.7617 | 3315 (9.838%) |
| SART motion-compensated | 109.84 | 0.9077 | 1505 (4.466%) |
| ASD-POCS motion-compensated | 82.72 | 0.9451 | 1284 (3.811%) |

This test demonstrates that the new method can be used in a clinical context even if the motion due to breathing is only approximately known.

6.2.3 Computation times

An important factor for clinical feasibility is the computation time that motion compensation adds to a standard reconstruction. The kernel times have been measured on a TESLA k40 GPU and are reported for the projection and back projection operations both with and without motion compensation. Two variants of the back projection operation have been tested, the single- and the dual-kernel versions as described in algorithm 8. Table 6.2 lists computation times for $512 \times 512 \times 141$ image and DVF sizes and a 512^2 detector size. The reported times are the average of 100 calls and only account for kernel time. As the back projection kernels are optimized for multiple calls, the average computation times for a single update or a multiple update are different. Both these times are shown in the back projection columns of Table 6.2. Reducing the size of the DVFs hardly changes the computation time as the number of samples needed is determined by the image size alone.

Both the single- and dual-kernel back projection operations lead to similar reconstructed image quality, with a visually imperceptible improvement in the dual-kernel case (0.1 in RMSE). The dual-kernel approach is expected to be better as errors in the DVFs are amplified by the divergent cone angle in the single-kernal case.

Table 6.2: GPU kernel times per projection.

| | Projection | Single-kernel Backprojection | Dual-kernel Backprojection |
|---------------|------------|------------------------------|----------------------------|
| Standard | 6.5ms | 4ms/2.5ms | - |
| Motion warped | 120ms | 24ms/18ms | 13ms/3ms |

6.3 Discussion

We have demonstrated a significant improvement in CBCT image quality by removing motion artifacts using a modelling approach to motion compensation. The resultant images still have some error compared with a static reconstruction, but critically, tissue boundaries are resolved with much greater accuracy than when motion is ignored.

One of the greatest strengths of the new method is that it employs all the projection data to reconstruct an image, reducing the X-ray dose to the patient. It is also completely algorithm independent; its novelty lies in a modelling approach, which in principle can be applied in conjunction with any static reconstruction algorithm. In fact, most of the motion-compensation ideas present in the literature and reviewed at the beginning of this work could incorporate the method. As some of these rely on refining DVF_s, then, instead of using those DVF_s to generate a deformed image from a prior high-quality one, they could be used to reconstruct images from the real acquired data. Others rely on temporal reconstruction constraints, where the images at successive time steps are regularized to look similar to their neighbours. Again, such techniques can be used in combination with the new motion compensation because the latter permits any state of the motion to be reconstructed. Indeed, one could generate an X-ray video of the patient breathing if enough time steps are reconstructed and, as these frames are computationally independent, they could be processed in parallel. And none of these extra images would require any extra dose for the patient.

The use of DVF_s can lead to large memory requirements and an increased pre-processing time, but it has been established in phase space tomography that it is possible to trade off the accuracy of the maps against an increased number of iterations and that some parameters in the motion model itself can be refined by their influence on convergence[22][21]. More speculative is the idea of "bootstrapping" the DVF_s without starting from any high-resolution images. One can imagine repeatedly subdividing the CBCT data into more and more motion phases, and thus iterating both the images and the DVF_s themselves at each subdivision, whilst still using all the data for each reconstruction by interpolating between DVF_s until there are enough of these to describe the motion in sufficient detail. This would be very heavy computationally and there is no guarantee of convergence.

As presented here, the method takes only 2 to 3 times longer than a standard iterative reconstruction algorithm due to the use of GPUs for the motion-compensated projection and back projection operators. So the computational penalty is not large. It is important to note that we used DVF_s of the same size as the images (they are

generally smaller) and the code was not highly optimized. Careful tuning should lead to appreciably faster execution.

One drawback of the method in an eventual clinical scenario is the need for a sufficiently accurate DVF for each of the projections. Obtaining realistic patient-specific DVFs is non-trivial. However, statistical analysis[63][8] has shown that, while inter-patient motion variability is high, intra-patient variability is low provided the patient performs free breathing. And preliminary tests of DVF error tolerance of the motion compensation method suggest that the algorithm is very robust to undersampled and noisy DVFs due to its iterative nature, but further study is required. Additionally, a method that maximizes the quality of the DVFs needs to be identified. Obtaining the breathing amplitude using the Amsterdam Shroud[78] and correlating that with prior DVFs or with DVFs obtained using binned, low-resolution 4D-CBCT images from the same dataset are promising techniques.

We consider that this motion compensation method could have a genuine impact in IGRT even though it is not yet at a clinical stage. Better diagnostic imaging offers the prospect of less collateral damage to healthy tissue and increased survival rates. Ultimately, it might be possible to steer a particle therapy beam in real time to follow a moving target.

Chapter 7

Numerical Study of Motion Compensation

In the previous chapter of this thesis a motion compensation algorithm is proposed as a general algorithm, and then is specifically focused for IGRT. The method however is scarcely compared with standard IGRT 4D CBCT image reconstruction methods, and some questions about the reliability of the motion models arise. Obtaining accurate motion description of the patients is still one of the biggest challenges in 4D imaging, regardless of the method used. How accurate do these models need to be? Additionally, if the motion is previously known to high accuracy, is 4D imaging necessary at all?

This chapter looks more specifically at these challenges and compares the motion compensated reconstruction to the now most commonly used methods in clinical IGRT. The aim of the work here is to supplement Chapter 6 with further observations about the behaviour of the algorithm under less ideal numerical data.

The objectives of this chapter are twofold: Firstly, the improved image quality obtainable by iterative algorithms is highlighted, showing how 4D CBCT binning methods can be improved by using better reconstruction algorithms, even with low data. Secondly, the flexibility and error behaviour of the algorithm is studied. The algorithm will reconstruct the image without any motion artefacts if the motion is perfectly known, however respiratory motion is variable between patients and within the patients themselves. The error behaviour with uncertainties in the DVF is crucial for the future possibility of the method in clinical cases, as while the motion correction method removes almost in its entirety any motion artefacts with very accurately known DVFs, obtaining very accurate motion models of patients is not possible. Thus, the performance of the method with low resolution and approximately accurate DVFs is studied in this work. Additionally, some proposed methods for 4D CBCT rely in computing

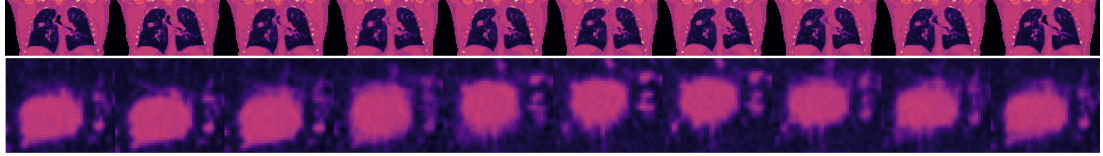


Figure 7-1: The POPI dataset for all frames in the cranial-caudal direction, and a zoomed area of the tumour. The colour scale is linear attenuation coefficient in the range [0-2000].

DVFs and then deforming a high resolution image with them. This work also studies why using reconstruction for motion correction produces better results than deforming a static image.

7.1 Materials and methods

An small introduction of the POPI dataset, reconstruction methods, methods for deformation vector field computation an reconstructed image quality evaluation parameters are described in this section.

4D POPI model

The dataset that is going to be used is the same as in the previous chapter, a 4D-CT (10 bins) treatment planning scan of a lung cancer patient, known as the POPI model. In Figure 7-1 a snapshot of the whole breathing pattern can be seen in the cranial-caudal direction, with a zoomed section of the tumour, on where the motion is better appreciated. Figure 7-2 shows the only frames 0, 3 and 6, for an amplified image.

Image reconstruction

This chapter reconstruct 4D images in all frames, and compare them to the ground truth. The iterative algorithms used in this section are SART and ASD-POCS. The rationale is that to demonstrate the flexibility of the method, more than one algorithm is presented, and SART is chosen because its a well understood and common algorithm, while ASD-POCS is chosen because its a more advanced algorithm with more complex constrains, however it is also quite well known one. One would expect that more advanced and newer algorithms to work even better than these two, but using those may obscure the results of the analysis that this chapter attempt to study, the quality of the reconstruction with the common errors in 4D CBCT.

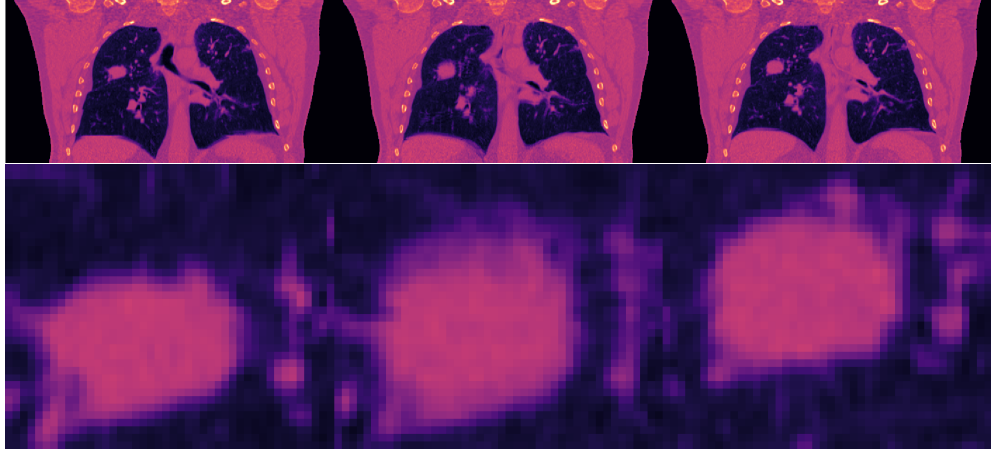


Figure 7-2: The POPI dataset for three frames (0,3 and 6) in the cranial-caudal direction, and a zoomed area of the tumour. The colour scale is linear attenuation coefficient in the range [0-2000].

Deformation vector field computation

As images in all frames are reconstructed in this chapter, deformation fields from and to any arbitrary time snapshot are required by the algorithm. For 10 frames, this makes 90 deformation vector fields + 10 identity fields (all zeroes). The DVFs used in the previous chapter that are provided with the POPI model only register to a single time slice (the second one, labelled 1), thus they are not enough to reconstruct the data in this chapter. In order to obtain the needed DVFs, a third party software has been used, the Elastix[30] package. Elastix is an open source software that provides a big variety of multimodal nonrigid image registration tools.

From the algorithms available in the package, a nD+t B-spline group-wise cyclic registration[39] approach has been chosen. This method is an optimization based algorithm, that registers 4D images (in this case) with B-splines. This allows for an analytic representation of the deformation using a simple yet fast method. The algorithms assumes deformation only in the spacial domain, and smoothness, as it is mean to represent intra-patient deformation. An assumption is made that a correctly registered image should have the same pixel intensity value in each corresponding spacial location, thus a cost function of the following form is defined:

$$C(\mu) = \frac{1}{\|\mathcal{S}\| \|\mathcal{T}\|} \sum_{x \in \mathcal{S}} \sum_{t \in \mathcal{T}} (I(T_\mu(x, t)) - \bar{I}_\mu(x))^2, \quad (7.1)$$

where I is a n-dimensional image, $\bar{I}_\mu(x)$ is the average intensity value over time (after

applying the transformation), $T_\mu(x, t)$ is the B-spline coordinate transformation, μ the B-spline parameters, and \mathcal{S} and \mathcal{T} the set of spacial and temporal coordinates respectively. As multiple solutions exist for this equation, an additional constrain is added. As the registration is cyclical, a constrain in the coordinate transformation is added, that the average transformation must be the identity, as in

$$\frac{1}{\|\mathcal{T}\|} \sum_{t \in \mathcal{T}} T_\mu(x, t) = x. \quad (7.2)$$

The minimization equation therefore is

$$\hat{\mu} = \arg \min_{\mu} C(\mu) \text{ subject to (7.2).} \quad (7.3)$$

This equation is minimized using adaptive stochastic gradient descend, a faster converging version of gradient descend[29]. For more details about the specific implementation, refer to the article[39].

This algorithm needs an initial grid of spatial points to register and link via B-splines. The grid size used in this work is an uniformly distributed grid with samples every 13x13x1 voxels.

Quantitative reconstruction quality parameters

To evaluate the quality of the reconstruction, the tumour is going to be the focus, as in the previous chapter. The metrics RMSE and UQI and Segmentation mismatch will also be used, however an additional metric to compute the binary shape location of the tumour will also be used. Using the same tumour area, the tumour will be extracted using morphological operators on images, via binarization with Otsu's method, image dilation and erosion and labelling using connected components. The biggest segmented blob will be then used to compute the geometric center, and the euclidean distance between this and the ground truth will be used as metric of quality. This is due to CBCT not reconstructing HU units of images with the best accuracy, thus the quality of the result on image attenuation coefficient values is less important than the quality of the shape of the tumour. The attenuation coefficients are actually important for RT planning, however CBCT is mainly used to know the tumour shape and location on the treatment.

7.2 Results

In order to evaluate the flexibility of the motion compensated iterative algorithms various numerical test are performed and the qualitative parameters computed in the results. The first test shows the quality of using iterative algorithms versus FDK in 4D CBCT applications, without motion compensation. Then the motion compensated method will be compared to 4DCBCT, using only a tenth of projections. The last tests will focus on DVFs and quality of DVFs. Three different studies are presented. The first shows the effect of a highly under-sampled DVF, the second reconstruct images with 10% of the projections being labelled in the wrong bin (thus using the wrong DVFs) and the last one tests the reconstruction quality in case where DVFs are only available for the tumour area. Comparison to the 3D CBCT image with motion artefacts is not performed in this chapter, needless to say it performs worse than the motion compensation algorithms in all cases except on frame number 4, on where the tumour average lies approximately, thus locating its centroid with the same accuracy as motion compensated methods.

7.2.1 Iterative algorithms vs FDK in 4D CBCT

The standard procedure for a 4D CBCT image used currently in the clinic is to obtain projections of the patient breathing of the order of 1000-1600[66] projections per session while monitoring the breathing phase with some external surrogate. Then the projections are binned for each breathing phase (generally 6-10 different phases) and the images are reconstructed for each bin, with the FDK algorithm. For a dataset of 100 noiseless projections per bin, where all projections have been perfectly binned, and there is no intra-bin motion, figure 7-3 shows the reference images and reconstruction with FDK, SART and ASD-POCS (rows) for bins 0, 3 and 6 (columns), with 50 iterations in the iterative algorithms. The improved quality of the iterative algorithms compared to FDK is clearly visible. This just reaffirms the results presented in other studies[55][59], where iterative algorithms have been shown to be superior than FDK in 4D CBCT. Figure 7-4 shows the quality parameters computed for the tumour area for each frame and algorithm. Iterative algorithms perform better, ASD-POCS obtaining the best result in almost all parameters.

7.2.2 Motion Compensated vs 4D CBCT

The motion compensated reconstruction is compared to 4D CBCT reconstruction in this section. It is important to remember that the motion compensated reconstruction uses only 100 projections in total, the same projections to reconstruct each of the



Figure 7-3: The POPI dataset for three frames (0,3 and 6) and reconstruction of each frame using 100 projections by FDK, SART and ASD-POCS, from top to bottom. The colour scale is linear attenuation coefficient in the range [0-2000].

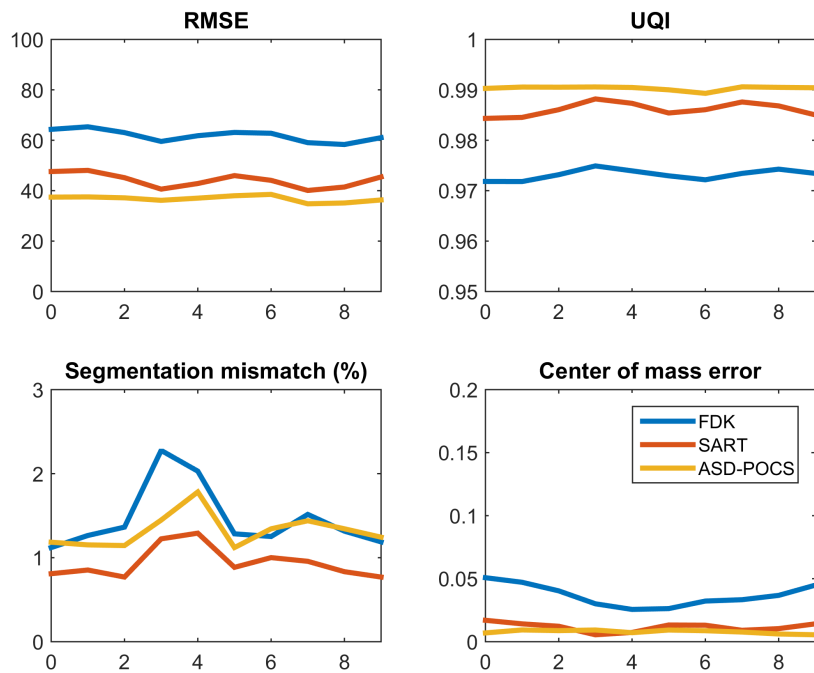


Figure 7-4: Reconstruction quality comparison of 4D CBCT algorithms for each frame. Iterative algorithms show better performance compared to FDK in all cases.

different frames. In the 4D CBCT algorithms the total number of projections is 1000, binned in 10 frames. Figure 7-5 shows the real data, 4D CBCT using FDK and reconstruction using motion compensated algorithms, SART and ASD-POCS respectively. SART has a similar noise level than FDK, while ASD-POCS removes most of that noise. Figure 7-6 shows the quality parameters for 4D CBCT FDK, motion compensated SART and ASD-POCS, and the frame number 4 deformed by the DVFs. This last one is presented to present the quality of the DVFs used. While in the real case the original image would be unknown, especially with this quality, its comparison here is of use. The motion compensated algorithms rely in this data, thus in case where the algorithm itself would have no errors and the DVFs would be completely coherent (perfect match on motion from and to the frames) the warped original image would be the best case scenario for the algorithms. These are not the best quality DVFs (e.g. the ones provided with the POPI model for frame number 1 are better), however they are a good example of smooth DVFs that one can obtain in 4DCBCT.

In the results one can see that while the quality of the reconstruction is lower than in 4D-CBCT, it is still good in general terms. The center of the tumour is located within 1mm of error on most cases, less than the error in proton therapy dose delivery.

7.2.3 Substandard Deformation Vector Fields

The biggest single challenge of the motion compensation method is the fact that obtaining accurate patient specific DVFs is not possible with the current methods. Thus, evaluating numerically how accurately the DVFs need to be known for the algorithm to perform within reasonable limits is an important factor. The previous chapter shows that if the DVFs are perfectly known the motion compensated method can completely eliminate the motions influence in the final image, and the first section of this chapter shows that a smooth cyclic DVF computation algorithm can, while with more error, lead to accurate reconstruction. This section pushes the limits of the DVFs numerically in order to evaluate ho much the reconstruction quality deteriorates with each of the effects. The motion compensated methods with full DVFs are taken as a baseline for comparison.

Undersampled DVFs

While obtaining accurate DVFs may be a problem, it is easier to obtain broad smooth DVFs in a coarse grid that show roughly the motion of the area. Obtaining these is both numerically robust and computationally cheap, making it a viable option in a clinical case. While the DVFs computed for the previous sections of chapter

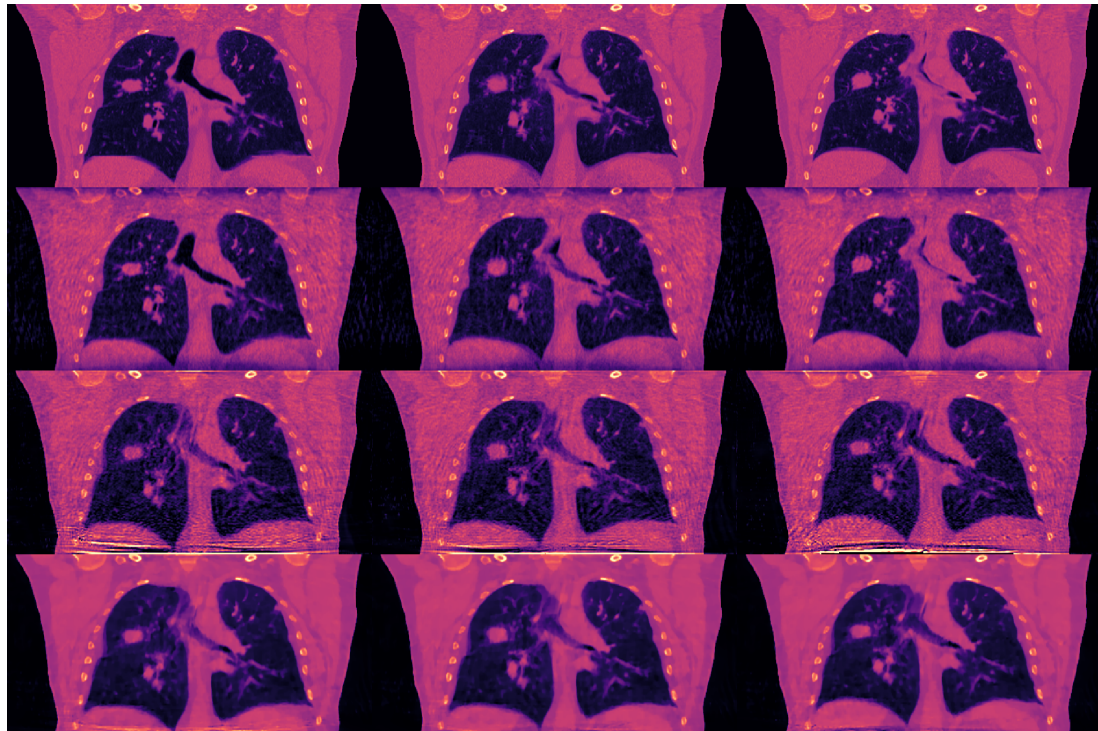


Figure 7-5: The POPI dataset for three frames (0,3 and 6) and reconstruction of each frame 4D CBCT FDK, motion compensated SART and motion compensated ASD-POCS, from top to bottom. The colour scale is linear attenuation coefficient in the range [0-2000].

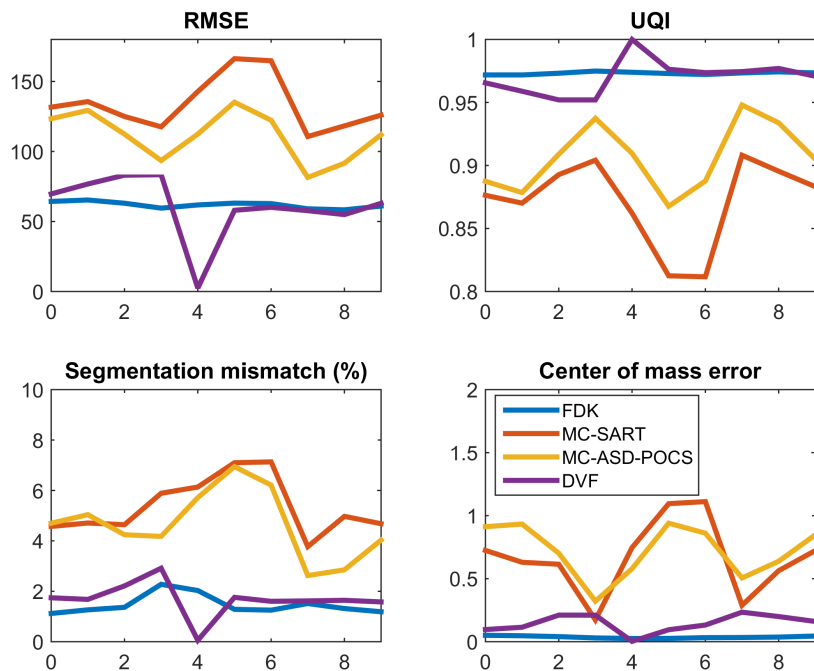


Figure 7-6: Reconstruction quality comparison of 4D CBCT FDK, motion compensated methods (SART and ASD-POCS) and the 4th frame after deformation.

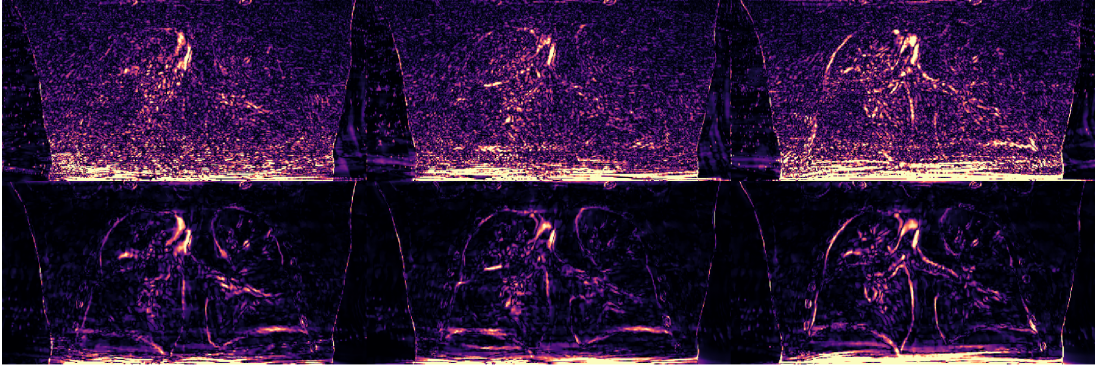


Figure 7-7: Absolute difference plots in frames (0,3 and 6) for the motion compensation methods with full DVFs and undersampled DVFs, for SART and ASD-POCS, from top to bottom. The colour scale is linear attenuation coefficient in the range [0-400].

have been defined in a 13x13x1 spaced grid, the intermediate points are calculated with B-spline, thus allowing more complex behaviour than with linear interpolation in the intermediate voxels. In this simulation, the DVFs defined voxel by voxel is down-sampled to a 16x16x16 spaced grid, resulting on a 22x30x9 grid, that is linearly interpolated.

Visually the results are very similar to the full DVF motion compensation method, so the difference between them is visualized in figure XX for SART and ASD-POCS. The quality parameters are compared to the full DVF motion compensation and 4D CBCT FDK in figure 7-8. In there, while an obvious lower accuracy than the full DVF method is obtained by the undersampled one, the deterioration is not very significant. The location of the tumour is still below 1.5 mm of error for all frames, around 1mm on average.

Binning errors in projections

Another of the most common errors in 4D CBCT is the mislabelling of projections to the wrong breathing phase. When binning the projection, the breathing surrogates monitoring the phase may fail, either due to inherent unavoidable system errors or because the patient changed its breathing pattern during data acquisition. It is thus often a common error that projections are labelled wrongly, generally by 1 bin (e.g. a projection from phase number 4 is labelled as 3 or 5). In this experiment 10% of the projections are randomly mislabelled to an adjacent bin, thus using the wrong DVFs in reconstruction. The effects of this mislabelling can be seen in comparison to correct DVFs in figure 7-9 and the quality parameters can be seen in figure 7-10. The

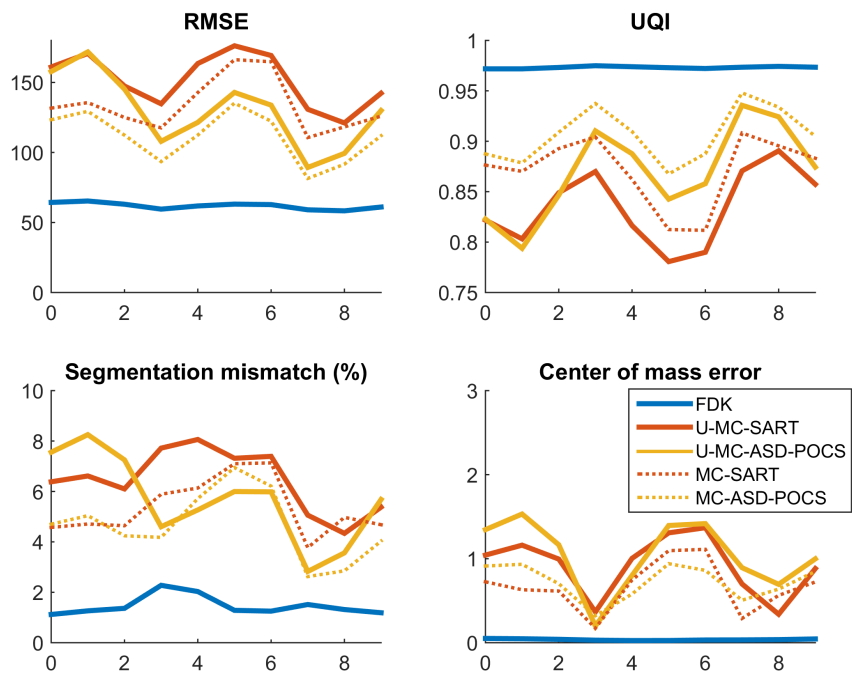


Figure 7-8: Reconstruction quality comparison of 4D CBCT FDK, motion compensated methods (MC-SART and MC-ASD-POCS) and motion compensated methods with undersampled DVFs (U-MC-SART and U-MC-ASD-POCS).

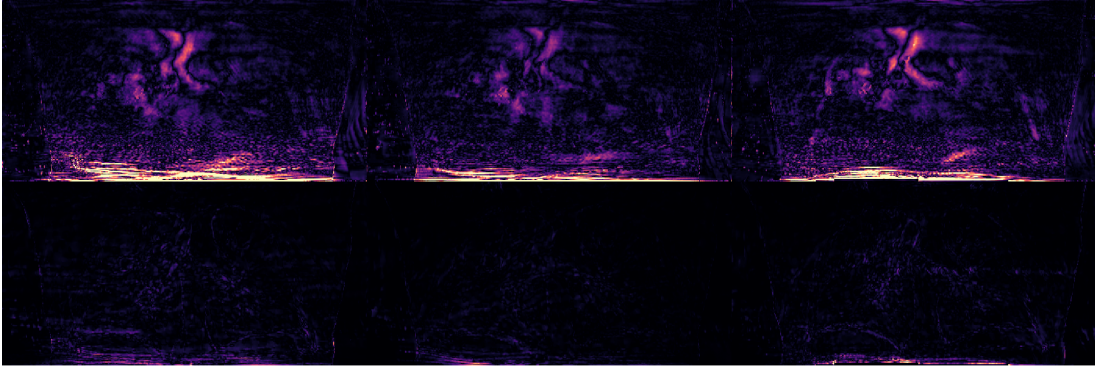


Figure 7-9: Absolute difference plots in frames (0,3 and 6) for the motion compensation methods with and without binning errors, for SART and ASD-POCS, from top to bottom. The colour scale is linear attenuation coefficient in the range [0-400].

results show that for SART, the error in most parameters increase a bit, however for ASD-POCS, the effect is negligible. This is an expected behaviour, as mislabelling of the projections would lead to a wider transition in tumour edges, however the total variation algorithm does sharpen smooth edges, thus removing this effect.

Only tumour motion information

Nowadays clinically used breathing surrogates only give 1D signals of the breathing phase, and there are potential options for obtaining live 1D motion information of the tumour, such as implanted fiducials, ultrasound imaging[73] or electrical impedance tomography[62][48] systems. Thus, evaluating the performance of the motion correction method for when only the motion of the tumour is known is crucial, as this would be the most likely introduction of the method to clinical cases, as the technology already exists. For the tests of this section, the DVFs are cropped to the same area as the tumour is for the quality evaluation, and set to zeros in the rest.

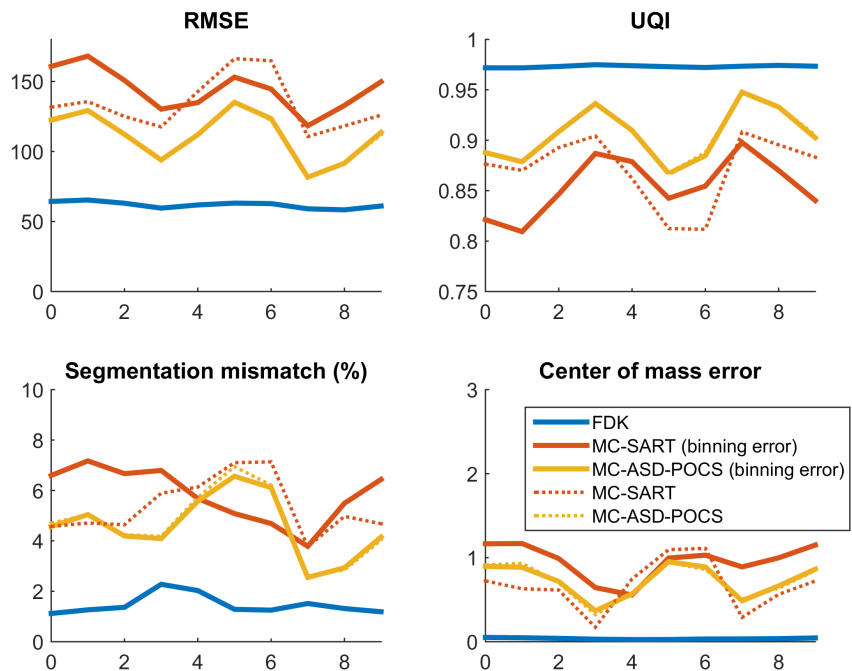


Figure 7-10: Reconstruction quality comparison of 4D CBCT FDK, motion compensated methods (MC-SART and MC-ASD-POCS) and motion compensated methods with errors in projection binning (MC-SART (binning error) and MC-ASD-POCS (binning error))).

7.3 Discussion

This chapter has shown the numerical accuracy of the motion compensated method proposed in this thesis as well as its comparison with standard 4D CBCT methods and its behaviour when the DVFs are suboptimal. First, iterative algorithms perform considerably better than FDK in 4D CBCT reconstruction, as others have already shown. The importance of choosing good algorithms for improved image quality is remarked. The results also hint that the motion compensated method can deliver 4D images using a tenth of the data needed for a 4D CBCT, thus reducing the dose to the patient by a significant amount. It should be also highlighted the robustness of the method to errors in DVFs, most importantly for binning errors and localized motion information. Binning errors are almost unavoidable in clinical cases, and the results clearly show the little effect it has in motion compensated iterative algorithms, especially in noise removing ones, such as ASD-POCS. This not only makes the algorithm robust to mislabels, but also to single breathing inhale-exhale phases that have different amplitude than expected, an effect that happens if a patient takes a deeper or shallower breath than usual. On top of that, the solid results for localized motion information is one of the strongest points in favour of the clinical application of this method, as accurate knowledge of only the tumour location would be enough to obtain a good delineation of the tumour using the motion compensated method.

The quality parameters may need to be redefined to better evaluate the quality of the methods, however. RMSE and UQI are quite straightforward, but they are very limiting when evaluating the performance of reconstruction of something with spatial structure, as e.g. small random noise can increase their values significantly while maintaining the tumour delineation methods equally as accurate. When observing the tumour segmentation mismatch, the data shows that most of the mismatch is a missing 1 pixel wide surface around the motion compensated reconstruction, similar as in figure 6-10. This hints that edge preserving algorithms may delineate the tumour better thus reducing most of the mismatch appearing in the motion compensated reconstruction. Alternatively smarter segmentation methods may also achieve a better delineation of the tumour thus showing a smaller error. The inter-method variation of the quality parameters is something also not expected on average. For example, most algorithms perform a bit worse around the frame 6, and this is highly likely due to DVS errors for this dataset on those frames. If the study were to be performed with multiple datasets, then the error is expected to be the same in all frames on average (assuming DVFs have the same average errors).

This last observation highlights the biggest limit of the study shown in this chapter:

it contains a single dataset. But this doesn't mean that the results are not valid, or that multiple datasets would show a different behaviour, as the cause of the change in quality of the reconstruction is clearly the caused by the algorithms used or the disturbances to DVF introduced. The variation within each of the frames however, is not of big significance. However, if further use of the motion compensation methods for clinical use is desired, the results must be evaluated for multiple datasets. Additionally, the method should be evaluated with real CBCT projections, not only with simulated data.

This chapter strengthens the idea that motion compensated algorithms can have a significant improvement of image quality while reducing the dose to the patients by an order of magnitude.

Chapter 8

Conclusions and Future work

Bibliography

- [1] 4d xcat phantom webpage. Accessed: 2017-10-19.
- [2] Cern phase space tomography. <http://cern.ch/tomography>. Accessed: 2017-10-19.
- [3] Popi model webpage and data. https://www.creatis.insa-lyon.fr/rio/popি-model_original_page. Accessed: 2016-0912-19.
- [4] Martín Abadi, Ashish Agarwal, Paul Barham, Eugene Brevdo, Zhifeng Chen, Craig Citro, Gregory S. Corrado, Andy Davis, Jeffrey Dean, Matthieu Devin, Sanjay Ghemawat, Ian J. Goodfellow, Andrew Harp, Geoffrey Irving, Michael Isard, Yangqing Jia, Rafal Józefowicz, Lukasz Kaiser, Manjunath Kudlur, Josh Levenberg, Dan Mané, Rajat Monga, Sherry Moore, Derek Gordon Murray, Chris Olah, Mike Schuster, Jonathon Shlens, Benoit Steiner, Ilya Sutskever, Kunal Talwar, Paul A. Tucker, Vincent Vanhoucke, Vijay Vasudevan, Fernanda B. Viégas, Oriol Vinyals, Pete Warden, Martin Wattenberg, Martin Wicke, Yuan Yu, and Xiaoqiang Zheng. TensorFlow: Large-scale machine learning on heterogeneous distributed systems. *CoRR*, abs/1603.04467, 2016.
- [5] A.H. Andersen and A.C. Kak. Simultaneous algebraic reconstruction technique (SART): a superior implementation of the ART algorithm. *Ultrasonic imaging*, 6(1):81–94, 1984.
- [6] Ander Biguri, Manjit Dosanjh, Steven Hancock, and Manuchehr Soleimani. Ti-GRE: a MATLAB-GPU toolbox for CBCT image reconstruction. *Biomedical Physics & Engineering Express*, 2(5):055010, 2016.
- [7] Ander Biguri, Manjit Dosanjh, Steven Hancock, and Manuchehr Soleimani. A general method for motion compensation in x-ray computed tomography. *Physics in Medicine and Biology*, 2017.

- [8] J M Blackall, S Ahmad, M E Miquel, J R McClelland, D B Landau, and D J Hawkes. MRI-based measurements of respiratory motion variability and assessment of imaging strategies for radiotherapy planning. *Physics in Medicine and Biology*, 51(17):4147, 2006.
- [9] Y. Censor and T. Elfving. Block-iterative algorithms with diagonally scaled oblique projections for the linear feasibility problem. *SIAM Journal on Matrix Analysis and Applications*, 24(1):40–58, 2002.
- [10] Antonin Chambolle. An algorithm for total variation minimization and applications. *Journal of Mathematical imaging and vision*, 20(1):89–97, 2004.
- [11] Cheng-Ying Chou, Yi-Yen Chuo, Yukai Hung, and Weichung Wang. A fast forward projection using multithreads for multirays on GPUs in medical image reconstruction. *Medical Physics*, 38(7):4052–4065, 2011.
- [12] Cheng-Ying Chou, Yi-Yen Chuo, Yukai Hung, and Weichung Wang. A fast forward projection using multithreads for multirays on gpus in medical image reconstruction. *Medical Physics*, 38(7), 2011.
- [13] Cheng-Ying Chou, Yi-Yen Chuo, Yukai Hung, and Weichung Wang. A fast forward projection using multithreads for multirays on gpus in medical image reconstruction. *Medical Physics*, 38(7), 2011.
- [14] Sophia B. Coban and William R.B. Lionheart. Regularised GMRES-type methods for X-ray computed tomography. In *The third international conference on image formation in X-ray computed tomography*, page 194, 2014.
- [15] Patrick L Combettes and Valérie R Wajs. Signal recovery by proximal forward-backward splitting. *Multiscale Modeling & Simulation*, 4(4):1168–1200, 2005.
- [16] Yi Du, Gongyi Yu, Xincheng Xiang, and Xiangang Wang. GPU accelerated voxel-driven forward projection for iterative reconstruction of cone-beam CT. *BioMedical Engineering OnLine*, 16(1):2, 2017.
- [17] Joan Duran, Bartomeu Coll, and Catalina Sbert. Chambolle’s projection algorithm for total variation denoising. *Image processing on Line*, 2013:311–331, 2013.
- [18] Hao Gao. Fast parallel algorithms for the x-ray transform and its adjoint. *Medical physics*, 39(11):7110–7120, 2012.
- [19] Lucas L Geyer, U Joseph Schoepf, Felix G Meinel, John W Nance Jr, Gorka Bastarrika, Jonathon A Leipsic, Narinder S Paul, Marco Rengo, Andrea Laghi,

- and Carlo N De Cecco. State of the art: iterative CT reconstruction techniques. *Radiology*, 276(2):339–357, 2015.
- [20] G. Han, Z. Liang, and J. You. A fast ray-tracing technique for TCT and ECT studies. In *Nuclear Science Symposium, 1999. Conference Record. 1999 IEEE*, volume 3, pages 1515–1518 vol.3, 1999.
 - [21] S Hancock, M Lindroos, and S Koscielniak. Longitudinal phase space tomography with space charge. *Physical Review Special Topics-Accelerators and Beams*, 3(12):124202, 2000.
 - [22] S Hancock, M Lindroos, E McIntosh, and Mike Metcalf. Tomographic measurements of longitudinal phase space density. *Computer Physics Communications*, 118(1):61–70, 1999.
 - [23] G. T. Herman and L. B. Meyer. Algebraic reconstruction techniques can be made computationally efficient [positron emission tomography application]. *IEEE Transactions on Medical Imaging*, 12(3):600–609, Sep 1993.
 - [24] Varian Medical Systems Inc. Iterative cone beam CT, 2017.
 - [25] X. Jia, H. Yan, L. Cerviño, M. Folkerts, and S.B Jiang. A GPU tool for efficient, accurate, and realistic simulation of cone beam CT projections.
 - [26] Xun Jia, Yifei Lou, John Lewis, Ruijiang Li, Xuejun Gu, Chunhua Men, William Y Song, and Steve B Jiang. Gpu-based fast low-dose cone beam ct reconstruction via total variation. *Journal of X-ray science and technology*, 19(2):139–154, 2011.
 - [27] S. Kaczmarz. Angenäherte Auflösung von Systemen linearer Gleichungen. *Bulletin International de l'Académie Polonaise des Sciences et des Lettres*, 35:355–357, 1937.
 - [28] Avinash C. Kak, Malcolm Slaney, IEEE Engineering in Medicine, and Biology Society. *Principles of computerized tomographic imaging*. IEEE Press, New York, 1988. Published under the sponsorship of the IEEE Engineering in Medicine and Biology Society.
 - [29] Stefan Klein, Josien PW Pluim, Marius Staring, and Max A Viergever. Adaptive stochastic gradient descent optimisation for image registration. *International journal of computer vision*, 81(3):227, 2009.

- [30] Stefan Klein, Marius Staring, Keelin Murphy, Max A Viergever, and Josien PW Pluim. Elastix: a toolbox for intensity-based medical image registration. *IEEE transactions on medical imaging*, 29(1):196–205, 2010.
- [31] Florian Knoll, Markus Unger, Clemens Diwoky, Christian Clason, Thomas Pock, and Rudolf Stollberger. Fast reduction of undersampling artifacts in radial MR angiography with 3D total variation on graphics hardware. *Magnetic resonance materials in physics, biology and medicine*, 23(2):103–114, 2010.
- [32] Robert M Lewitt. Alternatives to voxels for image representation in iterative reconstruction algorithms. *Physics in Medicine and Biology*, 37(3):705, 1992.
- [33] Jörg Liesen and Petr Tichý. Convergence analysis of krylov subspace methods. *GAMM-Mitteilungen*, 27(2):153–173, 2004.
- [34] H. Helen Liu, Peter Balter, Teresa Tutt, Bum Choi, Joy Zhang, Catherine Wang, Melinda Chi, Dershan Luo, Tinsu Pan, Sandeep Hunjan, George Starkschall, Isaac Rosen, Karl Prado, Zhongxing Liao, Joe Chang, Ritsuko Komaki, James D. Cox, Radhe Mohan, and Lei Dong. Assessing respiration-induced tumor motion and internal target volume using four-dimensional computed tomography for radiotherapy of lung cancer. *International Journal of Radiation Oncology*Biology*Physics*, 68(2):531 – 540, 2007.
- [35] Ji Liu and Stephen Wright. An accelerated randomized kaczmarz algorithm. *Mathematics of Computation*, 85(297):153–178, 2016.
- [36] Manasavee Lohvithee, Ander Biguri, and Manuchehr Soleimani. Limited cone beam reconstruction using edge preserving total variation regularisation. 2017.
- [37] Yong Long, Jeffrey A Fessler, and James M Balter. 3D forward and back-projection for X-ray CT using separable footprints. *IEEE transactions on medical imaging*, 29(11):1839–1850, 2010.
- [38] Bruno De Man and Samit Basu. Distance-driven projection and backprojection in three dimensions. *Physics in Medicine and Biology*, 49(11):2463, 2004.
- [39] CT Metz, Stefan Klein, Michiel Schaap, Theo van Walsum, and Wiro J Niessen. Nonrigid registration of dynamic medical imaging data using nD+ t B-splines and a groupwise optimization approach. *Medical image analysis*, 15(2):238–249, 2011.
- [40] Yurii Nesterov. A method of solving a convex programming problem with convergence rate $O(1/k^2)$. In *Soviet Mathematics Doklady*, volume 27, pages 372–376, 1983.

- [41] V. G. Nguyen, J. Jeong, and S. J. Lee. Gpu-accelerated iterative 3d ct reconstruction using exact ray-tracing method for both projection and backprojection. In *2013 IEEE Nuclear Science Symposium and Medical Imaging Conference (2013 NSS/MIC)*, pages 1–4, Oct 2013.
- [42] Yusuke Okitsu, Fumihiko Ino, and Kenichi Hagihara. High-performance cone beam reconstruction using CUDA compatible GPUs. *Parallel Computing*, 36(2):129–141, 2010.
- [43] Nobuyuki Otsu. A threshold selection method from gray-level histograms. *Automatica*, 11(285-296):23–27, 1975.
- [44] W.J. Palenstijn, K.J. Batenburg, and J. Sijbers. Performance improvements for iterative electron tomography reconstruction using graphics processing units (GPUs). *Journal of Structural Biology*, 176(2):250 – 253, 2011.
- [45] Eric Papenhausen, Ziyi Zheng, and Klaus Mueller. Gpu-accelerated back-projection revisited: squeezing performance by careful tuning.
- [46] Hyeong-Gyu Park, Yeong-Gil Shin, and Ho Lee. A fully GPU-based ray-driven backprojector via a ray-culling scheme with voxel-level parallelization for cone-beam ct reconstruction. *Technology in cancer research & treatment*, 14(6):709–720, 2015.
- [47] P. Paysan, M. BREHM, A. Wang, D. Seghers, and J. Star-Lack. Iterative image reconstruction in image-guided radiation therapy, April 20 2017. WO Patent App. PCT/US2016/056,539.
- [48] T Pengpan, ND Smith, W Qiu, A Yao, CN Mitchell, and M Soleimani. A motion-compensated cone-beam ct using electrical impedance tomography imaging. *Physiological measurement*, 32(1):19, 2010.
- [49] James C Phillips, Rosemary Braun, Wei Wang, James Gumbart, Emad Tajkhorshid, Elizabeth Villa, Christophe Chipot, Robert D Skeel, Laxmikant Kale, and Klaus Schulten. Scalable molecular dynamics with NAMD. *Journal of computational chemistry*, 26(16):1781–1802, 2005.
- [50] Wei Qiu, David Titley-Péloquin, and Manuchehr Soleimani. Blockwise conjugate gradient methods for image reconstruction in volumetric ct. *Computer methods and programs in biomedicine*, 108(2):669–678, 2012.
- [51] Sebastian Ruder. An overview of gradient descent optimization algorithms. *CoRR*, abs/1609.04747, 2016.

- [52] Leonid I. Rudin, Stanley Osher, and Emad Fatemi. Nonlinear total variation based noise removal algorithms. *Physica D: Nonlinear Phenomena*, 60(1):259 – 268, 1992.
- [53] Holger Scherl, Benjamin Keck, Markus Kowarschik, and Joachim Hornegger. Fast gpu-based ct reconstruction using the common unified device architecture (cuda). In *Nuclear Science Symposium Conference Record, 2007. NSS'07. IEEE*, volume 6, pages 4464–4466. IEEE, 2007.
- [54] Daniel Schlipske and Henry Medeiros. A fast GPU-based approach to branchless distance-driven projection and back-projection in cone beam CT. In *SPIE Medical Imaging*, pages 97832W–97832W. International Society for Optics and Photonics, 2016.
- [55] Mai L Schmidt, Per R Poulsen, Jakob Toftegaard, Lone Hoffmann, David Hansen, and Thomas S Sørensen. Clinical use of iterative 4d-cone beam computed tomography reconstructions to investigate respiratory tumor motion in lung cancer patients. *Acta Oncologica*, 53(8):1107–1113, 2014.
- [56] Evan E. Schneider and Brant E. Robertson. CHOLLA: A new massively parallel hydrodynamics code for astrophysical simulation. *The Astrophysical Journal Supplement Series*, 217(2):24, 2015.
- [57] WP Segars, G Sturgeon, S Mendonca, Jason Grimes, and Benjamin MW Tsui. 4D XCAT phantom for multimodality imaging research. *Medical physics*, 37(9):4902–4915, 2010.
- [58] Jonathan Richard Shewchuk et al. An introduction to the conjugate gradient method without the agonizing pain, 1994.
- [59] Chun-Chien Shieh, John Kipritidis, Ricky T OBrien, Zdenka Kuncic, and Paul J Keall. Image quality in thoracic 4D cone-beam CT: A sensitivity analysis of respiratory signal, binning method, reconstruction algorithm, and projection angular spacing. *Medical physics*, 41(4), 2014.
- [60] R.L. Siddon. Fast calculation of the exact radiological path for a three-dimensional ct array. *Medical physics*, 12(2):252–255, 1985.
- [61] E.Y. Sidky and X. Pan. Image reconstruction in circular cone-beam computed tomography by constrained, total-variation minimization. *Physics in Medicine and Biology*, 53(17):4777, 2008.

- [62] X. Song, M. Fuss, K.J. Eriksen, D. Erdogmus, M. Deffebach, D. Kaurin, J. Holland, and J. Fitchen. Non-invasive location and tracking of tumors and other tissues for radiation therapy, April 2 2009. WO Patent App. PCT/US2008/077,445.
- [63] Jan-Jakob Sonke, Joos Lebesque, and Marcel van Herk. Variability of four-dimensional computed tomography patient models. *International Journal of Radiation Oncology*Biology*Physics*, 70(2):590 – 598, 2008.
- [64] Thomas Strohmer and Roman Vershynin. A randomized kaczmarz algorithm with exponential convergence. *Journal of Fourier Analysis and Applications*, 15(2):262–278, 2009.
- [65] Ilya Sutskever, James Martens, George Dahl, and Geoffrey Hinton. On the importance of initialization and momentum in deep learning. In *International conference on machine learning*, pages 1139–1147, 2013.
- [66] Sheeba Thengumpallil, Kathleen Smith, Pascal Monnin, Jean Bourhis, François Bochud, and Raphaël Moeckli. Difference in performance between 3d and 4d cbct for lung imaging: a dose and image quality analysis. *Journal of applied clinical medical physics*, 17(6):97–106, 2016.
- [67] William M Thompson and William RB Lionheart. GPU accelerated structure-exploiting matched forward and back projection for algebraic iterative cone beam ct reconstruction. 2014.
- [68] W. van Aarle, W. Jan Palenstijn, J. De Beenhouwer, T. Altantzis, S. Bals, K. J. Batenburg, and J. Sijbers. The {ASTRA} toolbox: A platform for advanced algorithm development in electron tomography. *Ultramicroscopy*, 157:35 – 47, 2015.
- [69] Henk A Van der Vorst. Bi-CGSTAB: A fast and smoothly converging variant of Bi-CG for the solution of nonsymmetric linear systems. *SIAM Journal on scientific and Statistical Computing*, 13(2):631–644, 1992.
- [70] Jef Vandemeulebroucke, David Sarrut, Patrick Clarysse, et al. The popi-model, a point-validated pixel-based breathing thorax model. 2007.
- [71] Curtis R Vogel and Mary E Oman. Iterative methods for total variation denoising. *SIAM Journal on Scientific Computing*, 17(1):227–238, 1996.
- [72] Zhou Wang and Alan C Bovik. A universal image quality index. *IEEE signal processing letters*, 9(3):81–84, 2002.

- [73] Craig Western, Dimitre Hristov, and Jeffrey Schlosser. Ultrasound imaging in radiation therapy: From interfractional to intrafractional guidance. *Cureus*, 7(6), 2015.
- [74] Meng Wu and Jeffrey A Fessler. GPU acceleration of 3D forward and backward projection using separable footprints for x-ray CT image reconstruction. In *3rd Workshop on High Performance Image Reconstruction*, 2011.
- [75] Fang Xu. Fast implementation of iterative reconstruction with exact ray-driven projector on gpus. *Tsinghua Science & Technology*, 15(1):30–35, 2010.
- [76] Fang Xu and K. Mueller. A comparative study of popular interpolation and integration methods for use in computed tomography. In *3rd IEEE International Symposium on Biomedical Imaging: Nano to Macro, 2006.*, pages 1252–1255, April 2006.
- [77] H. Xue, L. Zhang, Z. Cheng, Y. Xing, and Y. Xiao. An improved TV minimization algorithm for incomplete data problem in computer tomography. In *Nuclear Science Symposium Conference Record (NSS/MIC), 2010 IEEE*, pages 2621–2624, Oct 2010.
- [78] Hao Yan, Xiaoyu Wang, Wotao Yin, Tinsu Pan, Moiz Ahmad, Xuanqin Mou, Laura Cervio, Xun Jia, and Steve B Jiang. Extracting respiratory signals from thoracic cone beam ct projections. *Physics in Medicine and Biology*, 58(5):1447, 2013.
- [79] Mingqiang Zhu and Tony Chan. An efficient primal-dual hybrid gradient algorithm for total variation image restoration.
- [80] Mingqiang Zhu, Stephen J Wright, and Tony F Chan. Duality-based algorithms for total-variation-regularized image restoration. *Computational Optimization and Applications*, 47(3):377–400, 2010.
- [81] Andy Ziegler, Thomas Khler, Tim Nielsen, and Roland Proksa. Efficient projection and backprojection scheme for spherically symmetric basis functions in divergent beam geometry. *Medical Physics*, 33(12):4653–4663, 2006.
- [82] Timo Zinsser and Benjamin Keck. Systematic performance optimization of cone-beam back-projection on the kepler architecture. *Proceedings of the 12th Fully Three-Dimensional Image Reconstruction in Radiology and Nuclear Medicine*, pages 225–228, 2013.